Roles of Magnesium and Simvastatin in Structural Changes, Stability, and Affinity of the Ligand Binding Domain of Integrin αXβ2

By

Pragya Manandhar

**A Dissertation Submitted to the Biology and Biochemistry Department,
Natural Sciences and Mathematics
in partial fulfillment of the requirements for the degree of**

DOCTOR OF PHILOSOPHY

in Biochemistry

Chair of Committee: Mehmet Şen

Committee Member: Robert Fox

Committee Member: Robert Schwartz

Committee Member: Richard Willson

Committee Member: Qing Ma

Committee Member: Kevin MacKenzie

**University of Houston
May 2021**

DEDICATION

This dissertation is sincerely dedicated to my father, Dr. Vijay Kumar Manandhar; my mother, Rupa Manandhar; and my dear sisters, Pratibha and Prerana Manandhar, for their abundant love, support, faith, and encouragement, throughout my academic journey.

ACKNOWLEDGMENTS

In this incredible journey of intellectual and scientific growth, I have incurred countless debts of gratitude to those who have supported, guided, and invested in me intellectually, professionally, and emotionally. First of all, I would like to express my deepest gratitude to my advisor Dr. Mehmet Şen, under whose supervision this research work was carried out, for his unwavering support, intellectual guidance, and patience throughout all these years. His continuous encouragement and trust to grow as a protein biochemist, his dedication and enthusiasm towards scientific research, were a constant source of inspiration for me; which I will value for the rest of my life.

I am extremely grateful to my esteemed committee members for their intellectual support, indispensable guidance, and for showing me the right direction: Dr. Fox, Dr. Willson, and Dr. MacKenzie for their guidance and advice with their profound expertise in biochemistry, biophysics, and NMR; Dr. Schwartz for his invaluable insight on my research work; and Dr. Ma for providing me with a perspective aiming at shaping this research work.

Special thanks to Dr. William Widger, Dr. Steven Bark, Dr. James Briggs, and Dr. Michi Umetani for their guidance in collaborative research, unending support, and help with instrumentations. I would like to thank Dr. Tianzhi Wang at UTMB for his help with NMR studies and Dr. James Byrnes for his support with SAXS experiments. I am deeply indebted to Dr. April Bednarski, Dr. Chung Wong, Dr. Tammi Pavelec, Dr. Ricardo Delgado, and Dr. Jennifer Firestine, who instilled in me the interest to pursue a scientific career and guided me during my early days in scientific research.

I wish to express my special thanks to my colleagues in the Şen lab; Collins for his help in biophysical studies, Zeinab for her immense help in cell-based experiments, Micah for painstakingly proofreading this dissertation, and Tannon for his support with research work. I would like to extend my gratitude to Zahra Mazhar and Dr. Yanyun Liu from Briggs lab for their help in the computational research work.

I am extremely grateful to my dear friend and peer, Dr. Shivangi Srivastava, for her friendship and support throughout this journey. I consider myself fortunate to have shared a special friendship with her and Chaitanya all these years. A special thank you to Utsab for your understanding, encouragement, and for always being there for me. A huge thanks to my seniors and colleagues; Drs. Nanda, Abhijeet, Sujina, Abi, Nada, Renee, Brandon, Ran, Neha, Henry, Morgan, Spencer, Suchan, Rahul, Ujwal, Sagar, Rintu, and friends Asha, Jacky, Jonathan, Tweesha, Berra, Shreesti, Stewart, Celise, Taryn, and others for their friendship and support.

I will forever remain indebted to my family. I would not be here without their unconditional love and endless support. I would like to thank my parents for always supporting me in pursuing my dreams and my sisters, Pratibha and Prerana: for being my pillars of strength and keeping me grounded. I am so blessed to share a wonderful bond with them as my sisters and as my closest friends. I would like to thank my brother-in-law Sanjeev for his words of encouragement and my nephew Dheeraj for his help. My deepest gratitude goes to the Pals family and the Adhikari family for their tender love, care, and support. Through them, I have always had a home away from home. Lastly, I remain eternally grateful to everyone who has crossed paths with me in this journey.

ABSTRACT

Myeloid leukocytes contribute to inflammatory responses in immune dysregulations such as atherosclerosis, autoimmune encephalomyelitis, and arthritis. Leukocyte integrin, αXβ2 plays a pivotal role in their recruitment from circulation to lesions. Integrin αXβ2, known as a dendritic cell marker and complement receptor 4, is a heterodimeric cell surface receptor that bi-directionally relays cellular signals and functions in cellular trafficking, phagocytosis, and T-cell proliferation. In the regulation of these events, the ligand-binding domain of αXβ2, called the αX I-domain, acts like the gatekeeper of the bidirectional signals and relays them through affinity maturation and conformational changes from the closed to open state.

A divalent cation is essential for the αX I-domain interaction with an acidic residue of a ligand. The biophysical approaches discussed here reveal that the addition of magnesium ion (Mg^{2+}) results in an alteration of the structure and stability of the αX I-domain in-solution. The multiplicity of the αX I-domain conformations existing in-solution is associated with its affinity regulation to physiological ligands such as fibrinogen and iC3b. The hydrophobic environment in the Metal Ion Dependent Adhesion site (MIDAS), the Mg^{2+}-binding motif, appears to determine the ionization states of two critical MIDAS aspartates, Mg^{2+} creates a link from MIDAS motif to the allosteric sites, all of which contribute to the integrin activation. The local rearrangements and cation-dependent flexibility of the αX I-domain facilitate affinity maturation. These features support the rapid equilibrium of the αX I-domain between the closed and the open conformations required during rapid leukocyte activation, important for regulating leukocyte adhesiveness and migration.

Furthermore, our studies reveal the binding mode of the αX I-domain to its first competitive antagonist, simvastatin, at the molecular level. We show that the carboxylate moiety of simvastatin in hydroxy-form binds to the Mg^{2+} at the MIDAS. This polar interaction is buried by a non-polar environment, which stabilizes the αX I-domain-simvastatin interactions and is potentially the common mechanism for integrin-ligand interactions.

TABLE OF CONTENTS

LIST OF TABLES

LIST OF FIGURES

CHAPTER 1

INTRODUCTION

1.1 Integrins

Integrins are a large family of type-I transmembrane receptors responsible for mediating cell–cell, cell–pathogen, and cell–extracellular interactions in metazoans (1). As an important class of adhesion receptors, integrins bidirectionally transduce biochemical signals across the plasma membrane, facilitating crucial biological processes such as cell migration, proliferation, and differentiation (2). Since their initial identification (3-6), the integrin receptor family has been extensively studied to understand its structure, function, and activation mechanisms. However, due to the differences in expression profiles and cellular functions, different ligands and binding constants, the long-standing question on the mechanism of integrin activation does not hold a unified explanation.

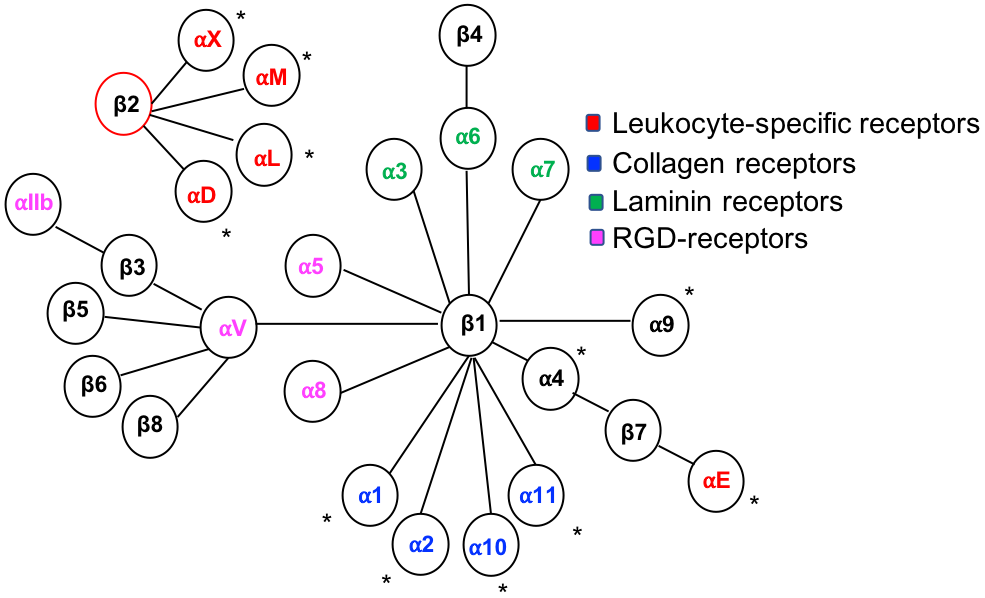

Figure 1: Classification of integrin families.
Heterodimers of 18 types of α subunits and 8 types of β subunits combine to form 24 different integrins shown by connected solid lines. The integrins expressed on immune cells are shown with an asterisk.

Integrins are heterodimeric receptors and exist as two non-covalently bound α and β subunits. There are 18 α and 8 β subunits that associate to form 24 distinct integral heterodimers (Figure 1) (1, 7). The diversity in the subunit composition contributes to the diversity in ligand recognition. Based on their ligand specificities, mammalian integrins are categorized as laminin-binding, collagen-binding, leukocyte, and, RGD-recognizing integrins (Figure 1) (8). Loss of function and mutation studies performed in integrin knockout mice have revealed phenotypes linked to different human diseases depicting the importance of integrins (8, 9).

1.2 Integrin signaling

Integrins function as transmembrane mechanical linkages between the extracellular environment and the cytoskeleton inside the cells. Through extracellular ligand-binding integrins communicate extracellular cellular signals to the intracellular matrix by a process called “outside-in” signaling. The “inside-out” signaling activates integrins via stimuli received from cell surface receptors like B-cell and chemokine receptors, thereby relaying intracellular signals to the extracellular environment (10, 11). The ability of all integrins to relay bidirectional signaling stands out as a unique ability among other membrane receptors. These signaling events are associated with integrin conformational rearrangements and affinity changes, and emerging evidence has shown that the degree of integrin conformational changes and affinity maturation events appear to be integrin specific (12).

1.3 Roles of integrins in immunity

1.3.1 Leukocyte integrins

Among the integrin family, a class of integrins sharing a common β2-subunit (αXβ2, αMβ2, αLβ2, and αDβ2) (Figure 1) along with αEβ7, α4β1, and α4β7 are collectively known as leukocyte integrins. They play essential roles in immune responses to inflammations, infections, and immunosurveillance (13). However, at least 12 types of integrins are shown to be expressed on leukocytes and platelets (14, 15). αLβ2 is expressed on all leukocytes, whereas αXβ2, αMβ2, and αDβ2 are predominantly expressed on myeloid cells at different levels (16-18). Additionally, β2-integrins are also found on extracellular vesicles, which implicate their functions in the progression of pathogenic conditions like sepsis (19). α4β1 is expressed on leukocytes and neutrophils and plays a role in cell adhesion, spreading, and in the homing of memory and effector T lymphocytes to inflamed tissues (20). The expression of α4β7 is reported on NK cells, mast cells, basophils, monocytes, and most abundantly on T lymphocytes that circulate to mucosal tissues. α4β7 activation on leukocytes plays a role in adhesion and migration (21, 22).

β2-integrins play critical roles in leukocyte trafficking and extravasation from the bloodstream to inflammation sites within tissues by controlling cell adhesion, migration, and cytoskeleton reorganization (Figure 2) (23). β2-integrins are fundamental in the formation of an immunological synapse between cells such as an antigen-presenting cell (APC) and a T cell (24), a B cell and a T cell (25), and between a natural killer cell and its target (Figure 2) (26). Therefore, β2-integrins are essential in immunological responses such as T cell activation and phagocytosis. Aberration in expression or

activation of integrins on immune cells results in immunodeficiency or autoimmune diseases such as leukocyte adhesion deficiency (LAD) and systemic lupus erythematosus (SLE) in human, and mouse models (27, 28).

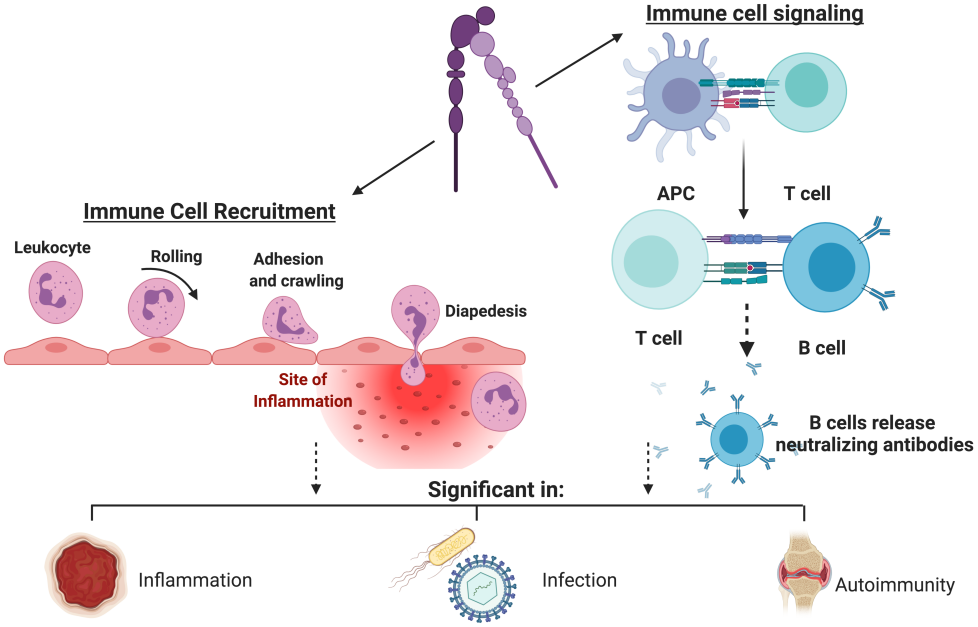

Figure 2: Role of β2-integrins in immune cell functions. Involvement of β2-integrins is crucial in biological processes like inflammation, infection, and autoimmunity. Created with BioRender.com

The significance of β2-integrins is emphasized in the rare genetic diseases called LAD syndromes type I and type III, which are immune deficiency conditions manifested by impaired adhesion of immune cells and a lack of neutrophil extravasation from the bloodstream to sites of inflammation and infections (29, 30). Clinically, LAD can be lethal due to recurrent bacterial infections, systemic sepsis, and impaired immune surveillance. LAD-I, particularly, is caused by mutation in the integrin, beta-2 *(ITGB2)* gene that results in either elimination or reduction in expression of β2-integrins (30, 31). LAD-III results from mutations in kindlin-3, which is a cytoplasmic adaptor protein that binds to integrin β-tail and prevents integrin activation through “inside-out” signaling (29).

Another pathological condition associated with β2-integrins is SLE, characterized by chronic inflammation caused when the immune cells attack healthy tissues in the body. Even though SLE's exact cause is unknown, genetic studies have shown its correlation with the integrin alpha-M (*ITGAM*) and integrin alpha-X *(ITGAX)* genes, which encode for integrin αM and αX subunits, respectively (32, 33). In correlation to SLE, there are single nucleotide polymorphisms in the αM subunit which cause impaired ligand binding and defective cellular cytokine expression (28). Due to the diverse immunoregulatory roles of β2-integrins, modulating integrin activation has been a field of extensive research, and targeting β2-integrins is an attractive approach to treat pathological conditions arising from inflammation.

1.3.2 Integrin αXβ2

Integrin αXβ2 is one of the β2-integrin family members consisting of 150 kDa αX (CD11c) and 95 kDa β2 (CD18) integrin subunits. It is dominantly expressed on monocytes, tissue macrophages, subsets of T and B cells, natural killer cells, and dendritic cells (34).

1.3.2.1 Importance of αXβ2

Integrin αXβ2 is a marker for dendritic cells (DCs) (35). It plays important role in the regulation and priming of the immune system by mediating leukocyte extravasation and phagocytosis. αXβ2, also known as complement receptor 4 (CR4), modulates phagocytosis of particles opsonized with the complement product, iC3b (36), making it a significant player in innate immunity.

Differential expression of αXβ2 is implicated in various diseases. Low expression of αXβ2 can cause autoimmune encephalomyelitis (23) whereas its overexpression on

natural killer cells can cause hypocholesteremia (37). Moreover, αXβ2 overexpression contributes to the onset of atherosclerosis, which is pathologically characterized by leukocyte activation, migration across inflamed endothelium, and deposition on the arterial walls (37). Due to the significant involvement of αXβ2 in the immune system, and related implications in multiple diseases, it is important to characterize its conformational dynamics in relation to αXβ2-ligand interactions, which can provide a better understanding of αXβ2 activation mechanism.

1.3.2.2 Ligands of αXβ2

Integrins have a unique ability to recognize multiple ligands with different affinity energetics, a characteristic that markedly aids in integrin functional diversity. However, this capability also confers challenges for identifying a unique ligand-binding mechanism for each integrin.

Through its ligand-binding domain, called the αX I-domain, αXβ2 binds to the complement fragment—iC3b (36), FcγRIII-B (38), fibrinogen (39), type I collagen (40), intercellular adhesion molecules—ICAM-1 (41), ICAM-2 (42), and ICAM-4 (43), as well as vascular adhesion molecule VCAM-1 (42). αXβ2 also interacts with the non-protein ligand, heparin (44), denatured proteins (45), and negatively charged amino acid residues (46). Since studies have revealed that proteolysis and denaturation enhance binding of the αX I-domain to fibrinogen, αXβ2 has been proposed as a danger receptor for proteolyzed and denatured proteins (46).

In this thesis, the physiological ligands of αXβ2, iC3b, and fibrinogen, are used for binding studies. αXβ2 is a complement receptor of iC3b and C3c, and the interaction with these opsonic fragments of C3 results in phagocytosis of pathogenic particles (47,

48). The complement system involves numerous plasma proteins and is either activated directly by pathogen recognition or indirectly by the pathogen-bound antibodies. The resulting cascade of reactions builds an effective host defense against initial infections. Complement activation can originate by three distinct pathways, with proteolytic cleavage of complement component C3 as the critical step in each (Figure 3).

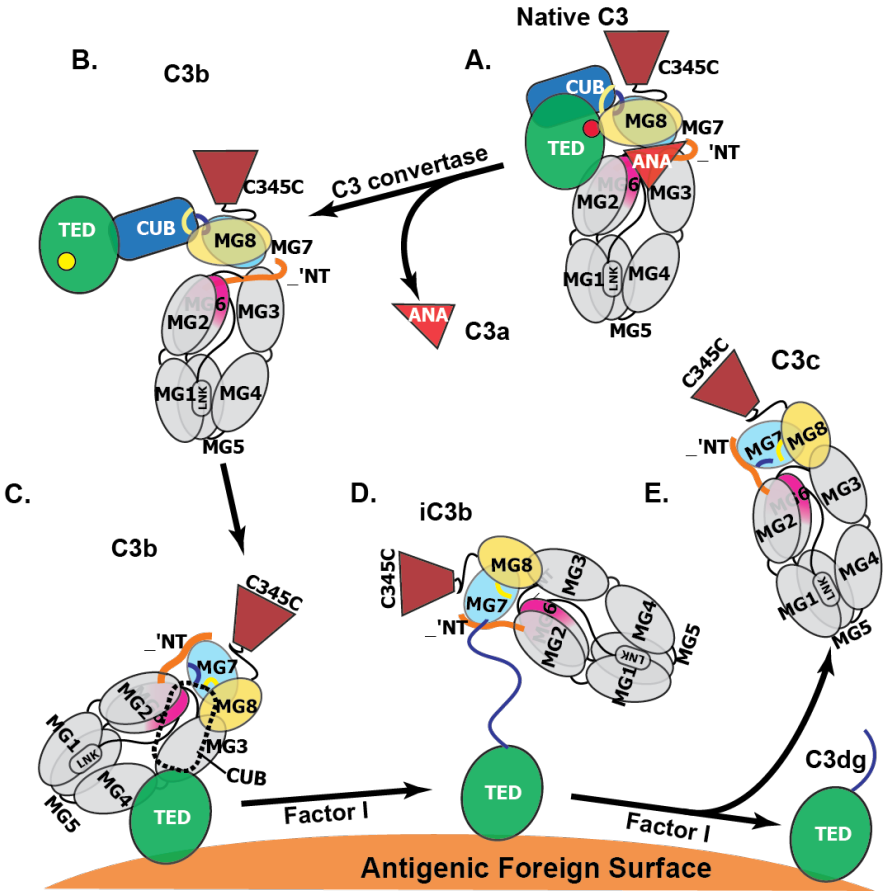

Figure 3: Complement C3 and formation of its products.
Schematic diagram of C3 activation and domain rearrangements. The protease-C3 convertase generated by early trigger enzyme cascade cleaves C3 to C3a, and C3b. The degradation of the C3b forms the 173-kDa inactivated C3b (iC3b) fragment which links to pathogen surface via the thioester domain (TED). Further degradation of iC3b forms C3c, and C3dg.
Adapted from Nishida N., Walz T., & Springer, T. A. (2006). Structural transitions of complement component C3 and its activation products. PNAS, 103(52), 19737-42.

An early triggered enzyme cascade generates the protease-C3 convertase that cleaves C3 to yield C3a, a peptide mediator of inflammation, and C3b, the key molecule

which acts as an opsonin in the complement system by binding to pathogens (Figures 3A to 3B). C3b undergoes subsequent cleavages by the complement regulatory enzyme factor I (FI) (Figures 3C to 3D), resulting in the 173-kDa inactivated C3b (iC3b) fragment that links complement receptors and signaling process (Figure 3D) (49, 50). iC3b is comprised of C3c and thioester domain (TED) linked by a long flexible linker (Figure 3D). The cleavage of iC3b forms C3c and C3dg (Figures 3D to 3E). The C3c gets released to fluid phase and its terminal fragment C3dg remains covalently attached to the thioester domain (Figure 3E). Electron Microscopy (EM) studies have shown that the iC3b-αXβ2 interaction involves the binding of the αX I-domain on the C3c moiety of iC3b at two sites (47, 51).

The major binding site of iC3b to αXβ2 is reported at the interface between macroglobulin MG3 and MG4 domains, and the secondary binding site is reported near the C345C domain (47). This secondary binding region is recently identified as two distinct binding moieties of iC3b, the N-terminal segment of the C3b α'-chain (α'NT) (Figure 3D; orange fragment) and the N-terminus of the residual CUBf segment (Figure 3D; yellow fragment) in the C3 α'-chain which results from cleavage of CUB domain (complement C1r/C1s, sea urchin EGF, and bone morphogenic protein-1 related domain) which specifically binds to the αX I-domain (52). Likewise, the CUBf segment is also shown to bind to the αM I-domain. The αMβ2 through its αM I-domain, also binds to iC3b at a thioester domain and simultaneously interacts through its β-subunit regions with C345C domain in the C3b moiety of iC3b (47).

Another important ligand of αXβ2 is fibrinogen, a large multidomain 340-kDa hexameric protein comprised of two pairs of α, β, and γ polypeptide chains. Fibrinogen

is an important blood plasma protein that is converted into fibrin. Fibrin functions in blood coagulation by preventing blood leaks from vessels. In addition, fibrinogen also functions in platelet aggregation and stimulation of cytokine release in macrophages. Fibrinogen consists of two distal D domains and a central E domain, which upon cleavage by plasmin, results in fragment D and fragment E (53). The αX I-domain binds to the N-terminal domain of the α-chain of fibrinogen in fragment E upon recognition of the (glycine-proline-arginine) sequence (39, 54). The αM I-domain binds to the fragment D of fibrinogen (55). Even though fibrinogen is a ligand for both αXβ2 and αMβ2, αXβ2 exerts a dominant role over αMβ2 during adherence of fibrinogen to macrophages and dendritic cells (56).

Despite the high sequence identity of 60% found between the αX and αM I-domain, striking differences are observed in their binding sites to their ligands iC3b and fibrinogen, respectively (47, 52). Since these two integrins bind to each ligand at distinct sites, elucidating the molecular basis of these interactions could provide a strategy to design integrin-specific therapeutics.

1.3.2.3 Uniqueness of αXβ2 among β2-integrins

αXβ2 is widely used as a marker of dendritic cells (57). αXβ2 and αMβ2 are highly expressed in macrophages, while αLβ2 is expressed in both lymphocytes and myeloid cells (58, 59). Unlike αMβ2, the αXβ2 can bind to proteolyzed fibrinogen with high affinity, thereby increasing neutrophil granulocyte adhesion (46). Both αXβ2 and αMβ2 bind to several structurally unrelated ligands. αXβ2 binds strongly to negatively charged species, while αMβ2 has the propensity to bind positively charges species (60-62). αXβ2 can recognize the high negative charge on microbes and act as a scavenger

receptor to collect proteolyzed protein and alert the immune system regarding infections (63, 64).

αXβ2 and αMβ2 also play different roles in an inflammatory response. αMβ2 plays a critical role mainly in phagocytosis of complement-opsonized pathogens and highlights the well-established theme of complement as the primer of antibody formation (65). While both αXβ2 and αMβ2 are involved in phagocytosis, studies have shown that αXβ2 is more dominant than αMβ2 in adhesion to fibrinogen by human monocyte-derived macrophages and dendritic cells (64). Fibrinogen, a major ligand of β2-integrins, is a critical molecule deposited at sites of injury during inflammation and participates in the adhesion and migration of leukocytes.

Studies involving an opportunistic fungal pathogen, *Candida albicans*, demonstrated that the defense against fungal infections is driven by αXβ2 and not by the αMβ2 receptor (66). Studies on mice deficient in αXβ2 or αMβ2 showed that the production of inflammatory cytokines by renal monocytes and macrophages during the acute phase of fungal infection and protection against death from endotoxin shock were dependent on αXβ2 (64). It was also shown that tissue macrophages first activate and engage αXβ2, and not αMβ2, in primary inflammatory function (64). αXβ2 plays a central role in atherosclerosis development during hypercholesterolemia, evident by studies in which αX-deficient mice exhibited reduced adhesion of monocytes to vascular adhesion molecules and reduced macrophage content in atherosclerotic lesions, thereby decreasing plaque formation (37). In addition, studies have demonstrated the abundance of αXβ2 in mouse atherosclerotic lesions (67).

1.4 Structure of integrins

1.4.1 Overall integrin structure

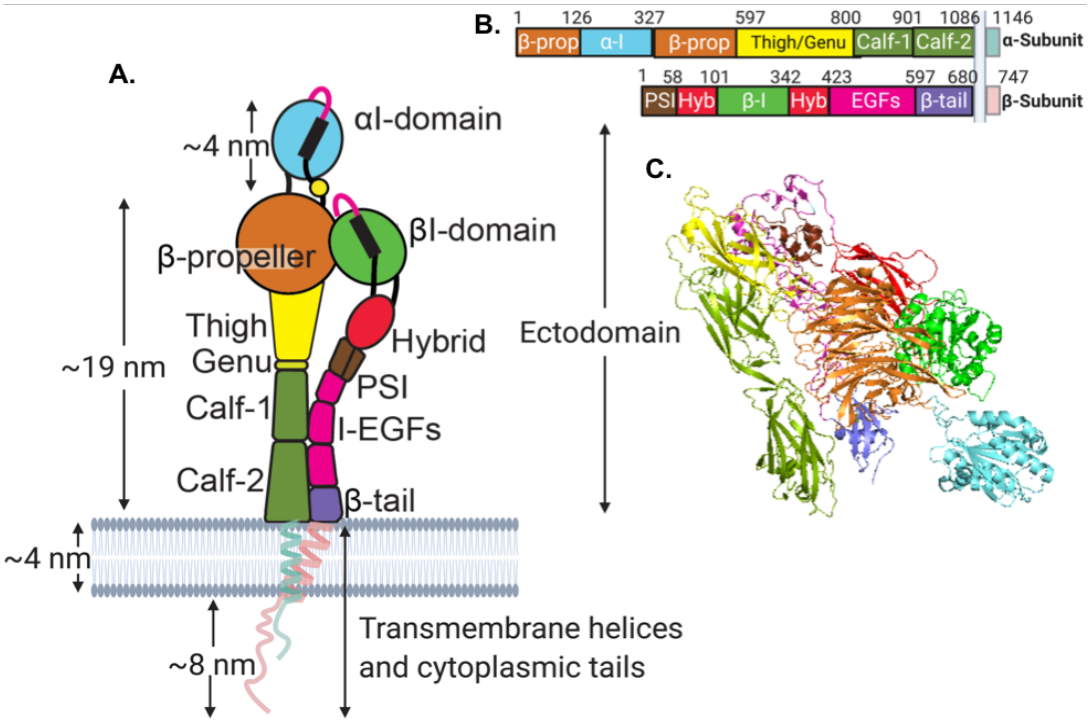

Figure 4: Overall integrin structure. (A) Schematic representation of α/β heterodimeric integrin comprising of two large α/β extracellular multidomains, membrane-spanning helices, and two short cytoplasmic tails depicting approximate dimensions. **(B)** Domain organization of integrin αXβ2. **(C)** Structure of integrin αXβ2 using same color code as *(B)* (illustrated with PyMOL using PDB coordinates 5ES4).Created with BioRender.com

Each subunit of the α/β heterodimeric integrin consists of a large extracellular multidomain, a single membrane-spanning domain, and a short unstructured cytoplasmic tail (with the exception of the β4 subunit containing a long cytoplasmic tail) linking to the cytoskeleton (Figure 4A). Generally, the α and β subunits contain about 1000 and 750 amino acids, respectively, although the sizes of different integrins vary (Figures 4B, C) (68). Numerous high-resolution structures of intact integrin or integrin domains published in the past two decades have contributed to structural insights in understanding of the integrin activation mechanism (48, 68-70).

1.4.1.1 Cytoplasmic tails

The cytoplasmic tails of integrins are typically unstructured and short, usually consisting of 10-70 amino acid residues (Figure 4A). Both the α- and β- cytoplasmic tails serve as hubs for adaptor protein complex assembly. However, the β-cytoplasmic tail is more conserved than the α-cytoplasmic tail across integrin family. Integrins predominantly bind to adaptor proteins such as kindlin and talin through their β-tails during integrin activation (68).

1.4.1.2 Transmembrane type-I helices

The transmembrane helices of integrins are comprised of about 25-29 residues which form homo- or heterodimers of α-helical coils (Figure 4A) (71, 72). Their structural specifics in integrin αIIb/β3 were elucidated by solution NMR analysis (73). The 24-residue αIIb transmembrane α-helix is inserted perpendicular into the membrane, whereas the 30-residue β3 α-helix is tilted in the phospholipid membranes (73). Studies have revealed that the conserved GFFKR and HDR(R/K) sequences stabilize the heterodimer formation in membrane-proximal regions of α and β subunits, respectively (74, 75), keeping most integrins in the bent conformation.

1.4.1.3 Ectodomain

The first structure of complete integrin αVβ3 ectodomain (76) showed that the α-subunit consists of four extracellular subdomains, a seven-bladed β-propeller, a thigh, calf-1, and calf-2 (Figures 4A-C) (76, 77). The integrin α-subunits can be categorized according to whether or not they contain an extra von Willebrand factor A inserted (αI) domain. Half of the 18 α subunits incorporate the inserted (αI) domain of approximately 200 residues that protrudes from the β-propeller domain (Figure 4) (78-80). Unlike the

other four domains, which manifest relatively rigid structures, the αI domain shows structural flexibility relative to the remainder of intact integrin and conformational rearrangement within the domain itself. αI domains function as the only ligand-binding domain when present, and are crucial for bidirectional signal relay between α and β subunits (78, 79, 81).

The β-subunit is composed of eight extracellular subdomains: a β I-domain, a hybrid domain, a plexin-semaphorin-integrin (PSI) domain, four epidermal growth factor (EGF)- like domains, and a membrane-proximal β-tail (βTD) domain (Figure 4). The βI-domain, which is a structural homolog of the αI-domain but not diverged from it, is responsible for ligand binding in the integrin heterodimers, which lack the αI-domain (8).

Integrins are metalloproteins. In the αI-domain containing integrins, the integrin-ligand interactions are dependent on Mg^{2+} which is coordinated by residues in MIDAS (metal-ion-dependent adhesion site) motif. In the integrins lacking an αI-domain, ligand binding is dependent on Mg^{2+} coordinated by MIDAS residues and two Ca^{2+} ions present at the ADMIDAS (adjacent to MIDAS) and SyMBS (synergistic metal ion-binding site) of the βI domain (82). Upon ligand binding, the ligand-binding domain transitions from the closed/low-affinity state to an open/high-affinity state, which leads to the conformational rearrangements in other parts of the integrin (83). Leukocyte integrins are αI-domain containing integrins. The structural changes of the αI-domain will be specifically discussed in detail in Section 1.4.4.

1.4.2 Global conformational changes of the integrin ectodomain

The large global conformational arrangement in the α- and β- subunit of integrins

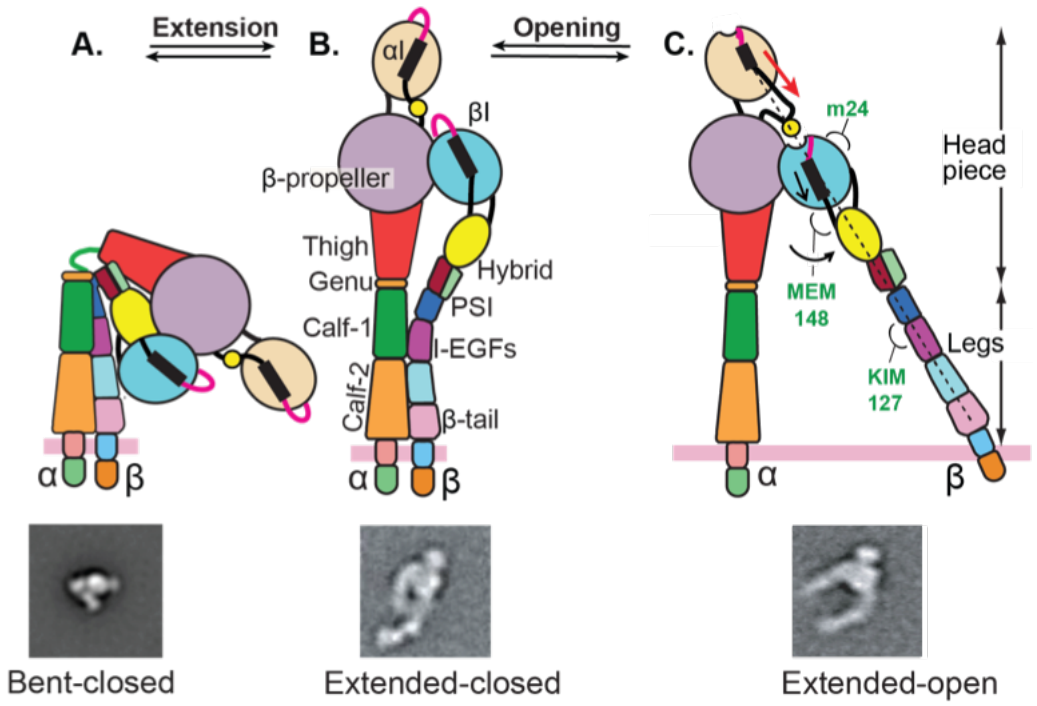

Figure 5: Schematic diagram of different integrin conformations.
Three overall conformation of αI integrins. **(A)** The bent/closed and **(B)** the extended/closed states have low affinity for a ligand, but **(C)** the extended/open is the high affinity state. Electron Microscopy (EM) images depict these conformational states of integrin.
EM images adapted from Nishida N., Xie C., Shimaoka M., Cheng Y., Walz T., & Springer, T. A. (2006). Activation of leukocyte beta2 integrins by conversion from bent to extended conformations. Immunity, 25(4), 583-594.

is associated with a change in integrin affinity and the transmission of biochemical signals from the extracellular domains to the transmembrane and cytoplasmic domains. Electron microscopy (EM) studies have revealed that integrins adopt three overall conformational states: bent with closed headpiece, extended with closed headpiece, and extended with an open headpiece (Figure 5). The bent and extended closed conformations are proposed as the low ligand affinity states (Figures 5A, B). In contrast, the extended conformation with headpiece opening has been proposed as the high ligand affinity conformation (Figure 5C) (48). The extracellular domain extension allows

the headpiece to extend away from the cell surface, yielding in solvent exposure of interfaces between the headpiece and lower legs. The extended conformation with headpiece opening results in rearrangement in MIDAS region of the βI-domain, causing the βI-α7 helix to move downward and derestricting the hybrid domain, which leads to the swing-out of the hybrid domain away from the α subunit (Figure 5C-semi-circular arrow) (14, 84).

Negative-stain EM studies showed that leukocyte integrins predominantly adopt the bent, low-affinity state (85). Hence, extracellular and intracellular ligands are responsible for activating the bent/closed integrin into an extended/open conformation through “outside-in” and “inside-out” signaling, respectively. The extracellular ligand-binding regulates the conformational equilibrium temporally and spatially based upon the cellular activation and association with the cytoskeleton (86).

Upon ligand binding to αI- integrins, the conformational changes occur in the αI-domain and then it interacts with the βI-domain inserted in the hybrid domain —an event that relays cellular signals between α- and β- subunit (Figure 5C). The orientation between the βI- and hybrid domain is critical in integrin conformational change (79). The crosstalk between the αI-domain and the βI-domain results in a 60° swing-out of the hybrid domain from the α subunit (arrow in Figure 5C) (79). This movement, along with a shift of the rigidly connected PSI domain located at knee region of β-subunit, in turn, transitions integrins from a “closed” to an “open” conformation (Figures 5A-C). This association of the αI-domain to the βI-domain is an important activation step since it has been shown to induce a global conformation change of the intact integrin (78, 79, 87).

1.4.3 Coupling of integrin conformational changes and function

The structural diversity, flexibility, and dynamism of integrins are directly related to their functions in mediating interactions between the extracellular environment and the intracellular cytoskeleton (88, 89). These interactions are important for regulating integrin-dependent cellular signalling. The bidirectional signal transduction is associated with fine-tuning of integrin's conformational equilibria (14). However, the mechanisms of the conformational regulation of integrins are diverse and specific to each integrin (90).

The dynamic control of integrin affinity to their respective ligands is essential. Binding of ligands to the extended-open conformation also leads to integrin clustering, intracellular kinase recruitment, and activation of downstream signaling pathways (91). Expression of integrin in a bent, closed state is crucial for its regulation because aberrant integrin activation can be harmful. For instance, αIIbβ3 integrins expressed on platelets are continuously exposed to fibrinogen in the blood and must be maintained in a bent, closed state unless blood vessel injury occurs. Inappropriate activation of αIIbβ3 causes platelet aggregation and thrombosis, resulting in bleeding disorders as well as stroke and heart attack (92-94).

The β2-integrins found in leukocytes and T cells are also predominantly expressed in a bent, closed state and are activated by cytokines that result in ligand binding to mediate cell–cell adhesion assisting in inflammation, phagocytosis, cytotoxic killing, or lymphocyte recruitment (95). On the contrary, integrin α6β4 and α3β1, which form components of hemidesmosomes, are generally present in an extended/open state. These integrins can provide stable mechanical adhesion for linking the extracellular matrix to the actin cytoskeleton (96, 97). The laminin-binding integrin α6β4

was reported to be resistant to conformational regulation and exhibits a completely extended conformation in different buffer conditions, indicating that α6β4 does not require mechanisms for rapid activation since it is expressed on stationary cells and found in an extended conformation (12). Thus, each integrin's specific conformational state contributes to regulating cellular properties to respond to injuries or provide positional uniqueness to a cell for adhesion to another cell or extracellular matrix.

The importance of the conformational states of integrins can be highlighted in several crucial physiological functions. Interestingly, two recent studies have reported that ligand-bound integrin can adopt a bent conformation. Studies using super-resolution microscopy have shown that bent, closed β2-integrins exhibit a face-to-face orientation by their interaction with ICAM dimers in *cis*. Blocking of this interaction resulted in molecular patterns of activated integrins on human neutrophils (98). Interestingly, *cis* interaction was also shown between the αM I-domain and the IgG receptor, FcγRII-A, which was important in regulating neutrophil recruitment (99). An addition of phorbol ester PMA was shown to activate α4β1 without an extension of the receptor. This observation suggests the importance of ligand binding to bent, closed integrin that could be beneficial for receptor clustering and trafficking (89).

Studies have shown that moderate shear force can activate leukocyte integrins (100, 101). The application of tensile force to the integrin-ligand interface results in the αI-α7 helix movement leading to headpiece opening and stabilization of the open conformation. These force-strengthened integrin-ligand interactions, along with the associated stabilization of conformational changes, could be important for cellular migration (102).

1.4.4 Structural changes in the αI- and βI-domain

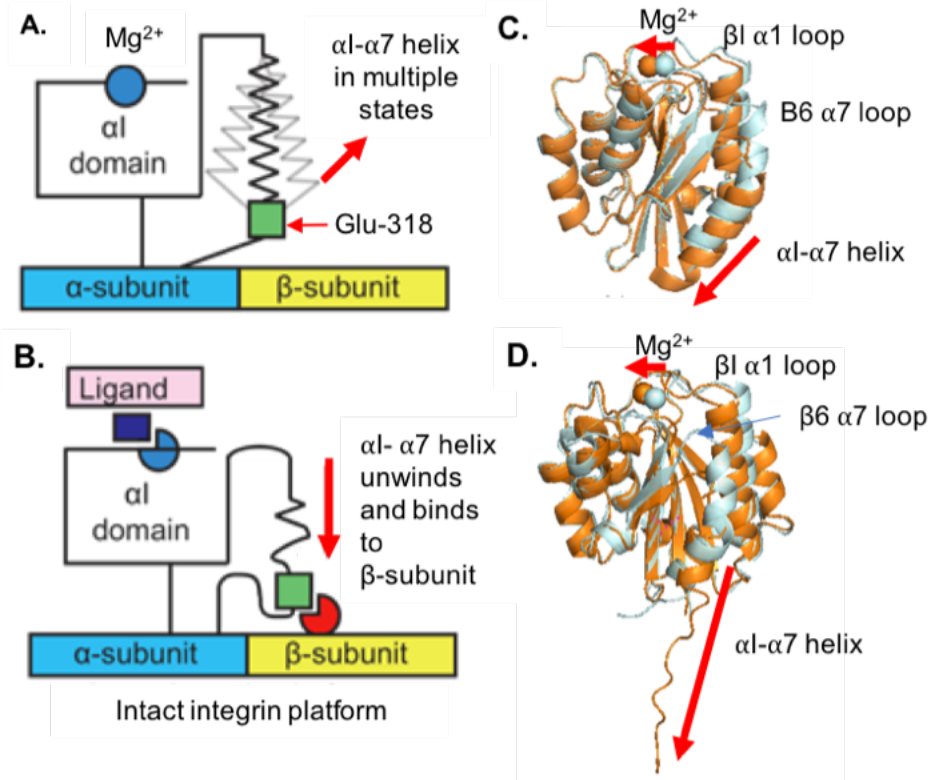

Figure 6: Structural rearrangements during integrin activation. Schematic diagrams of the αI-α7 helix motion during the integrin activation from **(A)** the closed/low-affinity states to **(B)** open/high-affinity states on intact integrin. **(C)** Superimposition of the isolated closed (PDB# 1JLM) and open (PDB# 1IDO) αM I-domain. **(D)** Superimposition of the closed (PDB# 5ES4) and open (PDB# 4NEH) αX I-domain on intact αXβ2.

The α- and β- I-domains adopt a Rossmann-type fold with a central, hydrophobic six-stranded β-sheet surrounded by seven amphipathic α-helices. The αI-domain physiologically consists of a Mg^{2+} ion in the metal ion-dependent adhesion site (MIDAS) at the ligand-binding "top" face at the C terminal ends of the parallel β strands (Figure 6C) (87, 103). The N and C terminus at the "bottom" face the αI-domain are flexibly linked to the β-propeller domain. The flexibility of the N-terminal linker is limited due to the disulfide bond to a β-propeller loop followed by a short sequence formed by three residues (79). On the contrary, the C-terminal linker is highly flexible, and consists of a

Ser/Thr- rich 10 residue sequence. The first crystal structure of the αX I-domain lacked a metal at the MIDAS (103), and has not been crystalized with any cations so far. However, the crystal structure of the αXβ2 ectodomain acquired in later years contained a metal ion at the MIDAS (78, 79).

1.4.4.1 MIDAS movement

Structural studies have revealed that the αXI-domain samples two major conformations termed as closed and open states (79, 85, 103). The closed state transitions to the open state during an integrin activation, but molecular details of conformational transitions are highly elusive.

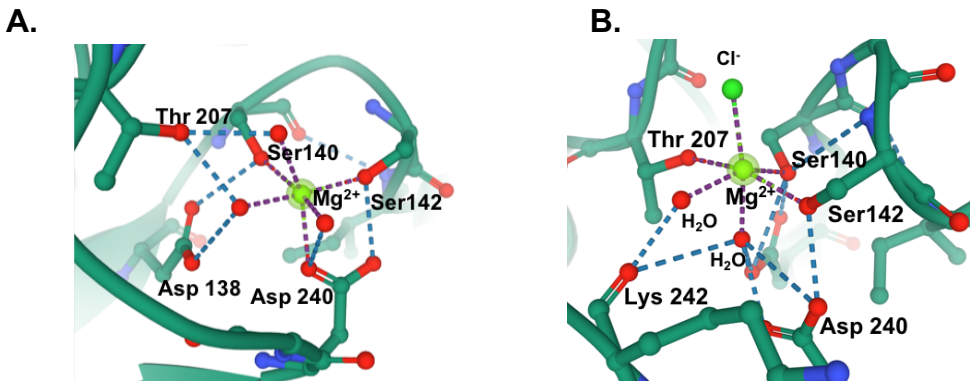

Figure 7: Difference in the magnesium coordination at MIDAS in the closed and open states of the αX I-domain.
A) closed/low- affinity state (PDB# 5ES4) **(B)** open/high-affinity state (PDB# 4NEH).

The αX I-domain binds to ligand with the coordinated Mg^{2+} ion and metal-coordinated residues in three different loops of MIDAS. The metal coordinating residues are mostly polar and negatively charged amino acids. For example, the β1α1-loop contains three coordinating residues in a sequence of Aspartate-X-Serine-X-Serine (DXSXS) MIDAS motif, which is shown to be conserved among the αI-domains. For Mg^{2+}coordination, the second loop donates a Threonine (Thr 207) residue, and the third

loop donates an Aspartate (Asp 240) residue (79). A water molecule forms a hydrogen bond with the side chains of MIDAS residues Asp 138, Thr 207, and Asp 240, as shown in (Figures 7A, B). Upon transitioning from the closed to the open state, the Mg^{2+} ion at MIDAS moves 2.5 Å, breaking direct coordination with Asp 240 and gaining coordination with Thr 207 (79).

1.4.4.2. The allosteric α7-helix motions in the αX I-domain

In the closed state of the αX I-domain, the αXI-α7 helix is tightly associated with the body of the domain through hydrophobic contacts (Figure 6A, C) (78, 103). In the αI-domain opening, the β6 strand tilts and the β6α7-loop moves toward the C-terminus with the downward movement in the α7-helix by 10 Å (Figure 6C). In an intact ectodomain, the C-terminal portion of the α7-helix completely unwinds and the α7-helix is elongated. Studies using nuclear magnetic resonance (NMR) spectroscopy have also suggested that the αI α7-helix is highly flexible (104). With this high flexibility, its terminal residue Glutamate (Glu 318), could reach and bind to the β2 I-domain MIDAS (Figures 6B, D), and, together with a couple of preceding hydrophobic residues, act as the internal ligand for the β2 I-domain (Figure 6B) (79).

1.4.4.3 Allosteric crosstalk between MIDAS and the αI-α7 helix

The ligand-binding causes a synchronized reorganization of the loop around MIDAS and is hypothesized to induce a downward motion of the distal αI α7-helix through allostery (79, 105). This relay of allostery is essential in bidirectional signal transduction.

1.4.4.4 Mimicking αI-domain activation using a point mutation

The side chain of Isoleucine (Ile 314) present towards the end of the α7-helix is buried in a hydrophobic pocket (also known as SILEN-socket for Isoleucine) formed by side chains of hydrophobic residues in its proximity. Mutation of Ile 314→Glycine (Gly) (SILEN mutation) disrupts the contact between this residue and the hydrophobic pocket and increases the ligand affinity of the αI-domain (103). This Ile 314 Gly mutated SILEN αX I-domain is shown to destabilize the closed conformation of the αX I-domain and shift the conformational equilibrium towards the open state (103). Based on affinity and kinetics measurements, this SILEN mutant has been proven to provide the important end-point of the high ligand-binding affinity of the αX I-domain. Notably, the αM I-domain structure with SILEN mutation is shown to adopt an open state conformation (106).

1.5 Towards new area of designing integrin-specific therapeutics

Integrins are proven drug targets. Integrin αXβ2 proves to be a potential therapeutic target due to its roles in autoimmune pathologies and cancer microenvironment. Although antibody-based therapies have been investigated for T-cell modulation by targeting β2-integrins as antagonists, these anti-inflammatory treatments were unsuccessful in clinical trials. This unmet need in the field highlights an urgency for developing non-antibody-based antagonists. That being the case, small molecule antagonists can be advantageous in regulating integrin functions with high specificity and lower concentration. Hence, some small molecules have been of great interest due to their ability to induce integrin structural changes (107, 108). Understanding the allostery and structural perturbations of β2-integrins by identifying small molecule

antagonists and agonists and determining the binding mode of integrin-small molecule interactions will advance strategies for designing second generation specific small molecule inhibitors and activators.

Several small-molecule inhibitors of β2-integrins have been identified (109-111). Clinically, statins are widely used to reduce cholesterol levels in patients by inhibiting HMG-CoA reductase. They also possess pleiotropic effects such as anti-inflammatory ability (108-110, 112, 113). The type-I statins such as lovastatin, simvastatin, and mevastatin, have been shown to inhibit the binding of LFA-1 to ICAM-1 (108, 110). Lovastatin is shown to have significantly changed leukocyte distributions in several lymphoid tissues *in vivo* (109).

Studies have shown the binding of hydrolyzed simvastatin (Figure 8B) to the αM I-domain inhibits αM I-domain's binding to its physiological ligands like iC3b and C3b (107). The carboxyl group of the hydrolyzed simvastatin was found to bind Mg^{2+} at the αM I-MIDAS (107).

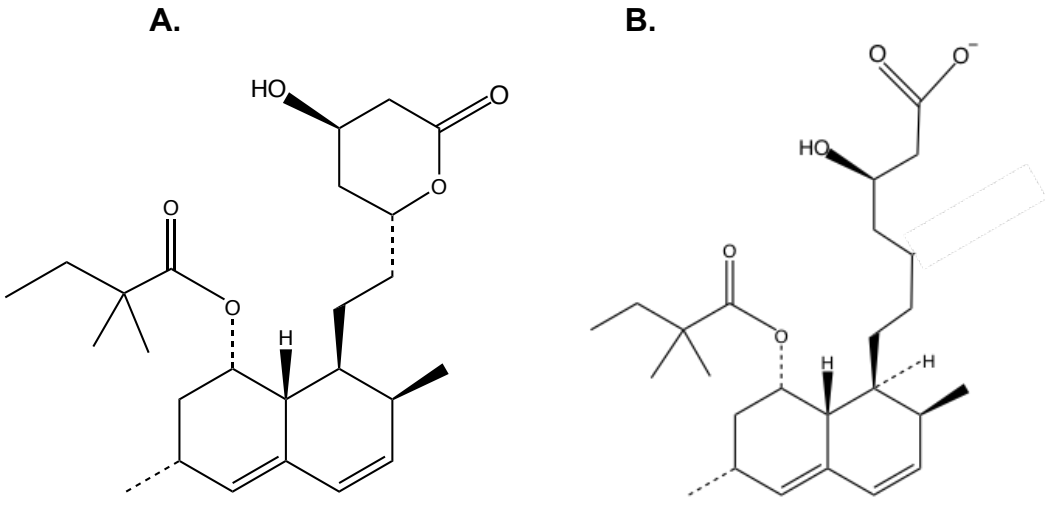

Figure 8: Structures of simvastatin (A) Lactone Prodrug **(B)** Hydroxy-acid-form.

1.6 Dissertation summary

In my doctoral study, I carried out the biophysical characterization of the wild-type (WT) and SILEN αX I-domain representing the closed and open conformation, respectively. We examined the effect of divalent cations on the thermodynamics and conformation of the αX I-domain. We showed that Mg^{2+} affects the affinity modulation of the αX I-domain. Additionally, we demonstrated that simvastatin in its carboxylate form (Figure 8B) binds to the αX I-domain and antagonizes binding of iC3b to the αX I-domain. We identified the simvastatin-αX I-domain interaction interface and elucidated the binding mechanism.

CHAPTER 2

MATERIALS AND METHODS

2.1 Expression of the recombinant αX I-domain

The recombinant αX I-domain gene used for this study is the sequence coding for the amino acid residues Glutamine (Gln 129) to Glycine (Gly 319) of the intact CD11c gene. This CD11c gene fragment subcloned into the pgEX-6P expression vector with an N-terminal Glutathione S-transferase (GST) affinity tag was the construct used for the expression of the WT αX I-domain. This construct included Alanine (Ala 232)→Thr mutation for increasing the solubility of the αX I-domain. This mutation is not in close vicinity of functional sites and regularly used for the αI-domain studies. The Ile 314→Gly encoding construct was used to express the SILEN αX I-domain. The recombinant αX I-domain plasmid was transformed into *E. coli* Rosetta BL21(DE3) cells. To begin the transformation, 50 ng of the plasmid was added into 50 µL of *Escherichia coli* Rosetta BL21 (DE3) cells in a microcentrifuge tube placed on ice. After gently flicking the tube's bottom to mix the cells and plasmid, the tube was incubated on ice for 30 minutes. To heat shock the cells, the tube was placed into a 42 ºC water bath for 45 seconds and immediately returned to the ice for 3 minutes. 250 µL of Luria Bertani (LB) (Appendix 1) media was added, cells were incubated at 37 ºC for 1 hour while shaking on an orbital shaker at 225 rpm. Next, 100 µL of the suspended cells were plated on an LB agar plate containing 100 µg/mL carbenicillin and 100 µg/mL chloramphenicol and incubated at 37 ºC for 12 to 16 hours.

After incubation, a single colony was inoculated into a 5-mL starter culture of LB media containing the antibiotics at 37 ºC with vigorous shaking at 225 rpm for overnight

growth (12 to 16 hours). 1 mL of the overnight starter culture was used in the following day to inoculate 1 L of LB media at 1:1000 dilution with antibiotics. The cells were grown until OD_{600nm} of 0.5-0.7 was reached. The temperature of the cells was reduced to room temperature by leaving the flasks at 4 ºC for 20 minutes to decrease the rate of protein synthesis-a process which is advantageous for proper protein folding and solubility. The cells were then induced to express the αX I-domain by adding isopropyl-1-thio-B-D-galactopyranoside (IPTG) to a final concentration of 1 mM. The cells were incubated overnight (14-16 hours) at 22 ºC with vigorous shaking at 225 rpm. Cell pellets were harvested the next day by centrifugation at 3500 rpm for 30 minutes.

To obtain isotopically labeled αX I-domain protein for nuclear magnetic resonance (NMR) studies, the cells were grown in 1 L of M9 salts minimal media (Appendix 1). 1 mL of the overnight starter culture used for inoculation in minimal media was grown in LB media. All remaining procedures for protein expression in minimal media were similar to the steps mentioned earlier for protein expression in cells grown in LB media. For isotopically labeled samples, ^{15}N-labeled ammonium chloride ($^{15}NH_4Cl$) and ^{15}N-labeled ammonium sulfate $(^{15}NH_4)_2SO_4$ were used as the sole nitrogen sources.

2.2 Purification of the recombinant αX I-domain

The harvested cells obtained by following procedures described in Section 2.1 were resuspended in 50 mL of lysis buffer (20 mM Tris-HCl, 200 mM NaCl, 10% glycerol, pH 8.0). The cell suspension was thoroughly lysed by passing through the Avestin Emulsiflex C3 homogenizer at 10,000 psi five times. The cell lysate was incubated with 1X phenylmethanesulfonyl fluoride (PMSF) and 1 mM DNase by gently

rocking at 4 ºC for 30 minutes. Next, the lysate was centrifuged at 20,000 X *g* in polycarbonate centrifuge tubes for 45 minutes at 4 ºC.

The GST-fused αX I-domain was purified by affinity purification using glutathione sepharose resin (Cytiva; product number 17075601) column. All prepared buffers used for protein purification were filtered through a 0.45 µm filter and degassed for 20 minutes. The resin was equilibrated with GST binding buffer (20 mM Tris-HCl, 300 mM NaCl, 10% glycerol, pH 8) for five column volume (CV). The supernatant obtained from the lysate was filtered through a 0.45 µm filter and loaded onto an equilibrated glutathione sepharose resin column at a 1 mL/minute flow rate. After washing the column with the GST binding buffer for five CV, the protein was eluted with the GST elution buffer (20 mM Tris-HCl, 200 mM NaCl, 10 mM reduced glutathione, 10% glycerol, pH 8) in 5 mL fraction sizes.

The protein-containing fractions were collected and subjected to site-specific cleavage using hexameric histidine-fused human rhinovirus 3C protease. The 3C protease to GST-fused αX I-domain protein ratio was 1:20. The digestion mixture (1-2 mg/mL GST-fused αX I-domain, 3C protease, 20 mM Tris-HCl, 15 mM BME in 30 mL) was transferred into a dialysis bag of 10 kDa molecular mass cut-off (Sigma-Aldrich) and set up for dialysis-digestion procedure. The dialysis bag was kept afloat in the dialysis buffer (20 mM Tris-HCl, 100 mM NaCl, 15 mM BME, 10% glycerol, pH 8) and gently stirred for 16 hours at 4 ºC for complete digestion.

After overnight digestion, the digestion mixture was spun down to remove any possible precipitation. The resulting supernatant was passed through a Ni-sepharose HisTrap HP column (GE-Healthcare) to remove the 3C protease fused to the hexameric

histidine tag. Before passing the protein mixture, this column was equilibrated with the binding buffer (20 mM Tris-HCl, 300 mM NaCl, 40 mM imidazole, 10% glycerol, pH 8). The resulting flow-through was the mixture of 22 kDa αX I-domain and the cleaved 26 kDa GST protein. The HisTrap column was washed with binding buffer (20 mM Tris-HCl, 300 mM NaCl, 40 mM imidazole, 10% glycerol, pH 8) for five CV to ensure that the protein of interest was thoroughly released, after which the his-tagged 3C protease was eluted with the elution buffer (20 mM Tris-HCl, 300 mM NaCl, 500 mM imidazole, 10% glycerol, pH 8). The collected flow-through was further passed onto the equilibrated glutathione sepharose resin to remove the cleaved GST protein. The resulting flow-through fractions mostly contained the 22 kDa αX I-domain.

Finally, the fractions containing the target protein were pooled together and concentrated to 5 mL using Amicon ultra centrifugal filter unit with a 10 kDa molecular mass cut-off (Amicon). The concentrated protein solution was centrifuged to remove any precipitation. Further purification of the concentrated αX I-domain was performed using the HiLoad 16/60 Superdex-75 prep grade column (GE Healthcare/Amersham) on the ÄKTA FPLC (Amersham Biosciences) system. The 5-mL sample was loaded into the S75 column previously equilibrated with 20 mM Hepes, 150 mM NaCl, pH 7.5 buffer prepared in chelex-treated water. In our studies, the chelex-treated water is the water obtained by passing the MilliQ water through a chelex-100 resin (Bio-Rad catalogue number 142-2832) multiple times to remove its trace amount of metal ions. Chelex resin is a styrene-divinylbenzene copolymer containing paired iminodiacetate ions, which can chelate polyvalent metal ions and operate in a pH solution of pH 4 or above (114). Since our experiments involved studying the effects of cations on the protein, we wanted to

ensure that the water used for the protein suspension and the buffer preparations did not contain any metal ions.

The sample was run for 2 hours at a 1 mL/minute flow rate and eluted in 1 mL fraction volumes. Any GST protein contamination was successfully removed in earlier elution fractions during size exclusion chromatography since this protein dimerizes and forms a 52 kDa GST dimer. The resulting αX I-domain peak fractions from the final size exclusion chromatography were evaluated for purity using the 12% sodium dodecyl sulfate-polyacrylamide gel electrophoresis (SDS-PAGE).

For SDS-PAGE gel electrophoresis (Appendix 2), 50 µL of protein sample was mixed with 10 µL of loading buffer before being heated at 95 ºC for 3-5 minutes. SDS-PAGE gels were run for 120 V until the protein reached the end of the stacking gel and at 200 V for protein separation on resolving gel in the SDS running buffer using Bio-Rad electrophoresis tank. Gels were stained with silverstain blue (Thermo Fisher Scientific) and destained with MilliQ water. The Precision Plus Protein™ all blue prestained protein standards (Bio-Rad; catalogue number 1610373) was used as a protein marker.

The purification procedures eventually yielded 3-5 mg of the monomeric αX I-domain with approximately 95% purity from a liter of bacterial cell culture. The protein concentration was measured by its UV absorbance at 280 nm and using the extinction coefficient of 11470 $M^{-1}cm^{-1}$, which was calculated with the protparam tool (https://web.expasy.org/protparam).

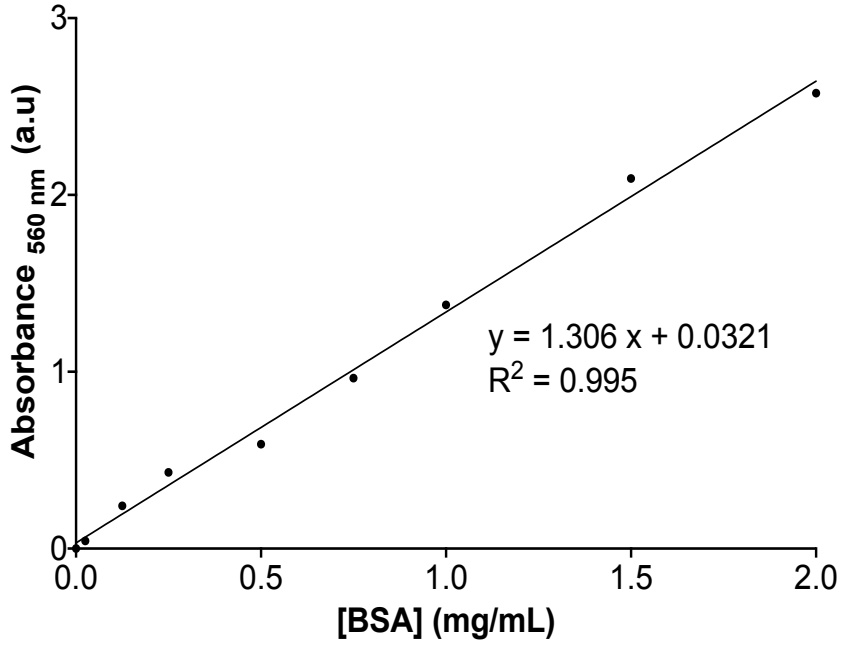

Figure 9: Standard linear plot of the BCA assay using 9 different concentrations of BSA protein. The equation derived from the linear plot was used for determining the concentration of the unknown (αX I-domain) protein samples.

2.3 Determining protein concentrations by BCA assay

The protein concentration was also measured by colorimetric detection using the bicinchoninic acid (BCA) Pierce™ protein assay kit (Thermo Fisher Scientific™). Bovine serum albumin (BSA) was used as the protein standard by using a series of dilution of its known concentration. All assays were conducted in the white 96-well polystyrene microplates (Pierce™) in triplicate. The assay was carried out in a volume of 25 µL, and the sample to working reagent ratio was at 1:8 (vol/vol). The total volume of working reagent required was calculated as [Number of standards (9) + Number of unknowns (6)] X [Number of replicates (3)) X (volume of working reagents per sample (0.2 mL)] = 9 mL. To 25 µL of each standard, 200 µL of the working reagent was added and mixed thoroughly on a plate shaker for 30 seconds. The microplate was covered and

incubated at 37 ºC for 30 minutes. The microplate was then cooled to room temperature, and the absorbance was measured on a Perkin Elmer Victor X4 plate reader at 560 nm. The 560 nm absorbance measurement of the blank standard without the protein was subtracted from the individual standards' measurement.

For each value of absorbance (y) measured as the absorbance of αX I-domain, its correct concentration (x) was determined by using the equation from the linear plot (y = 1.306 x + 0.031) (Figure 9 and Table 1).

Table 1: Protein concentration values determined by nanodrop and BCA assay

[αX I-domain] by Nanodrop (mg /mL)	Average [WT αX I-domain] from BCA assay (mg/mL)	Average [SILEN αX I-domain] from BCA assay (mg/mL)
0.5	0.584	0.467
1.0	0.925	0.899
1.5	1.285	1.155
2.0	1.515	1.457
3.5	2.202	2.210

Table 2: Molar absorptivity coefficient of the WT αX I-domain determined from BCA assay

(WT αX I-domain)			
Average observed Absorbance (a.u)	Average concentration (gm/dm^3)	Average concentration (mol/dm^3)	Calculated Molar Absorptivity ($M^{-1}cm^{-1}$)
1.240	0.925	4.21×10^{-05}	29461.750
1.711	1.285	5.85×10^{-05}	29248.154
2.010	1.515	6.88×10^{-05}	29207.438

Table 3: Molar absorptivity coefficient of the SILEN αX I-domain determined from BCA assay

(SILEN αX I-domain)			
Average observed Absorbance (a.u)	**Average concentration (gm/dm^3)**	**Average concentration (mol/dm^3)**	**Calculated Molar Absorptivity ($M^{-1}cm^{-1}$)**
0.642	0.467	2.12×10^{-05}	30176.810
1.206	0.899	4.09×10^{-05}	29451.418
1.541	1.155	5.26×10^{-05}	29277.793

The reported molar absorptivity of the αX I-domain was 11460 $M^{-1}cm^{-1}$. The observed average molar absorptivity of the WT and SILEN αX I-domain were determined 29334.227 $M^{-1}cm^{-1}$ and 29635.343 $M^{-1}cm^{-1}$, respectively (calculated from Table 2 and Table 3). The correction factors were 2.56 and 2.59 for the WT and SILEN αX I-domain, respectively.

2.4 Identification of αX I-domain using mass spectrometry

It is important to precisely identify the purified protein using other analytical methods aside the SDS-PAGE experiment. The region of the SDS-PAGE gel containing the αX I-domain was cut carefully and placed in a LoBind Eppendorf tube. The gel piece was minced into <1 mm sizes and destained with 500 µL of 100 mM ammonium bicarbonate: acetonitrile solution in 3:3 vol/vol ratio at 37 ºC for 30 minutes. After three destaining cycles, the obtained colorless gel pieces were dehydrated with 200 µL of acetonitrile at room temperature for 10 minutes. The gel pieces were rehydrated using 100 µL of trypsin (200 ng, Worthington Biochemicals) in freshly prepared 100 mM ammonium bicarbonate, pH 7.4, and incubated overnight at 37 ºC. The supernatant

containing peptides from the digested sample was transferred into a new LoBind Eppendorf tube. The peptides from the gel pieces were extracted using 100 µL of 1 % formic acid: acetonitrile at a 3:1 vol/vol ratio. After three subsequent extractions, the pooled sample was lyophilized overnight. The lyophilized sample was resuspended in 28 µL of 1% formic acid, of which 8 µL was subjected to liquid-chromatography tandem mass spectrometry (LC-MS/MS) experimental run.

LC-MS/MS analysis was performed on a ThermoFinnigan LTQ linear ion trap mass spectrometer coupled to an Agilent 1290 Infinity UPLC system. The peptides from the resuspended sample were separated on a 60-minute gradient of 20% solvent A (water + 0.1% formic acid) to 90% solvent B (methanol + 0.1% formic acid) at a flow rate of 40 µL/minute using an in-house-packed C18 reversed-phase column (500 µm X 6 cm). The capillary temperature was set to 250 ºC, and the electrospray voltage was set at 3.78 kV. Data acquisition involved data dependent MS from 400 to 2000 m/z (mass/charge) followed by MS/MS on the three highest intensity masses from MS using dynamic exclusion. The raw data files were retrieved from XCaliber software and converted into the MGF format using the MSConvert utility software for analysis.

2.5 Probing Mg^{2+}/Mn^{2+} and Ca^{2+} and simvastatin affinity using differential scanning fluorimetry (DSF)

A thermal shift assay using a differential scanning fluorimetry (DSF) was used to determine the binding affinities of Mg^{2+}, Mn^{2+}, $Ca^{2+,}$ and simvastatin to the αX I-domains. Stock solution of SYPRO orange (Bio-Rad; catalogue number 170-3120) was 5000X solution in 100% (vol/vol) DMSO. Before setting up the reaction in the 96-well polymerase chain reaction (PCR) plate, a master reaction mix including the αX I-

domain, 20X SYPRO orange dye and the buffer (20 mM Hepes, 150 mM NaCl, pH 7.5 in chelex-treated water) was prepared such that each well received 5 µg (11.37 µM) of the protein. This dye was added to the reaction mix such that its dilution prevented damage from the high concentration of DMSO contacting the protein of interest. Different stock concentrations of the cations (Mg^{2+}, Mn^{2+}, and Ca^{2+}) were prepared via serial dilution and subsequently added to each well, avoiding air bubbles in the process. The total reaction volume per well in the PCR plate was 20 µL by adding 10 µL of the master reaction mix and 10 µL of the cation containing buffer. The PCR plate was spun down to eliminate any remaining bubbles using Sorvall tabletop centrifuge at 200 x g at room temperature for 3 minutes. The prepared PCR plate was set up in the CFX96 touch real-time PCR (Bio-Rad) using the preset "HEX" channel for fluorescence excitation and emission. The fluorescence was measured at regular intervals with the temperature gradient of 0.1 ºC per minute over a temperature range spanning from 15 ºC to 95 ºC, an approximately 16 hours run. After the run, the results were saved on the excel spreadsheet and analyzed. The binding profiles were fitted using Prism 7. The reaction mixture with the αX I-domain, SYPRO orange, and buffer in the absence of cations was the experiment's positive control. The negative control included a protein mixture with the αX I-domain and the buffer without the SYPRO orange dye. Four replicates were performed for the data collection. To ensure that the ionic strength did not affect the protein's melting temperature, the thermal unfolding of the αX I-domain was monitored at increasing concentrations of NaCl, which always matched the ionic strength introduced by $MgCl_2$.

2.5.1 SYPRO orange binding event probed by stopped flow fluorescence

The stopped-flow experiments were conducted on the pneumatically driven Olis RSM 1000 fluorescence spectrophotometer. The responses from the dual-channel photomultiplier tubes were recorded at specific voltages at 907 V and 420 V. Out of the two reservoir syringes, one contained the 20X SYPRO orange, and the other held the protein of interest (αX I-domain or lysozyme at a concentration of 22.74 μM) in size exclusion buffer (20 mM Hepes, 150 mM NaCl, pH 7.5 prepared in chelex-treated water). All buffers used for the experiments were filtered and degassed thoroughly. The excitation and emission wavelengths were set at 472 nm and 570 nm, respectively, to detect the SYPRO orange fluorescence. 500 μL of the two samples in the ratio of 1:1 (vol/vol) were injected to rapidly mix in the observation Peltier cell, where the changes in fluorescence were measured using 0.12 mm slit and at 1000 scans/second. The fluorescence change was observed for 300 seconds for the αX I-domain and 900 seconds for lysozyme. Subsequently, the experiments using a buffer or DMSO ranging from 1% to 10% were used as a negative control for fluorescence detection. Each of these solutions was loaded in the first syringe, and 20X SYPRO orange was loaded in the second syringe to conduct the stopped-flow experiment at 20 ºC, 40 ºC, and 60 ºC. The fluorescence was observed for 500 seconds. The fluorescence of proteins was measured at different temperatures in the range of 20 ºC to 70 ºC. The temperature in the stopped-flow module set-up was maintained via the Julabo F-30C water bath . The flow firing box connected to the high-pressure gas sources was maintained to achieve 75 psi of pressure.

2.5.2 pH-dependent denaturation of the αX I-domain

The fluorescence change as a function of temperature was used to deconvolute an equilibrium constant of αX I-domain unfolding (K_u) at different pH values. This equilibrium constant, in turn, allowed the Gibbs free energy of unfolding to be calculated near the protein's melting point. Subsequently, it was possible to extrapolate and estimate the Gibbs free energy of unfolding at any temperature.

Using the equilibrium constant, we calculated the Gibbs free energy of unfolding at standard conditions by implementing the equations and method laid out by Wright and his group (115). The DSF fluorescence datafile "melt curve amplification results" was used to fit the data using the "Sigmoid" model function (Equation 1.1) and "Midpoint Analysis" on the website http://paulsbond.co.uk/jtsa/#/input. Estimates of melting temperature (T_m) were obtained as the point of inflection portion of the DSF curve. F_{max} and F_{min} were the maximum and minimum fluorescence values, respectively. T was the absolute temperature value at each fluorescence intensity, T_m was the temperature midpoint between minimal and maximal fluorescence, "a" was a parameter to characterize the breadth of the transition, and c was an asymmetry factor that allowed different gradients around the minimum and maximum fluorescence.

$$F_{calc} = F_{min} + \frac{F_{max} - F_{min}}{(1 + e^{(Tm - T)a})^c} \qquad \text{Equation 1.1}$$

The fraction of the protein that remained folded (P_f) was calculated at each temperature using Equation 1.2, which assumed a two-state model for protein denaturation. The value of F_{max} was the calculated fluorescence intensity of the fully

denatured protein where P_f was zero, and the measured value for F_{min} coincided with P_f equal to 1.

$$P_f = 1 - \frac{F - F_{min}}{(F_{max} - F_{min})} \qquad \text{Equation 1.2}$$

Using the fluorescence intensity at the melting temperature (F_{Tm}) and the definition that at T_m, 50% of the protein is folded, F_{max} was calculated using Equation 1.3.

$$F_{max} = (F_{Tm} - F_{min}) + F_{Tm} = 2F_{Tm} - F_{min} \qquad \text{Equation 1.3}$$

Assuming that the native protein fraction and unfolded protein fraction equal to 1, we achieved Equation 1.4.

$$P_u = 1 - P_f \qquad \text{Equation 1.4}$$

The equilibrium constant of protein unfolding (K_u) was then calculated using the relationship in equation 1.5.

$$K_u = \frac{P_u}{P_f} \qquad \text{Equation 1.5}$$

The Gibbs free energy of unfolding ($\Delta_u G$) was calculated using Equation 1.6, where R was the universal gas constant (8.314 $JK^{-1}mol^{-1}$), T was the absolute temperature value at each fluorescence intensity, and K_u was the equilibrium constant of unfolding at temperature T as calculated in Equation 1.5.

$$\Delta_u G = - RT \ln K_u \qquad \text{Equation 1.6}$$

The $\Delta_u G$ values calculated via Equation 1.6 were plotted against temperature values in the range of 10-50% unfolded protein. Solving for the linear equation of best fit

allowed $\Delta_u G$, $\Delta_u H$, and $\Delta_u S$ at each temperature to be calculated. The values of the R^2 in our linear plots were at 0.95 or above, which showed that the methodology was valid for the protein studied.

Similarly, the standard Gibbs free energy ($\Delta_u G^o$) of protein unfolding was determined as the value of $\Delta_u G$ extrapolated back to 298 K using the line of best fit from the plot of $\Delta_u G$ versus temperature.

Once $\Delta_u G^o$ was determined, the standard entropy of protein unfolding ($\Delta_u S^o$) was determined using Equation 1.7, where T = 298 K.

$$\Delta_u S^o = \frac{\Delta_u G^o}{T_m - T} \qquad \text{Equation 1.7}$$

The enthalpy of protein unfolding ($\Delta_u H^o$) was then calculated using the relationship shown in Equation 1.8.

$$\Delta_u H^o = T_m \, \Delta_u S^o \qquad \text{Equation 1.8}$$

2.6 Assessing thermal stability of the αX I-domain at different Mg^{2+} concentrations using differential scanning calorimetry (DSC)

The stability of the αX I-domains was further characterized by measuring the heat change associated with the protein's thermal denaturation. This experiment was carried out using the microcalorimeter PEAQ-differential scanning calorimetry (Malvern Panalytical) at a constant heat rate. Immediately before the experiment, $MgCl_2$ at different concentrations were mixed with 45.5 μM of the αX I-domain and placed on autosampler 96 well plate in MicroCal PEAQ-DSC at 4 ºC. The experiment was performed at a temperature range from 15 ºC to 70 ºC and a scan rate of 60 ºC per hour in the passive feedback mode. A 10-minute pre-scan thermostat mode was considered for the baseline equilibration. Data were analyzed using PEAQ-DSC software, which

included buffer subtraction from protein sample scan, baseline subtraction of heat capacity difference between baselines of pre-transition and post-transition, and concentration normalization. I am thankful to Dr. Muneera Beach at Malvern Panalytical for DSC data acquisition.

2.7 Determination of Mg^{2+}, Mn^{2+}, and Ca^{2+} affinity to the αX I-domain using isothermal calorimetry (ITC)

The heat change associated with the binding of the αX I-domain to the cations (Mg^{2+}, Mn^{2+}, and Ca^{2+}) was determined using isothermal calorimetry. The αX I-domain samples were loaded into MicroCalorimeter PEAQ-ITC (Malvern Panalytical) with a cell volume of 200 µL. Loading buffer for the αX I-domains was comprised of 20 mM Tris, 150 mM NaCl, pH 7.5, at concentrations of 100 µM (WT) and 50 µM (SILEN). For the WT αX I-domain, titrations with cations - Mg^{2+} at 7.5 mM, Mn^{2+} at 4 mM, and Ca^{2+} at 20 mM in matching/identical buffer were monitored for 38 injections of 0.5 or 1 µL with continuous stirring at 25 ºC. 1 µL of the cations - Mg^{2+} at 3.7 mM and Mn^{2+} at 2 mM in matching buffer were titrated for 38 injections to the SILEN αX I-domain. The titration curve for enthalpy of the reaction (ΔH^0) (kcal/mol) against the molar ratio of cation to the αX I-domain was generated from each injection of cation resulting in an integrated heat pulse and concentration normalization. The resulting isotherm was thus utilized to generate the cation affinity (K_D) by plotting the ΔH_0 against the cation concentrations.

2.8 Probing Mg^{2+}-dependent structural changes of the αX I-domain using circular dichroism (CD)

The circular dichroism spectra were obtained on an Olis DSM 1000 CD built around a double grating RSM monochromator and calibrated with 2.4 mM ammonium

(+)-10-n-camphorsulfonate, which has a negative peak at 192.5 nm and positive peak at 290.5 nm. Experiments were conducted at 10 μM concentration of the αX I-domain in a 1 mm cuvette using 2400 lines/mm grating and slit of 1.24 mm width. The CD measurements were carried out in wavelength ranging from 200 nm to 270 nm, followed by normalization against the buffer spectra. Each spectrum was an average of four scans. The mean residue molar ellipticity was calculated from the observed ellipticities according to the following equation:

$$[\theta] = (\theta o \text{ x } \text{MRW }) / (10 \text{ x } l \text{ x } c)$$

where $[\theta]$ was the mean residue molar ellipticity in deg. cm^2. $dmol^{-1}$, θo was the observed ellipticity in millidegrees, MRw was the mean residue weight of the αX I-domains (molecular mass / (Number of amino acids -1)), l was the path length in centimeters, and c was the αX I-domain concentration in g/L. The secondary structure content was calculated using the CD Pro suite reference set SP37A to compare the spectra of the αX I-domain. Three different algorithms, SELCON, CONTIN-LL, and CDSSTR, were implemented for the analysis (116).

2.9 Small angle X-ray scattering (SAXS)

The SAXS experiments were conducted on the αX I-domain at different concentrations of Mg^{2+}.

2.9.1 Static SAXS

A large stock volume (~5 L) of the buffer (20 mM Hepes, 150 mM NaCl, pH 7.5 in chelex-treated water) was prepared, and the αX I-domain was purified with the identical buffer in the last step of purification in size exclusion chromatography (SEC). The SEC eluted fractions of the αX I-domain were concentrated and spun down to remove

precipitations such that a final αX I-domain stock concentration of 2.5 mg/mL was obtained. Another buffer comprising exact buffer constituents but supplemented with 1 M $MgCl_2$ was prepared. Next, each buffer at different $MgCl_2$ concentrations was prepared by serial dilution of the buffer containing 1 M $MgCl_2$. For instance, 250 mL of $MgCl_2$ containing buffer was prepared by mixing the SEC buffer (20 mM Hepes, 150 mM NaCl, pH 7.5 in chelex-treated water) and serially diluted with buffer containing $MgCl_2$. Hence, 11 sets of 250 mL buffer were prepared at different $MgCl_2$ concentrations (Table 4).

Table 4: Concentration of WT αX I-domain at different $MgCl_2$ concentrations used for SAXS experiments

Mg^{2+} concentrations	αX I-domain (WT) concentrations (mg/mL)
0 μM	1.92
20 μM	2.00
100 μM	2.02
250 μM	1.65
500 μM	1.45
3 mM	1.51
10 mM	1.30
20 mM	2.07
60 mM	1.76
100 mM	1.92
250 mM	1.47

Next, 500 μL of the 2.5 mg/mL αX I-domain was placed in a dialysis bag of 10 kDa molecular mass cut-off (Sigma-Aldrich) and dialyzed in each of the 500 mL buffers containing respective $MgCl_2$ concentrations. The dialysis was carried out overnight with gentle stirring at 4 ºC. The resulting αX I-domain sample was spun to remove any

precipitation, aliquoted at 70 µL each for three replicates, frozen in liquid nitrogen, and stored in -80 ºC. We observed by SEC that freezing of the αX I-domain samples at each $MgCl_2$ concentration did not alter the elution profiles compared to samples at 4 ºC. The αX I-domain concentrations used for the SAXS analysis at each $MgCl_2$ concentration are listed in Table 4.

The reference buffer for each $MgCl_2$ concentration was the respective buffer in which the αX I-domain was dialyzed in. The static SAXS experiments on the prepared samples were collected using National Synchrotron Light Source-II (NSLS-II) Beamline 16-ID (LiX) at Brookhaven National Laboratory. I am thankful to Dr. James Byrnes for SAXS-data acquisition.

2.9.2 Size exclusion chromatography (SEC)-SAXS

The 22 kDa αX I-domain was purified by following the methods described in Section 2.1. A large stock of volume (~7 L) of the buffer (20 mM Hepes, 150 mM NaCl, pH 7.5 in chelex-treated water) was prepared, and the αX I-domain was eluted by size exclusion chromatography (SEC) in the same buffer. Another buffer comprising the exact buffer constituent along with 1 M $MgCl_2$ was prepared. The running buffer at each $MgCl_2$ concentration was prepared by serial dilution. For the SEC-SAXS experiment, 100 µL of 10 mg/mL αX I-domain was injected into the Superdex S200 column for each experimental run. The running buffer was the SEC buffer (20 mM Hepes, 150 mM NaCl, pH 7.5) containing respective $MgCl_2$ concentrations.

2.10 Surface plasmon resonance (SPR) assay

The preparation of C1 sensor chips (Cytiva; product number BR100540) and all SPR- based interaction studies were performed on a Biacore X100 instrument (GE

Healthcare) at 25 ºC using buffer filtered using 0.22 µm filters. The C1 sensor chip consists of a flat carboxylated surface with no dextran binding (117) which alleviated the non-specific binding. The pH scouting for each ligand was conducted using 10 mM sodium acetate at pH values of 3.5, 4, 4.5, 5, 5.5, and 6. The preconcentration analysis for the ligands was conducted at ligand concentrations of 10 µg/mL, 20 µg/mL, 50 µg/mL, and 100 µg/mL. This C1 sensor chip was activated by injecting 0.4 M of 1-ethyl-3-(3-dimethylamino) propyl carbodiimide (EDC) (Thermo Fisher Scientific; catalogue number 77149) and 0.1 M of N-hydroxy succinimide (NHS) (Thermo Fisher Scientific; catalogue number 24500) in 1:1 vol/vol ratio for 400 seconds at 5 µL/minute flow rate. Immobilization of each ligand (fibrinogen and iC3b) to each covalently activated C1 sensor chip was performed using 50 µg/mL ligand concentration in 10 mM sodium acetate at pH 4.5. The ligand immobilization achieved sensogram signals of 5500 RU and 1500 RU for fibrinogen and iC3b, respectively, through amine coupling at a flow rate of 5 µL/minute.

As a reference, a flow cell was activated using 0.4 M EDC and 0.1 M NHS at a 1:1 vol/vol ratio. The sensor chip surface was then blocked with ethylenediamine in series with the ligand-coupled flow cell activation. SPR affinity analyses to examine the interaction of the 10 µM αX I-domains with the ligand-coated or control surface were performed in running buffer containing 20 mM Hepes, 150 mM NaCl, pH 7.5 prepared in chelex-100 treated water and respective Mg^{2+} concentration. After each measurement, surfaces were regenerated in 100 mM Hepes, 1.5 M NaCl, 150 mM EDTA at pH 7 and pH 8 for fibrinogen and iC3b, respectively. The αX I-domain samples were diluted in Hepes/Mg^{2+} buffer for respective Mg^{2+} concentration and injected in random series of 11

concentrations (39 nM - 40 μM) at a flow rate of 10 μL/minute. The time-course of binding was observed for 450 seconds, the dissociation process observed for 400 seconds, followed by regeneration for 230 seconds.

2.11 SPR BIAevaluation and EVILFIT

The equilibrium dissociation constant (K_D) was calculated by steady-state analysis using the Biacore X100 evaluation software- BIAevaluation after subtracting the response on the control surface from the signal obtained on the ligand-coated surface. The sensograms were preprocessed with baseline adjustment and by setting an injection time fixed at a particular value. Data analysis was further conducted with the software EVILFIT (118, 119). For a more robust data adjustment, each sensogram was correctly aligned for the observed injection start point using the software Scrubber. The net binding traces for each experimental SPR run were loaded into the EVILFIT. The affinity traces in each data set were globally fit for all concentrations. Next, to obtain a 3D contour plot, the data were fit using the Tikhonov regularization algorithm. The distributions' boundaries were uniformly set to k_{off} values in the interval from 10^{-9} to 10^{0} sec^{-1}, and K_D values in the interval from 10^{-9} to 10^{0} M.

2.12 Nuclear magnetic resonance (NMR)

2.12.1 Heteronuclear single quantum spectroscopy (HSQC)

The final buffer for the sample was 20 mM sodium phosphate, 150 mM NaCl, 5 mM $MgCl_2$, 5% D_2O, pH 6.5. NMR experiments for ^{15}N-labeled SILEN αX I-domain were conducted on Bruker 800 MHz (Bruker Instruments, Inc.) using TCI cryoprobe. The starting volume of the NMR sample for the ^{15}N-labeled SILEN αX I-domain was 500 μL. For titration of ^{15}N-labeled SILEN αX I-domain with simvastatin, 100 μM SILEN αX I-

domain was mixed with different volumes of 10 mM hydroxy-acid simvastatin stock solution (Insolution™ Simvastatin; Sigma Aldrich catalog number 567022) at 12 different simvastatin concentrations of 10 μM, 49.8 μM, 147.8 μM, 243.9 μM, 338.2 μM, 430.6 μM, 521.3 μM, 697.7 μM, 783.4 μM, 867.6 μM, 1.03 mM, and 1.18 mM. At each increment in the titrations, a ^{1}H-^{15}N HSQC spectrum was acquired individually. The chemical shift changes in the ^{1}H-^{15}N spectrum were measured and normalized to a single value using Equation 2.1 in which $\Delta\delta_H$ and $\Delta\delta_N$ represent the chemical shift changes in the ^{1}H and ^{15}N dimensions, respectively, in ppm. Titrations were analyzed assuming that the observed chemical shift perturbation ($\Delta\delta$) was the weighted average between the two extreme values corresponding to the free ($\Delta\delta$ = 0) and simvastatin-bound states ($\Delta\delta = \Delta\delta^{max}$) using Equation 2.1. The αX I-domain was predicted to have a single binding site for simvastatin following the reaction shown in Equation 2.2, where X is the αX I-domain and S is simvastatin. The titration data was fit non-linearly against the theoretical 1:1 model of protein-drug equilibrium, as shown in Equation 2.3 to calculate the dissociation constant (K_D).

$$\Delta\delta = \sqrt{\left(\Delta\delta_H{}^2 + \frac{1}{25}\Delta\delta_N{}^2\delta\right)/2} \qquad \text{Equation 2.1}$$

$$X + S \rightleftarrows XS \qquad \text{Equation 2.2}$$

$$K_D = \frac{[X][S]}{[XS]} - [X_0] - [S_0] + [XS] \qquad \text{Equation 2.3}$$

$$\Delta\delta = \frac{[XS]\,\Delta\delta^{max}}{[X_0]} \qquad \text{Equation 2.4}$$

$$\Delta\delta = (\Delta\delta_F\,(([X_0] + [L_0] + Kd - \sqrt{([X_0] + [L_0] + K_d)2 - 4[P_0][L_0])/\,2\,[P_0]}$$

Equation 2.5

$[X_0]$ and $[S_0]$ were the total concentrations of the αX I-domain and simvastatin, respectively. [XS] was the steady-state complex concentration at equilibrium. Since the

1:1 model has chemical perturbation ($\Delta\delta$) as shown in Equation 2.5, the final chemical perturbation ($\Delta\delta$) was calculated using Equation 2.5, where ($\Delta\delta^{\max}$) and K_D were fit with nonlinear regression. All ^{1}H-^{15}N HSQC data were processed using NMRPipe and analyzed using Sparky software. The experiments were conducted at the KECK Institute for Molecular Design facility at the University of Houston.

2.12.2 Saturation transfer difference (STD)

The SILEN αX I-domain was expressed and purified, as described in Section 2.1. 25 μM of the SILEN αX I-domain at a volume of 500 μL was used for the STD experiment. The final buffer for the αX I-domain sample was 20 mM sodium phosphate, 150 mM NaCl, 10% D_2O, 5 mM $MgCl_2$, pH 7.5. 1 mM simvastatin was used for the experiments such that for the on-resonance experiment, the concentration of the SILEN αX I-domain to simvastatin was at the ratio of 1:40. The on-resonance irradiation of the SILEN αX I-domain by selective saturation was performed at the upfield region between 0.5 to 0.1 ppm. Off-resonance irradiation was applied at 15 ppm, where no protein signals were present. 1D STD NMR spectra were multiplied by an exponential line broadening function of 1-3 Hz prior to Fourier transformation. The water suppression by gradient tailored excitation (WATERGATE) scheme was employed for suppression of the residual HDO signal. The experiments were carried out on Bruker 800 MHz (Bruker BioSpin GmbH) at the NMR facility at the University of Texas Medical Branch.

CHAPTER 3

ASSOCIATION OF THE αX I-DOMAIN SHAPE-SHIFTING WITH LIGAND INTERACTIONS AS A FUNCTION OF CATION BINDING.

3.1 Introduction

Integrins undergo highly complex conformational alterations (120). Activation of integrins involve conformational change of the αI-domain from the closed to an open state. This transition regulates integrin affinity (84). In integrin αXβ2, the interaction of the αX I-domain with an acidic residue of its ligand requires a divalent cation. Physiologically, Mg^{2+} is present at MIDAS and plays a key role in coupling between MIDAS and the αXI-α7 helix. This coupling is the essence of the shape-shifting event of the αX I-domain, a process regulating αX I-domain ligand affinity, thus αXβ2 functions (79). The fact that the divalent cations modulate the function of integrins differently has been a long-standing observation, as Mg^{2+} uniformly facilitates, Ca^{2+} generally inhibits and Mn^{2+} universally enhances interactions with their cognate ligands. However, understanding on the regulation of the αX I-domain conformation, affinity in account to cation binding has been limited. Structural information has been provided through several structures of the αI-domains (79, 87, 103, 121), but we used “in-solution” techniques to characterize how divalent cations, mostly Mg^{2+}, alter the αX I-domain conformation and affinity.

Surface-expressed leukocyte integrin αI-domains fused to an artificial transmembrane helix have shown to undergo conformational change and demonstrated that the αI-domain is sufficient for adhesion of the fused complex to its ligand (122, 123). Therefore, the recombinantly expressed αX I-domain should exhibit typical

features of αXβ2 regarding conformational changes and ligand affinity irrespective of the rest of the αXβ2 structure. In our studies, we used the WT isolated along with a high-affinity SILEN mutant αX I-domain which represent the closed and the open state, respectively. The closed conformation is adopted in the absence of ligand binding and is known to be stabilized by small molecules that antagonize ligand binding (14, 124). In the closed αX I-domain, the side chain of the critical Ile 314 residue in the C-terminal α7 helix is associated with the hydrophobic pocket of the αX I-domain (also known as socket of Isoleucine–SILEN) whereas in the open αX I-domain, the Ile 314 is displaced from the hydrophobic pocket. The working model for an open state αX I-domain in our studies is designed with the mutation Ile 314 Gly, which disrupts the contact between the α7 helix and the αX I-domain body. This Ile 314 Gly-based switch controls αX I-domain conformation allosterically and represents the endpoint of the high ligand-binding affinity of the αX I-domain structure (103). The Ile 314 Gly-mutant will be referred to as the SILEN αX I-domain in our studies.

My hypothesis is that there exists a dynamic conformational equilibrium between αX I-domain closed and open states even in an absence of a ligand, and addition of Mg^{2+} allows the αX I-domain to advance to a binding-competent state. In my studies illustrated in upcoming Section 3.2, we implemented the following techniques for biophysical characterization of the WT and SILEN αX I-domain in relation to cation and ligand affinity, respectively. We specifically aim to investigate how Mg^{2+} alters conformational dynamics and structural stability of the αX I-domain in solution which in turn regulates the ligand affinity. These structural and biophysical characterizations of

the αX I-domain have the potential to provide an understanding to the overall complex functioning of the αXβ2.

Isothermal Calorimetry (ITC). ITC measures the heat change upon interaction of two substances. Each injection of a cation to the αX I-domain resulted in a heat pulse that was integrated with respect to time and normalized to generate a titration-fit curve. The titration curve represents the change in enthalpy (ΔH) versus the molar ratio of the cation to the αX I-domain (Figures 10A, B). The resulting isotherm was fit to a binding model to obtain the affinity of each cation to the αX I-domain which is represented by dissociation constant (K_D) of binding (125).

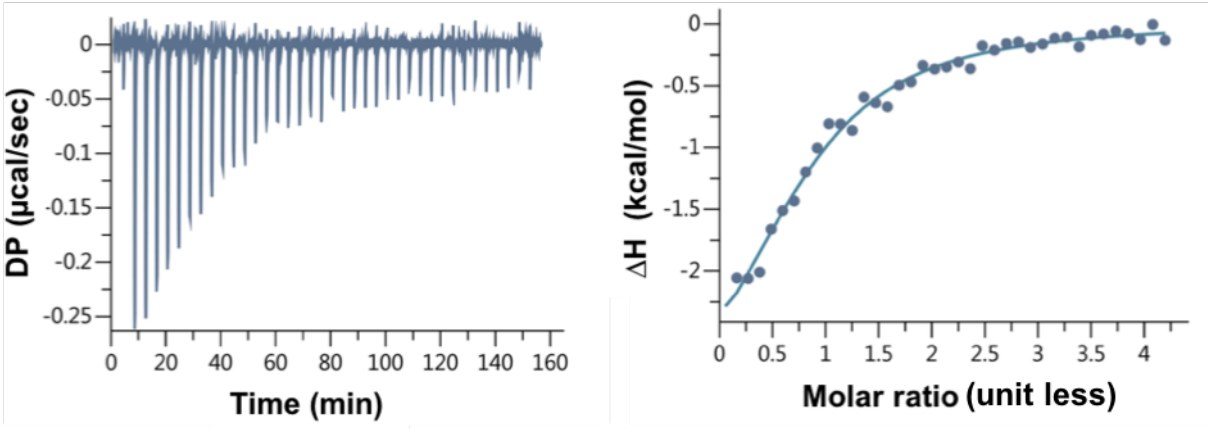

Figure 10: Representation of ITC experimental curves. (A) Heat signature of ligand and analyte binding resulting from each injection of the ligand. **(B)** Titration curve generated from integration of heat signature with respect to time and fitted to a binding model.

Differential Scanning Calorimetry (DSC). DSC relies on a direct assessment of the heat energy uptake. The amount of heat radiated or absorbed by the αX I-domain was measured on the basis of a temperature difference between the protein sample and the reference buffer. Changes in the heat capacity (C_p) occurs from the disruption of molecular forces that stabilizes the native structure of the αX I-domain. Moreover, integration of the C_p at constant pressure as a function of temperature generated the

change in enthalpy of unfolding (ΔH) of the αX I-domain as a result of its heat denaturation (126). ΔH is represented by the total integrated zone shown in the thermogram peak (Figure 11). The thermogram peak denotes the transition midpoint as the melting temperature (T_m) where 50% of the molecules are folded and 50% of the molecules are unfolded (Figure 11). The assumptions used for mathematical modelling was the reversible two-state denaturation model based on the calculation of van't Hoff's enthalpy.

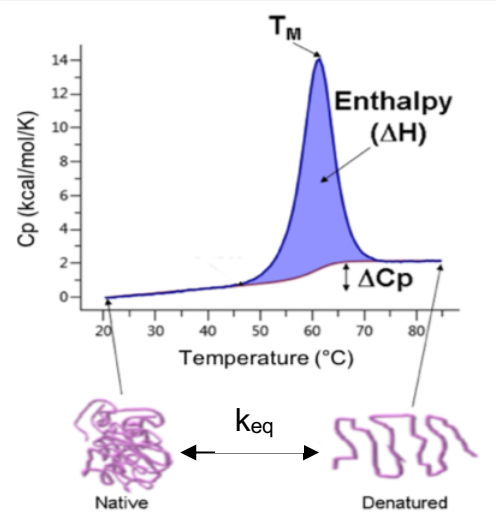

Figure 11: Illustration of thermal unfolding profile of a protein using DSC.

Differential Scanning Fluorimetry (DSF). A DSF thermal melt experiment is used to observe protein unfolding with high multiplicity in the presence of ligands. The temperature at which proteins unfold was measured by substantial increase in fluorescent intensity of a merocyanine dye, SYPRO orange, which has affinity to hydrophobic residues (Figure 12) (127). We employed this technique to extract the Gibbs free energy of unfolding ($\Delta_u G$), enthalpy of unfolding ($\Delta_u H$), and entropy of unfolding ($\Delta_u S$) from the slope of the unfolding transition curve, in varying Mg^{2+} concentrations, ionic strength, and pH (115).

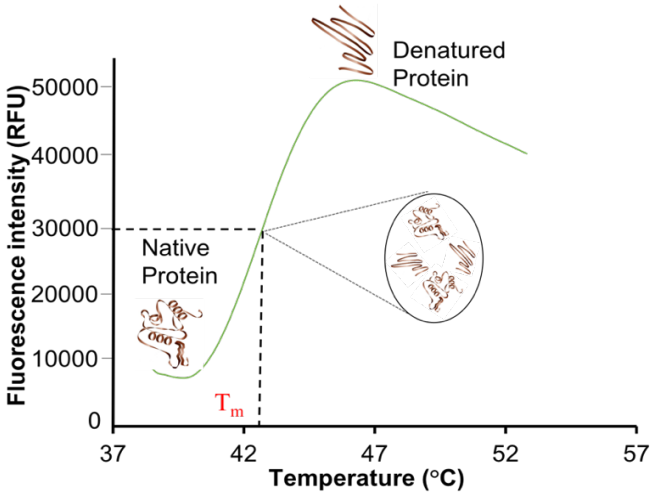

Figure 12: Schematic representation of thermal shift assay. DSF showing increase in fluorescence intensity due to dye binding to the hydrophobic residues of unfolded protein upon thermal denaturation.

Circular Dichroism (CD). CD is a biophysical method for swift assessment of protein secondary structural changes during binding and folding-unfolding events. CD is defined as the unequal absorption of left-handed and right-handed circularly polarized light upon interaction of asymmetric molecules with light (128). The α-helical proteins exhibit negative bands at 222 nm and 208 nm with a positive band at 193 nm. Negative bands at 218 nm and positive bands at 195 nm are characteristics of well-defined antiparallel β-sheets. Disordered proteins display low ellipticity above 210 nm and negative bands near 195 nm (Figure 13). With these characteristic secondary structure distinctions, CD is used to ascertain if the protein is properly folded in solution. Its application can be extended to examine if the protein's conformation is affected by a mutation or additives binding to the protein, given that there is no CD effect (129).

The validity and the limitations of various empirical methods developed to assess protein CD spectra for quantitative estimation of the secondary structure content has been controversial due to reasons such as non-peptidic chiral molecules in buffer. To

improve the reliability of CD data, the CD spectra were extensively analyzed using three methods-SELCON3, CONTIN-LL, and CDSSTR which determined the secondary structure content of the αX I-domain. These prediction methods are based on comparison of secondary structural content to different reference protein sets with large representation of CD spectral features at various wavelengths and structural combinations (116).

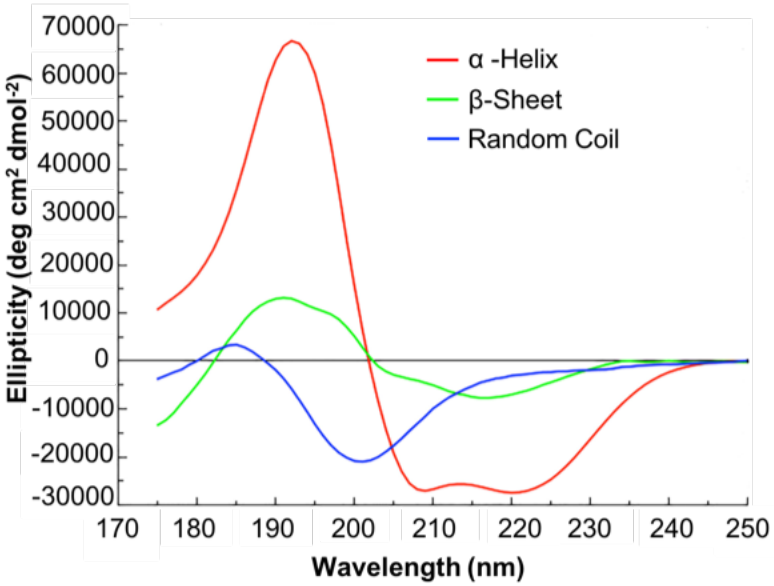

Figure 13: Standard CD spectra showing distinct characteristics of the α-helix, β -sheet, and random coil.
Adapted from David M. Rogers et al. (2019). Electronic circular dichroism spectroscopy of proteins. Chem., 5 (11), 2751-2774.

Small Angle X-ray Scattering (SAXS). SAXS is a solution technique whereby the scattering of X-rays upon interaction with a biomolecule is monitored. The resulting scattered pattern provides low-resolution quantitative structural information about the size, shape, and structural transitions of the biomolecule via the characteristic parameters such as molecular weight, maximum dimension (D_{max}), and the radius of gyration (R_g). D_{max} is the maximum intraparticle distance and R_g is a measurement of

the overall size of the protein. R_g is the average root-mean-square distanced to the center of density in the protein weighted by the scattering length density. The smaller the R_g, the more compact the shape of the protein is (130). A reliable SAXS analysis requires protein solution without aggregates termed as a monodisperse solution.

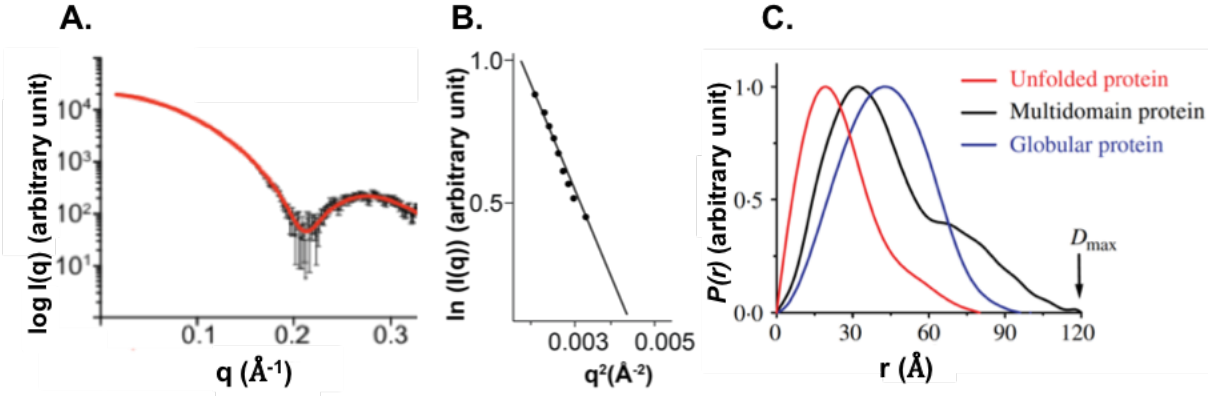

Figure 14: Illustration of raw SAXS data and analysis (A) Measurement of scattering intensity. **B)** Guinier plot demonstrating monodispersity of a particle **(C)** pair distance distribution p(r) plot.
Figure 14C: Adapted from John A. Tainer et al. (2007). X-ray solution scattering (SAXS) combined with crystallography and computation: defining accurate macromolecular structures, conformations and assemblies in solution. Q Rev Biophys., 40 (3), 191-285.

The scattering intensity-I(q) of the αX I-domain measured in the SAXS experiment is represented as a function of momentum transfer and is given by: $I(q) \sim I(0) \exp(-q^2 Rg^2/3)$. Here, I(0) is the forward scattering intensity defined by Guinier region of SAXS (Figure 14A). q is the scattering vector magnitude determined by using $q = (4\pi/\lambda)\sin\theta$ in which θ is half the scattering angle and λ the wavelength of the incident radiation. The q-range is the range between q_{min} and q_{max} defined by the experimental set-up that allows us to investigate the density fluctuations in the protein sample. Determination of I(q) considers the scattering amplitude which is a Fourier transform of the excess electron density: the difference between the electron density of the αX I-domain and the solvent (131).

The Guinier approximation of the plot of I(q) versus q transforms the Guinier region into a characteristic line for visual inspection of data for Guinier analysis. In this plot, the low-q region of the scattering curve is characteristic for the overall dimension of the particle (Figure 14A). The Guinier plot of ln[*I(q)*] versus q^2 is a linear function for a particle of any shape (Figure 14B). The slope of the Guinier plot is used for determining the R_g and the intercept provides the forward scattering I(0), which is proportional to the molecular weight and the concentration of the protein. Any deviation from the straight line or a lack of linearity in the Guinier plot indicates a lack of monodispersity or intermolecular interactions (131).

One of the representations of conformational change of the αX I-domain in our studies uses the pair-distribution p(r) function, which is a histogram of distances between pairs of points within the particle (Figure 14C). A Fourier transform of the p(r) function provides the scattering pattern of the particle. The p(r) is analyzed for interpreting the structural properties. The αX I-domain, being a globular protein, exhibits a symmetric bell-shaped p(r) (132).

Additionally, SAXS data can be used to obtain information on overall protein flexibility. The momentum transfer which is the modulus of the scattering vector is denoted by $s=4\pi (\sin\theta)/\lambda$. Typically, the Kratky plot $s^2I(s)$ as a function of s is applied to monitor degree of compactness and qualitatively distinguish globular protein from disordered state. The Kratky representation essentially allows visualization of particle features of the scattering profiles for an identification of the folding state and flexibility. For comparison of folding states of proteins, the data is normalized at I(0)=1 and with multiple of s and R_g before plotting the information about the shape of the protein.

However, in this case, the information on the size of the protein is dismissed (132). This resulting Kratky plot of normalized data is termed as a dimensionless Kratky plot (Figure 15).

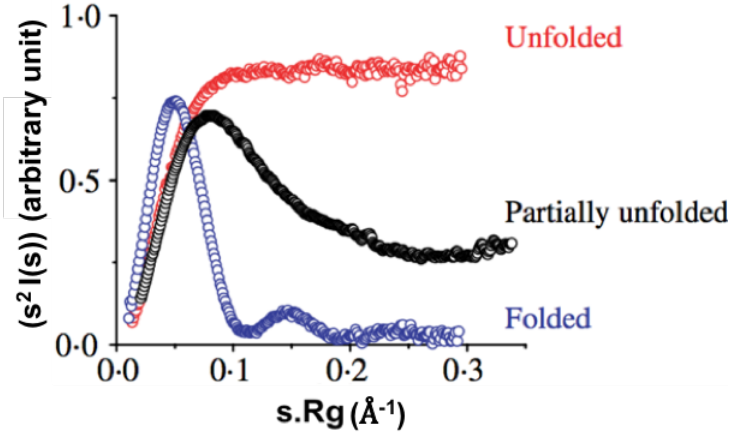

Figure 15: Representation of the dimensionless Kratky plot. Plot exhibiting bell-shaped curve for globular protein and showing a plateau instead of a peak for an unfolded protein.
Adapted from John A. Tainer et al. (2007). X-ray solution scattering (SAXS) combined with crystallography and computation: defining accurate macromolecular structures, conformations and assemblies in solution. Q Rev Biophys., 40 (3), 191-285.

Surface Plasmon Resonance (SPR). SPR uses optical methods to provide response by measuring change in the refractive index upon binding of an analyte (the αX I-domain) to the ligand covalently coupled on a sensor chip (Figure 16A). In principle, the affinity constant is measured by the equilibrium binding analysis (133). However, the SPR analysis uses an affinity constant which is simply the ratio of equilibrium of product and reactant concentrations and does not take into account the structural heterogeneity of the protein in binding to its ligand or any ligand heterogeneity on the SPR chip surface. Therefore, we implemented the EVILFIT algorithm for fitting the experimental data which integrates analysis with models allowing for heterogeneity

of binding affinity. To numerically stabilize the results against noise amplification, Tikhonov-Phillips or maximum entropy regularization is implemented in the EVILFIT data analysis (134).

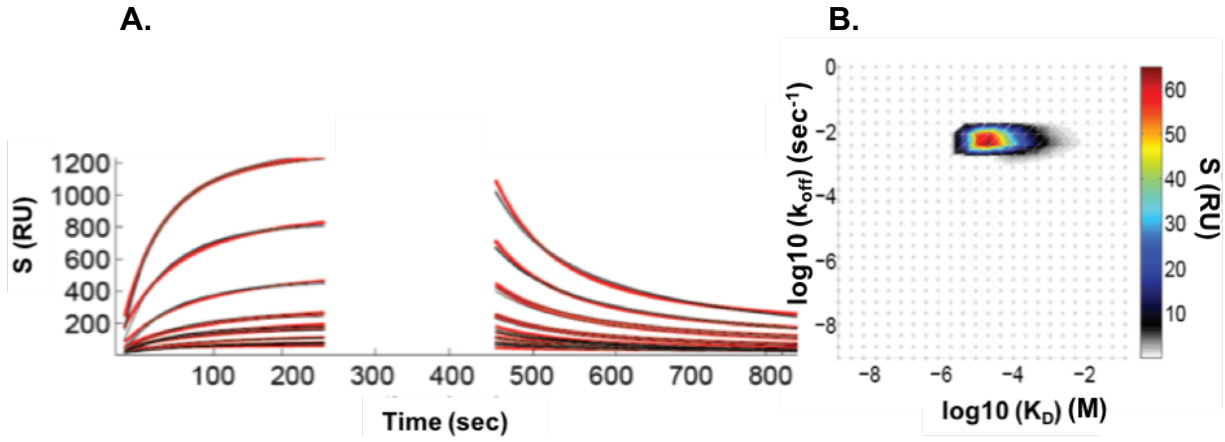

Figure 16: Analysis of SPR data. (A) SPR sensograms showing association and dissociation profile of an analyte to the immobilized ligand and **(B)** SPR binding data analyzed using Evilfit algorithm demonstrating calculated K_D-k_{off} distributions as a contour plot with the color temperature interpolated from the protein sample population.

Instead of the canonical step for characterization of αX I-domain-ligand interaction by a single pair of association (K_A) and dissociation (K_D) (Figure 16A), the EVILFIT algorithm yields a two-dimensional distribution of these constants (Figure 16B). For better representation in terms of affinity, the resulting data plot is shown as distribution of k_{off} and the equilibrium constant (K_D) in a 3D-dimensional coordinate system. The *x* and *y* axes represent the equilibrium constant-K_D (in M) and dissociation constant k_{off} (in sec^{-1}), respectively, and, a z coordinate depicts the abundance of 1:1 interactions defined by each pair of K_D and k_{off} (118). Therefore, examining the cation-dependent binding of the αX I-domain to its ligand using the EVILFIT algorithm offers an advantage by including the intrinsic structural heterogeneity of the αX I-domain.

3.2 Results

3.2.1 Purification of the WT and SILEN mutant αX I-domain.

The 47 kDa GST-fused αX I-domain was observed in the SDS-PAGE gel (Figure 17A). The cleavage of the GST-fused αX I-domain by hexameric histidine-fused human rhinovirus 3C protease resulted in the 22 kDa αX I-domain (Figure 17B). A final step of size exclusion chromatography (SEC) demonstrated that the αX I-domain was largely monomeric (Figure 17C). The identity of the protein was determined using MS-MS fragmentation using an LTQ linear ion trap mass spectrometer and verified by the detection of the unique peptide of the αX I-α7 helix within an error limit of ± 0.4 Da (Figure 18).

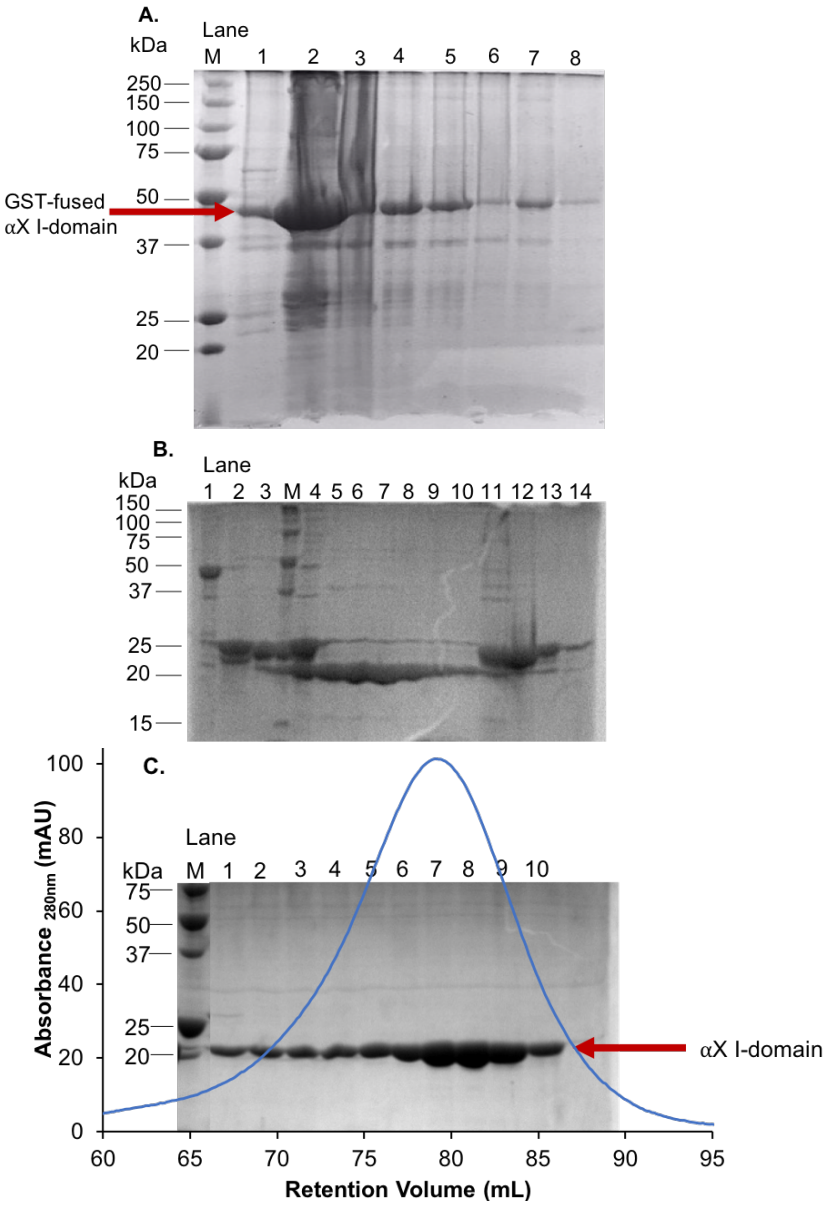

Figure 17: Monomeric 22 kDa αX I-domain obtained by affinity and size exclusion purification methods. (A) Affinity purification of the 47 kDa GST-fused αX I-domain was analyzed by SDS-PAGE (lane 1-8). **(B)** Digestion of GST-fused αX I-domain by hexameric histidine-fused human rhinovirus 3C protease revealed cleaved 22 kDa αX I-domain (lane 5-10). Controls samples of undigested GST-fused αX I-domain, 25 kDa GST protein, 23 kDa 3C protease, and protein mixture solution after digestion are shown in (lane 1-4), respectively. 3C protease elution (lane 11,12) and cleaved GST protein elution (lane 13,14) were separated by HisTrap column and GST column, respectively. **(C)** After removal of GST protein, Superdex75 size exclusion profile and subsequent SDS-PAGE demonstrated monomeric αX I-domain of 22 kDa (lane 1-10). The molecular weights of bands were compared with standard proteins (lane M).

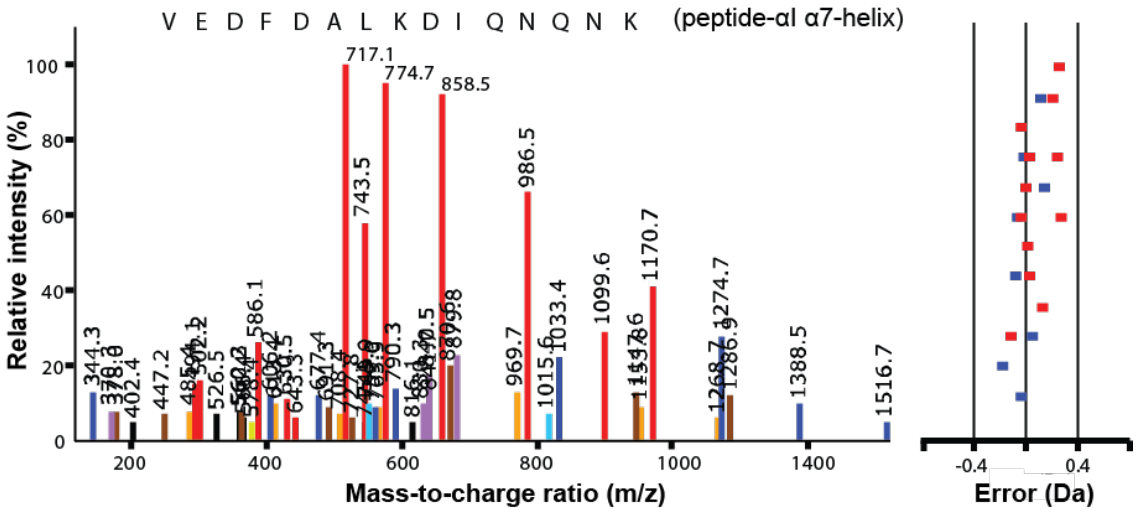

Figure 18: Identification of the αX I-domain using LC-MS/MS on linear ion trap mass spectrometry. The MS/MS product ions of the peptide (VEDFDALKDIQNQNK) of the αX I-α7 helix within an error limit of ± 0.4 Da was obtained upon MS-MS fragmentation of the αX I-domain using LTQ linear ion trap mass spectrometer.

3.2.2 Measuring cation affinities to the WT and SILEN αX I-domain.

The αX I-domain is an allosteric domain that binds to an extracellular ligand through the coordinated Mg^{2+} ion. Thus, the αX I-domain binds to Mg^{2+} and other cations. To examine if the cation affinity to MIDAS is affected by MIDAS reorganization, we determined the affinities of the WT and SILEN αX I-domain to three divalent cations, Mg^{2+}, Mn^{2+}, and Ca^{2+} by using isothermal calorimetry (ITC). In our ITC experiments, these metals were titrated to 10 μM αX I-domain. The SEC buffer was titrated to itself to serve as a negative control. Additionally, the metals were titrated to the buffer to ensure that these titrations did not result in significant changes in enthalpy.

The enthalpies of cation binding to the αX I-domain, which are predominantly driven by ionic interactions in calorimetric measurements, were utilized to determine the metal affinities. For the WT αX I-domain, 7.5 mM Mg^{2+}, 4 mM Mn^{2+}, and 20 mM Ca^{2+} were used for titration. The metal affinities to the WT αX I-domain were determined with

dissociations constants of 74 ± 3 μM, 154 ± 11 μM, and 480 ± 33 μM for Mn^{2+}, Mg^{2+}, and Ca^{2+}, respectively (Figure 19). For the SILEN αX I-domain, 3.7 mM Mg^{2+}, 2 mM Mn^{2+}, and 20 mM Ca^{2+} were used for titration. The metal affinities to the SILEN mutant αX I-domain were determined to be in the same range as the dissociation constants of 69 ± 1 μM for Mn^{2+} and 82 ± 9 μM for Mg^{2+} (Figure 19). However, titration of Ca^{2+} to the SILEN αX I-domain did not show change in heat capacity, and Ca^{+2} affinity to WT αX I-domain was 480 ± 33 μM (Figure 19C). The SILEN αX I-domain exhibited 2-fold higher affinity to Mg^{2+} than the WT αX I-domain. Given that the SILEN mutation is located in the allosteric αI-α7 helix, this two-fold affinity change suggests that the MIDAS re-coordination by Mg^{2+} may be linked to this helix. Since ΔH range of binding for each cation to the αX I-domain differed, the *y*-axis in each ITC measurement is different for providing better clarity in data presentation (Figure 19).

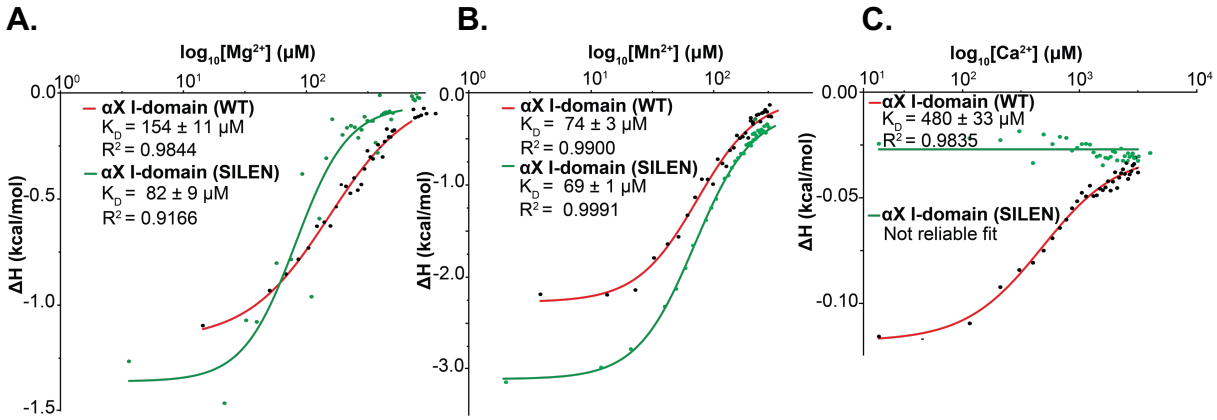

Figure 19: Affinities of divalent cations to the WT and SILEN αX I-domain were determined using isothermal calorimetry. The plots represent the change in the enthalpy upon **(A)** Mg^{2+} **(B)** Mn^{2+} **(C)** Ca^{2+}-binding to the WT αX I-domain (red line) and the SILEN αX I-domain (green line). Binding of Ca^{2+} to the SILEN αX I-domain was not observed.

Furthermore, ITC was advantageous for determining thermodynamic parameters of cation-binding to the αX I-domain. The Gibbs free energy (ΔG), enthalpy (ΔH), and entropy (ΔS) change are listed in Table 5. Based on the ΔG of binding, we distinctly

observed that the affinity of the αX I-domain was highest for Mn^{2+} followed by Mg^{2+} then Ca^{2+}.

Table 5: Values of thermodynamics parameters—Gibbs free energy (ΔG), enthalpy (ΔH), entropy (ΔS) of divalent cation affinity to the WT and the SILEN αX I-domain

αX I-domain		ΔG (kcal/mol)	ΔH (kcal/mol)	-TΔS (kcal/mol)
WT	**Mg^{2+}**	-5.17	-3.03	-2.14
	Mn^{2+}	-6.17	-2.83	-3.34
	Ca^{2+}	-4.15	-0.99	-3.16
SILEN	**Mg^{2+}**	-4.84	-5.90	1.05
	Mn^{2+}	-5.64	-8.36	2.72
	Ca^{2+}	N/A	N/A	N/A

However, interestingly, we observed a significant difference in the resulting binding entropies from metal titration to the WT and SILEN αX I-domain, respectively (Figures 20A, B). The entropic contribution favored the cation-WT αX I-domain affinity, but negatively contributed to the cation-SILEN αX I-domain binding. This entropic gain in the WT αX I-domain potentially originated from the desolvation effect involved during the MIDAS re-organization. The lower entropy observed in the SILEN αX I-domain versus the WT αX I-domain reflects that the SILEN αX I-domain exists in a higher extent of disorder compared to the WT αX I-domain. The cation binding to the SILEN αX I-domain potentially endows more order in its structure, thereby showing negative conformational entropy. The change in enthalpy was directly related to interaction of cation with electrostatically charged MIDAS residues whereas the change in entropy

was linked to disruption of hydrophobic interactions or water displacement or both during Mg^{2+}-induced αX I-domain conformational changes. Moreover, competition binding assay using two different cations' binding to the αX I-domain would provide more reliable insight on the metal-affinity determination.

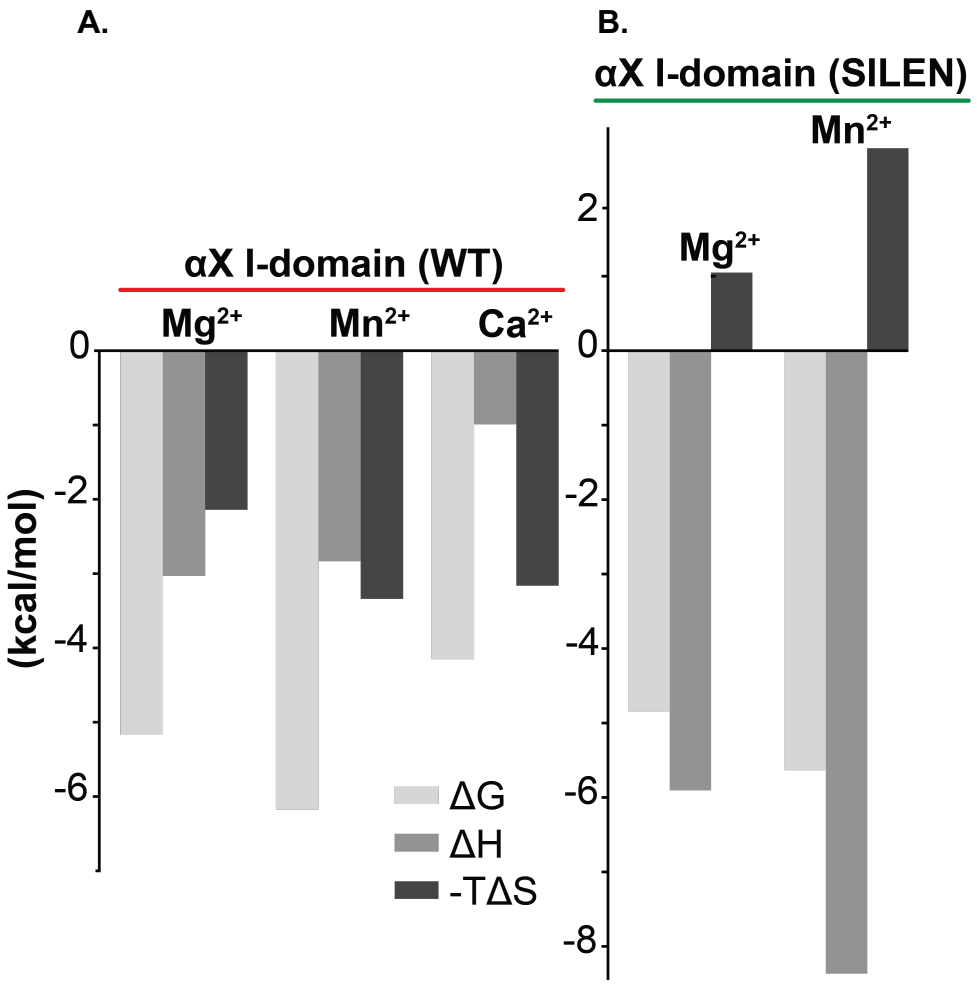

Figure 20: Thermodynamics of divalent cation affinity between the WT and SILEN αX I-domain show significant difference in the change in entropy. The change in the thermodynamic parameters—Gibbs free energy (ΔG), enthalpy (ΔH), entropy (ΔS) upon cation binding to the αX I-domain shows that the affinity of Mn^{2+}>Mg^{2+}>Ca^{2+} for **(A)** the WT αX I-domain and Mn^{2+}>Mg^{2+} for **(B)** the SILEN αX I-domain.

3.2.3 Mg^{2+}-binding induced the secondary structure changes.

To examine if the differences in entropic contribution of the Mg^{2+} interaction with the WT and SILEN αX I-domain could be partially attributed to the change in secondary structures, we investigated the Mg^{2+}-induced conformational changes of the αX I-domain using circular dichroism (CD). The secondary structure content averaged of three scans for the WT and SILEN αX I-domain at different Mg^{2+} concentrations was evaluated by detecting excitation of the backbone amide chromophore (Figures 21A, B).

The experimental far UV CD spectra showed negative bands at 208 nm and 222 nm which is distinctive of well-defined α-helices, and revealed that the protein remained properly folded in solution (Figures 21A, B). The spectra detected α-helices as the dominant secondary structure. Three negative controls for CD data acquisitions used were water, buffer, and air to ensure that non-peptidic chromophores did not show significant CD signals and contribute to the αX I-domain CD spectra (Figure 21C). In the CD spectra acquired, the helical ellipticity of the WT αX I-domain was higher than that of the SILEN αX I-domain, and we predict this difference is potentially due to the αI-α7 helix of the SILEN αX I-domain sampling in multiple flexible states.

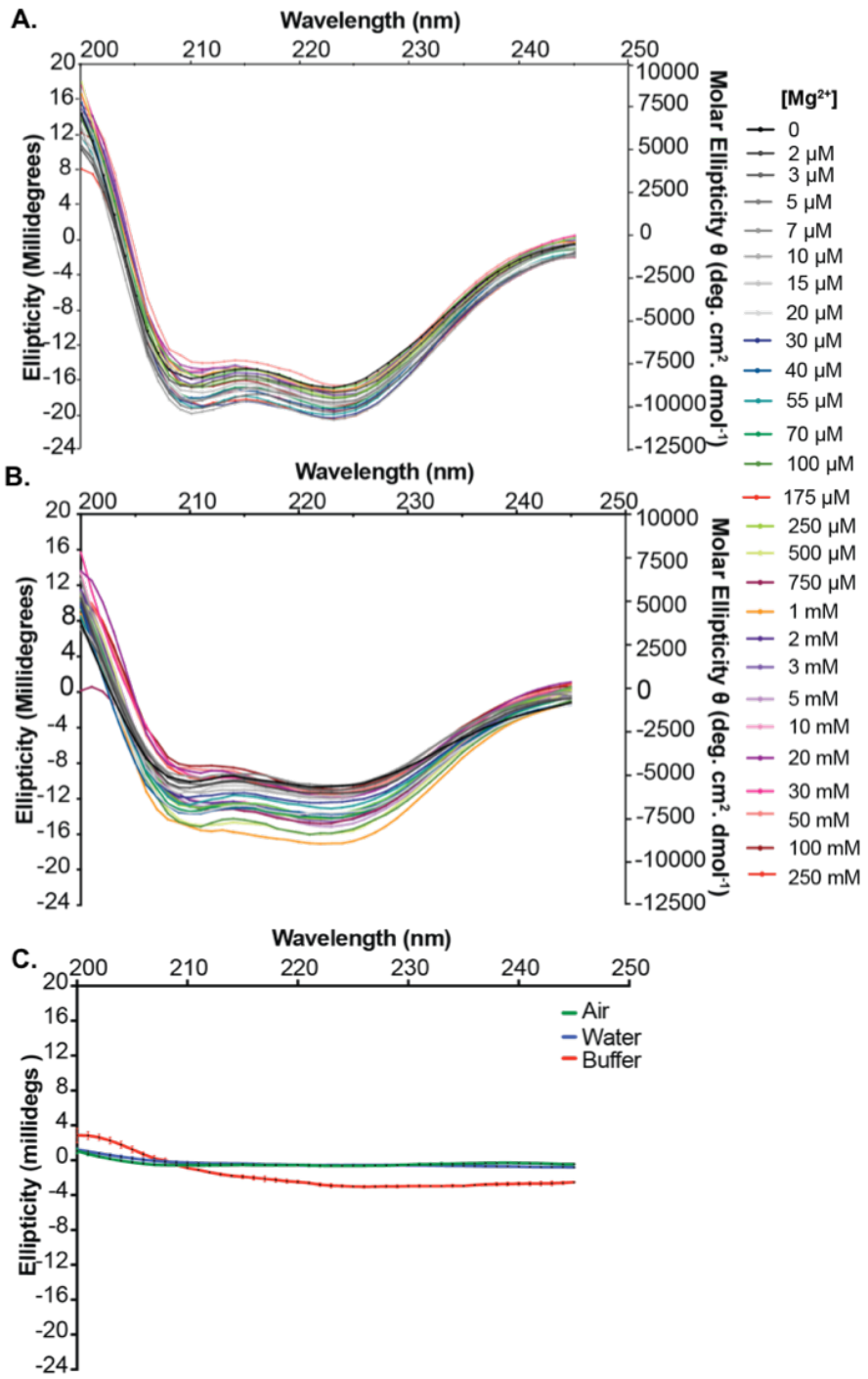

Figure 21: Probing the change in the secondary structure of the αX I-domain by Mg^{2+} titration using circular dichroism. Circular dichroism spectra of the 10 μM of the **(A)** WT αX I-domain and **(B)** SILEN αX I-domain upon Mg^{2+}-binding at the range of 1 μM-250 mM. The WT αX I-domain exhibited higher ellipticity compared to the SILEN αX I-domain. **(C)** The three negative controls for CD signals—water, buffer, and air show that non-peptidic chromophores did not impact the αX I-domain data acquisitions. Each CD spectra represents an average of three scans.

We further quantified the change in the secondary structure content using three independent flexible basis methods, SELCON3, CONTIN-LL, and CDSSTR. These methods implicitly assume the effects of distortions of distance, torsions and end effects using variable weighting of the reference protein sets (116). With an increasing ratio of Mg^{2+} to the WT αX I-domain, the relative helical content was either reduced in two or unchanged in one flexible basis methods, suggesting that the entropy-increase that we observed in isothermal calorimetric titrations, partially if not fully, could be a result of the partial loss in secondary structure content of the ensemble-averaged solution states (Figures 22A-C). In case of the SILEN αX I-domain, the effect of increasing concentration of Mg^{2+} on the ensemble-averaged secondary structure appeared to be biphasic — increasing until 1 mM and then reducing. Our results showed that the secondary structure content of the WT αX I-domain was altered upon Mg^{2+}-binding even though the cation binding site does not comprise secondary structures in its immediate vicinity. Since the pattern of change in the helical content of the WT αX I-domain during Mg^{2+} titration differed than that of the SILEN αX I-domain, it can be inferred that this Mg^{2+} binding event potentially establishes crosstalk with allosteric regions of the αX I-domain, especially the αX I-α7 helix.

Figure 22:The change in percentage of secondary structure content quantified by using the CD pro analysis suite indicates conformational change of the αX I-domain upon Mg^{2+}-binding. The α-helix content is represented by red dots for the WT αX I-domain and green dots for the SILEN αX I-domain at each Mg^{2+} concentration using the analysis programs **(A)** Selcon3, **(B)** CONTIN-LL, and **(C)** CDSSTR algorithms with the SP43 protein database as reference. In all three methods, the helical content of the SILEN αX I-domain is shown to increase until 1 mM Mg^{2+} and gradually reduce afterwards. A gradual decrease in the helical content of the WT αX I-domain is exhibited in the Selcon3 and CONTIN-LL methods.

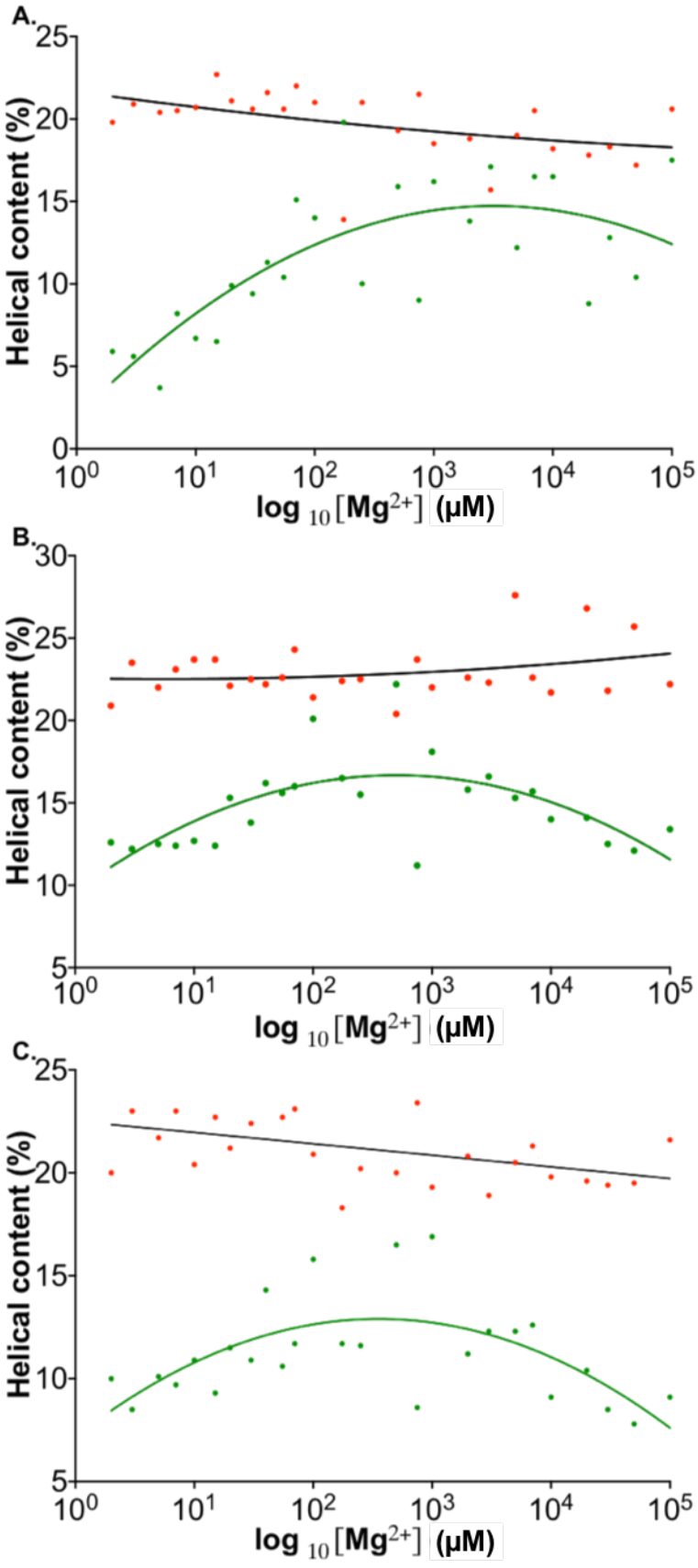
A.
Helical content (%)
25
20
15
10
5
0
10^0 10^1 10^2 10^3 10^4 10^5
log $_{10}$[Mg^{2+}] (μM)
B.
Helical content (%)
30
25
20
15
10
5
10^0 10^1 10^2 10^3 10^4 10^5
log $_{10}$[Mg^{2+}] (μM)
C.
Helical content (%)
25
20
15
10
5
10^0 10^1 10^2 10^3 10^4 10^5
log $_{10}$[Mg^{2+}] (μM)

3.2.4 Mg^{2+}-binding alters the stability of the αX I-domain.

Due to the CD data analysis indicating Mg^{2+}-dependent conformational change in the αX I-domain, we also wanted to determine if its stability was affected by Mg^{2+}-binding. Upon assessing the stability of the WT and SILEN αX I-domain at different temperatures using DSC, we observed the heat change associated with their thermal denaturation at different concentrations of Mg^{2+}. The WT αX I-domain appeared to exhibit single unfolding transition demonstrated by the melting temperature (T_m) at 53 ^oC in the cation-less condition (Figure 23A). However, a second transition at the lower temperature might be present, yet such a conclusion from the DSC unfolding curves is not reliable. Moreover, two distinct transition midpoints were observed for the cation-less SILEN αX I-domain which were indicated by its T_m at 40 ^oC and 53 ^oC (Figure 23B). The WT αX I-domain was thermodynamically more stable than the SILEN αX I-domain which was revealed by the difference between their melting temperatures (ΔT_m) of 13 ^oC and difference in enthalpy change ($\Delta\Delta H_{unfolding}$) of 135.48 kcal/mol (Figure 23 and Table 6).

With increasing Mg^{2+} concentrations, the T_m of the WT αX I-domain noticeably shifted by 10 ^oC increasing from 53 ^oC to 63 ^oC (Figure 23A). The SILEN αX I-domain also exhibited a similar increase in T_m of the first transition peak by 9 ^oC from 40 ^oC to 49 ^oC (Figure 23B). Notably, the second transition midpoint of the SILEN αX I-domain gradually disappeared with increasing Mg^{2+} concentration even though its T_m did not shift. For the αX I-domain, it is likely that the two conformational states/domains could be existing in solution at three different rates of equilibrium: fast, intermediate, and slow exchange. In case of the SILEN αX I-domain, it is tempting to speculate that the slow

exchange rate of equilibrium occur between the two distinct transitions and that the equilibrium is driven towards the first transition state.

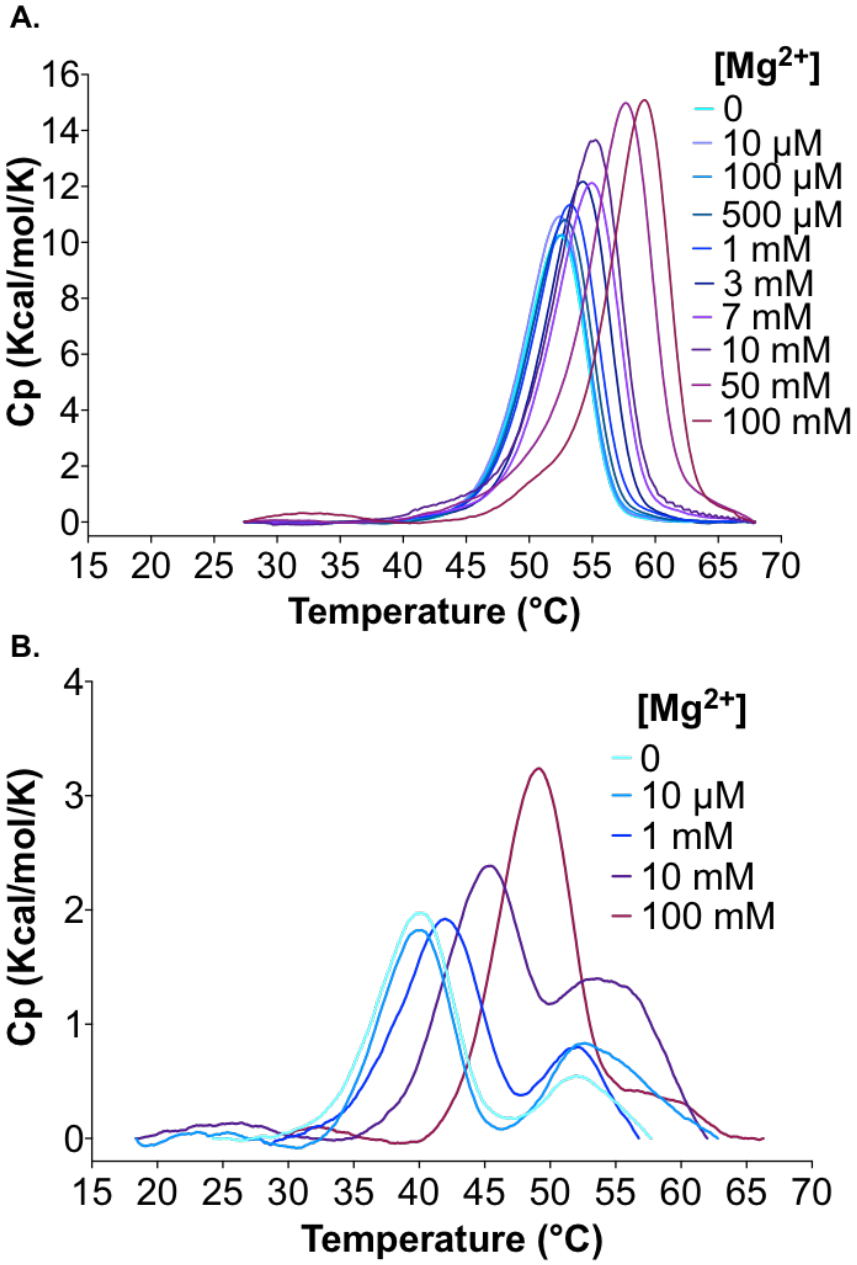

Figure 23: Mg^{2+}-binding increases the stability of the WT and SILEN αX I-domain. The differential scanning calorimeter (DSC) measurements showed that **(A)** the WT αX I-domain exhibited a single transition with the melting temperature increasing from 53 °C to 63 °C and **(B)** the SILEN αX I-domain exhibited two transition midpoints with the melting temperature at first transition midpoints increasing from 40 °C to 53 °C.

For both the WT and SILEN αX I-domain, a gradual increase in the $\Delta_u H°$ was observed upon increase in the Mg^{2+} concentration (Table 6). Taken together, these data showed that the increasing Mg^{2+} concentrations elevated the thermal stability of both conformations, suggesting potential structural differences that are incurred in the αX I-domain upon Mg^{2+}-binding.

Table 6: The values for change in enthalpy (ΔH) of the WT and SILEN αX I-domain upon binding of different concentrations of Mg^{2+} determined by differential scanning calorimeter (DSC)

	$\Delta_u H$ (kcal/mol)	
Mg^{2+} concentration	**αX I-domain (WT)**	**αX I-domain (SILEN)**
0 μM	187.70	52.22
10 μM	190.47	53.81
100 μM	182.55	N/A
500 μM	200.77	N/A
1 mM	216.21	56.60
3 mM	234.83	N/A
7 mM	222.15	N/A
10 mM	315.61	86.50
50 mM	311.25	N/A
100 mM	252.65	70.96

Multiplicity in DSC requires an ample amount of instrument time. Thus, we used another ortholog method to DSC, differential scanning fluorimetry (DSF), which has high multiplicity and can quantitatively assess the thermal unfolding event of proteins in a single experiment with a limited amount of protein. With increase in the Mg^{2+} concentration, the melting temperature of the WT and SILEN αX I-domain elevated from

45.9 °C to 57.4 °C and from 36.0 °C to 43.2 °C, respectively (Figures 24A, B). Implementing the Mg^{2+}-affinity to the αX I-domain obtained by the aforementioned ITC measurements, we plotted the αX I-domain transition midpoints at varying Mg^{2+} concentrations defined as multiples of equilibrium dissociation constant (K_D) values. We observed that the T_m did not change significantly for the WT αX I-domain or was slightly reduced in the case of the SILEN αX I-domain at Mg^{2+} concentrations below 1X K_D. A gradual increase in the T_m was observed as the MIDAS was increasingly occupied by Mg^{2+}, which resulted in approximately 90% occupancy at 10X K_D. However, above 10X K_D, both the WT and SILEN αX I-domain initially demonstrated a steep increase in the T_m, which eventually plateaued after reaching saturation (Figures 24A, B).

To validate that the Hofmeister or lyotropic effect via increasing ionic strength did not contribute to the increase in the T_m of the αX I-domain, we tested the αX I-domain thermal unfolding at increasing concentrations of sodium chloride. In this case, the T_m of the αX I-domain remained consistent which confirmed that the change in the solution ionic strength did not alter the thermal stability of the αX I-domain (Figure 24C). Taken together, our results suggested that the alteration of conformational stability during the thermal unfolding of the αX I-domain resulted from the Mg^{2+}-binding.

When the Mg^{2+}-induced structural alteration was modelled, differential changes in the melting profiles of the Mg^{2+}-binding to the WT and SILEN αX I-domain, respectively, were better represented via bi-phasic transition model. The bi-phasic (red-line) and mono-phasic fit (blue-line) binding profiles for the WT and SILEN αX I-domain were compared using *F*-tests which signified bi-phasic transition with *P*-values of <0.0001 (Figures 24A, B). The two-state or multiple-states transition was especially

apparent for the SILEN αX I-domain. Interestingly, this result aligned well with similar bi-mosaic CD and DSC transition profiles observed for the SILEN αX I-domain.

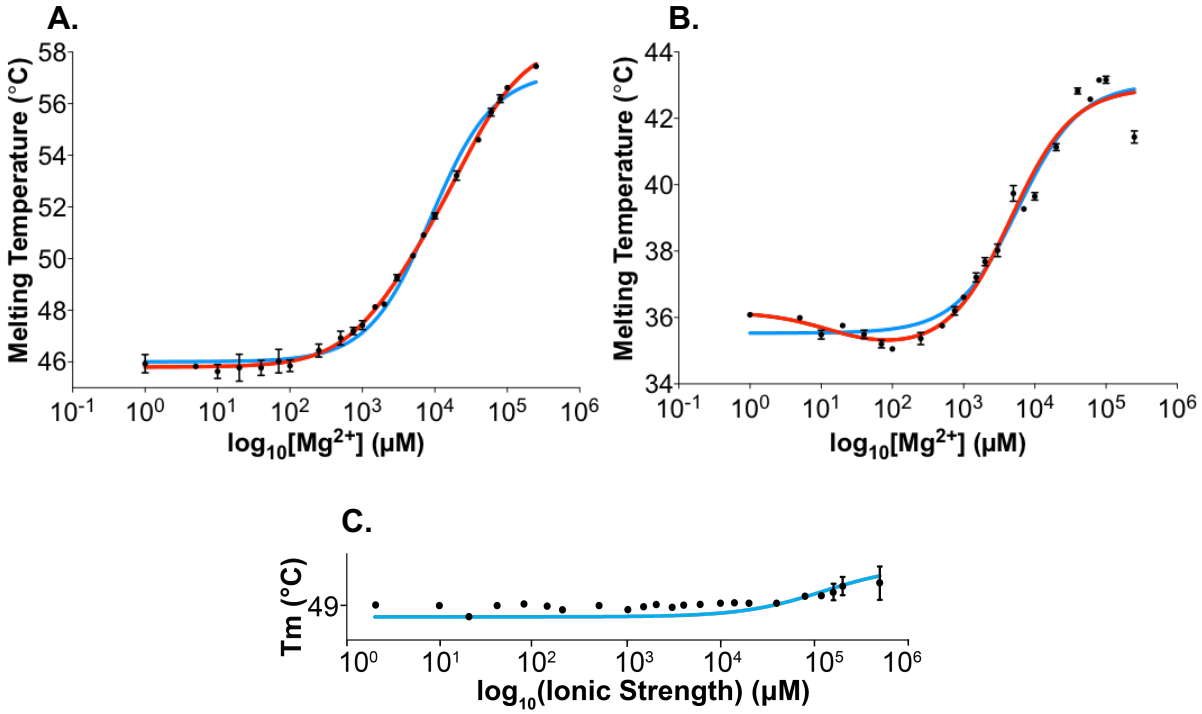

Figure 24: Mg^{2+}-binding increases the stability of the αX I-domain and is associated to the structural alteration of the αX I-domain after MIDAS saturation. Increase in the melting temperature (T_m) of **(A)** the WT αX I-domain from 45.9 °C to 57.4 °C and **(B)** the SILEN αX I-domain from 36.0 °C to 43.2 °C at increasing Mg^{2+} concentrations ranging from 0-250 mM. **(C)** The T_m of the αX I-domain did not change with an increasing concentration of sodium chloride. The bi-phasic and mono-phasic binding profiles are fitted using Prism7, and represented by the red and the blue line, respectively.

We further assessed the Mn^{2+}- and Ca^{2+}-dependent αX I-domain thermal unfolding event using DSF. In this case, buffer for the αX I-domain was consistent with the buffer used for the ITC sample preparations (20 mM Tris 150 mM NaCl, pH 7.5 prepared in chelex-treated water). With an increase in the Mn^{2+} concentration from 0-50 mM, the melting temperature of the WT and SILEN αX I-domain increased from 39.4 °C to 49.7 °C and from 40.5 °C to 50.1 °C, respectively (Figures 25A, B). Next, at

increasing Ca^{2+} concentrations ranging from 0-250 mM, we observed an increase in the T_m of the WT αX I-domain from 40.3 ^oC to 44.7 ^oC and the SILEN αX I-domain from 38.9 ^oC to 42.5 ^oC (Figures 25C, D).

For the Mn^{2+} or Ca^{2+} concentrations below 74 μM and 480 μM, respectively, or 1X K_D concentration, we observed that the T_m did not change drastically for the WT or the SILEN αX I-domain. Similar to the pattern observed for Mg^{2+}-interaction to the αX I-domain in the aforementioned DSF analysis, a gradual increase in the T_m was observed as the MIDAS was increasingly occupied by Mn^{2+} or Ca^{2+}, respectively. This T_m increase was associated with approximately 90% occupancy corresponding to roughly 10X K_D concentration. Mn^{2+} or Ca^{2+} concentration above 10X K_D concentration for both the WT and SILEN αX I-domain initially demonstrated an increase in the T_m with ΔT_m of approximately 8 ^oC and 4 ^oC, respectively, which ultimately plateaued (Figures 25A-D). The Mn^{2+}-interaction with the αX I-domain displayed a better fit for bi-phasic transition (red-line) compared to mono-phasic fit (blue line) with the *P*-values of <0.0001 in the *F*-test (Figures 25A, B). Binding fits and fit comparison were performed using Prism7.

Similarly, Ca^{2+}-interaction with the WT αX I-domain also displayed a bi-phasic transition (Figure 25C). However, a mono-phasic binding profile was observed for the Ca^{2+}-SILEN αX I-domain interaction (Figure 25D). Compared to the ITC titration analysis in which we did not observe binding of Ca^{2+} to the SILEN αX I-domain, the mono-phasic transition was observed in the DSF analysis.

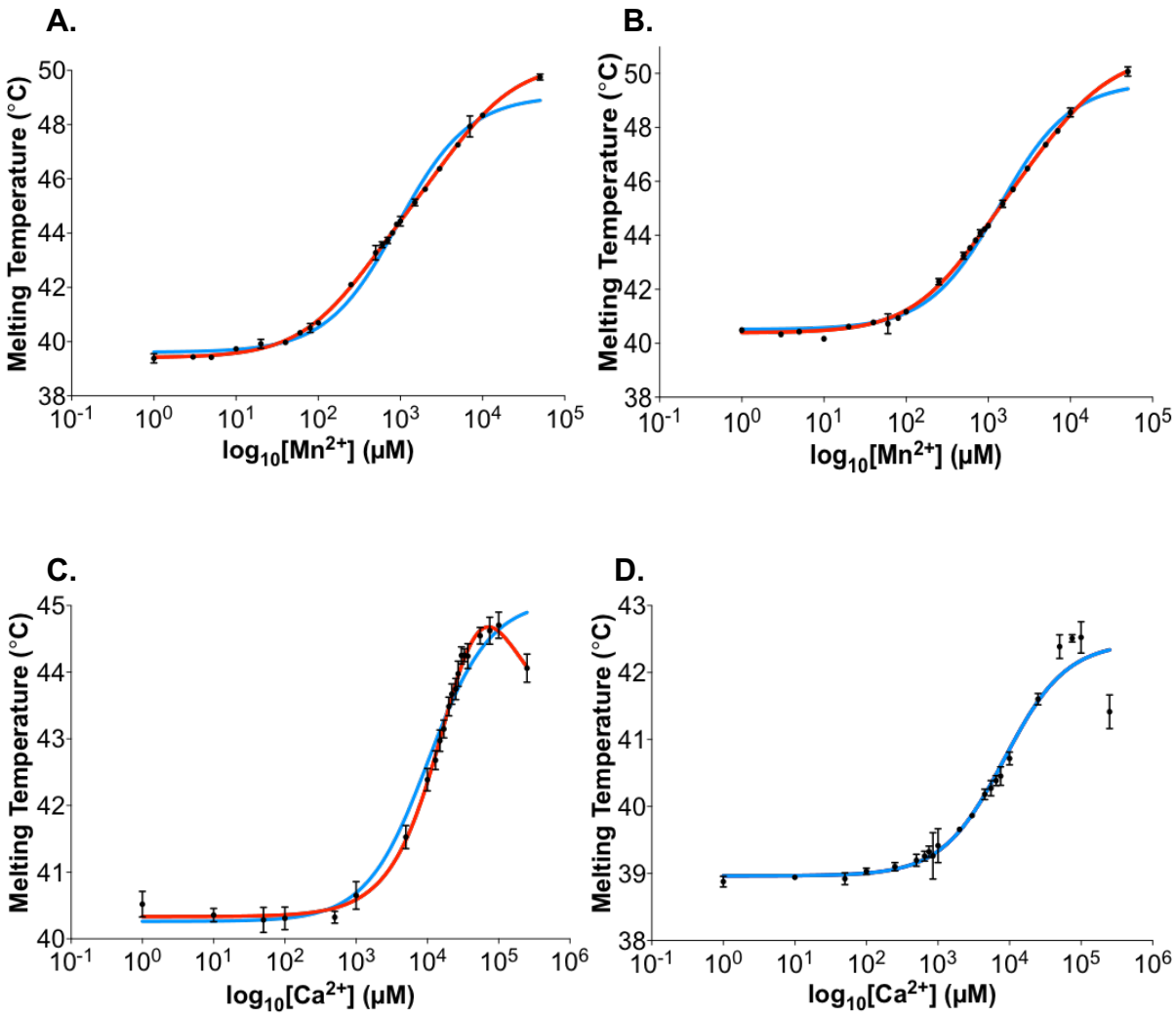

Figure 25: Alteration of conformational stability demonstrated upon MIDAS saturation by Mn^{2+}- and Ca^{2+}- binding, respectively, to the αX I-domain. Increase in the melting temperature (T_m) of **(A)** the WT αX I-domain from 39.4 ºC to 49.7 ºC, **(B)** the SILEN αX I-domain from 40.5 ºC to 50.1 ºC at increasing Mn^{2+} concentrations ranging from 0-50 mM. The T_m increase of **(C)** the WT αX I-domain from 40.3 ºC to 44.7 ºC and **(D)** the SILEN αX I-domain from 38.9 ºC to 42.5 ºC at increasing Ca^{2+} concentrations ranging from 0-250 mM. The red and blue line represent the bi-phasic and mono-phasic binding profiles, respectively which were fitted using Prism7.

Our DSF studies on the thermal unfolding of the αX I-domain in presence of the cations-Mg^{2+}, Mn^{2+}, and Ca^{2+}, respectively, suggested that the conformational stability of the αX I-domain is altered as a result of divalent cation binding.

The T_m values of the cation-less αX I-domain obtained by DSC was found to be higher than that via DSF by 7 ^oC and 4 ^oC for the WT and the SILEN αX I-domain, respectively. These differences could be attributed to the difference in the approaches of T_m measurement between the two methods. DSC provided a measurement of direct assessment of the heat energy uptake upon cation binding to the αX I-domain. However, DSF relies on a fluorescence-based measurement in which the activity of dye-binding is solely dependent on the exposure of hydrophobic residues of the αX I-domain. As temperature increases, hydrophobic residues are exposed upon protein denaturation and bound to dye, which then result in increase in fluorescence. Also, the dye-binding event could, negatively or positively, contribute some energetics to the protein unfolding event as previously reported for 8-anilinonaphthalene-1-sulfonic acid (ANS) or SYPRO orange dyes (135), which may alter the T_m. In addition, the difference in the scan rates between the two techniques was a significant variable which could be accounted for the discrepancy in the T_m values. Nonetheless, in both DSC and DSF, the ΔT_m induced upon the αX I-domain unfolding during Mg^{2+}-titration is similar and consistent (~10 ^oC) for both experimental setups.

To monitor the time required for equilibrium of SYPRO orange binding to the αX I-domain in each step and to ensure that the binding equilibrium is reached, we conducted a stopped-flow analysis. The resulting fluorescence spectra demonstrated a binding saturation within 2 seconds at all the temperatures ranging from 30 ^oC to 60 ^oC (Figure 26A).

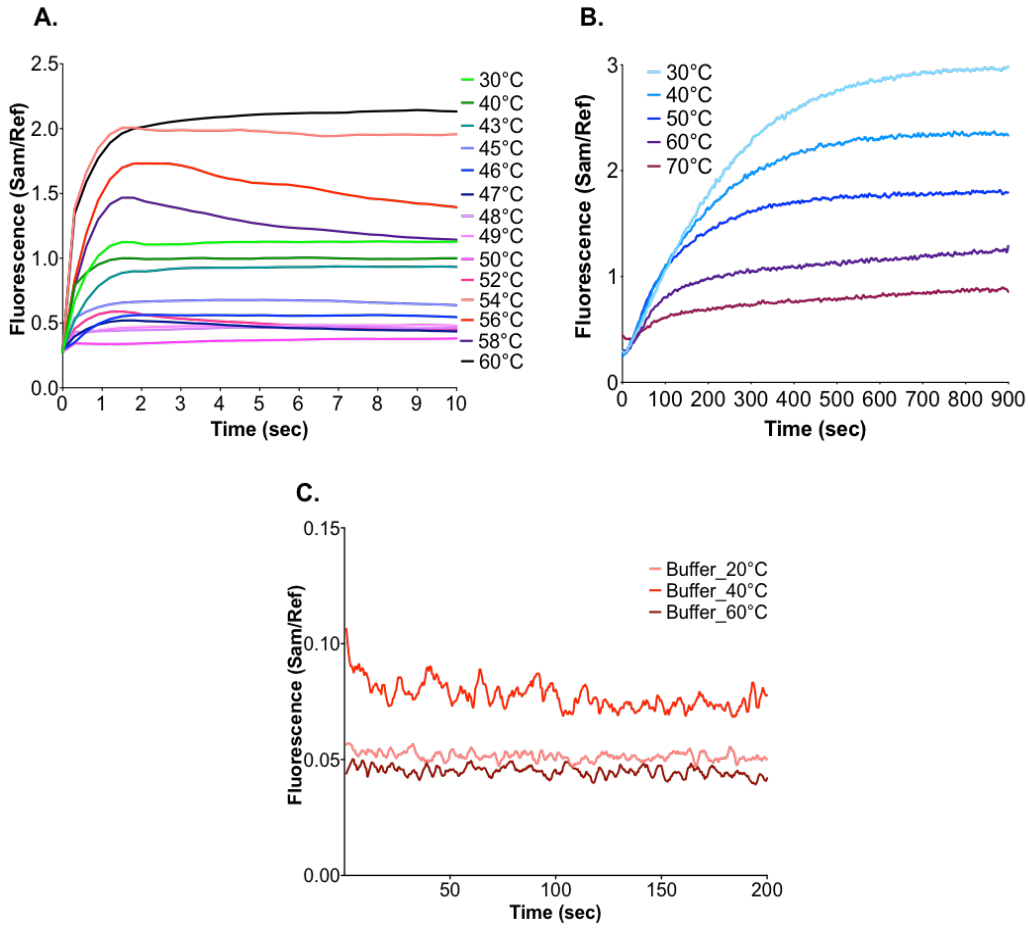

Figure 26: The SYPRO orange dye binding equilibrium was monitored by the measurement of fluorescence intensity at different temperatures using stopped-flow analysis. SYPRO orange binding to **(A)** the WT αX I-domain was expeditious compared to **(B)** lysozyme which reached saturation at approximately 400 seconds. **(C)** Buffer (20 mM Hepes, 150 mM NaCl, pH 7.5) did not demonstrate any fluorescence increase. The excitation and emission wavelength selected for measurement were 505 nm and 575 nm, respectively.

For comparison, we also measured the binding of SYPRO orange to lysozyme which demonstrated a relatively slower binding saturation at approximately 400 seconds within temperatures ranging from 30 °C to 70 °C (Figure 26B). As a negative control for fluorescence detection, addition of SYPRO orange to the buffer in which the proteins were solubilized in did not show significant change in fluorescence (Figure 26C). Our results ensured that binding of SYPRO orange to the αX I-domain occurred in less than

3 seconds, and we used a 1-minute delay in each step of DSF. Thus, the DSF measurements of the αX I-domain T_m used in our experimental setup were reliable.

3.2.5 pH-dependent αX I-domain unfolding in the absence and presence of Mg^{2+}.

As illustrated in Section 1.4.4.1, the octahedral Mg^{2+}-coordination at the αX I-domain MIDAS is mediated by polar contacts with two important aspartate residues, Asp 138 and Asp 240. The Asp 138 belongs to the conserved DXSXS sequence and involves in an invariant water-mediated Mg^{2+}-coordination. In the closed state αX I-domain, the Asp 240 directly interacts with Mg^{2+}. These aspartate-mediated contacts are buried in the extremely hydrophobic microenvironment at the MIDAS motif (78, 79). The change in energetics of the ionization of the titratable acidic residues results from an adaptation by the hydrophobic core to ensure that the local environment is maintained at a neutral pH (136). Therefore, we wanted to assess if the variation of the protonation state of the cation-less and cation-occupied αX I-domain at pH range 3—11 could be observed in respect to the αX I-domain stability.

We wanted to apply DSF to examine how the melting temperature and thermodynamics of the WT and SILEN αX I-domain unfolding upon Mg^{2+}-binding, respectively, were affected by the change in pH values. Therefore, by implementing the equations illustrated in Section 2.5.2, we first calculated the $\Delta_u G$ values and plotted them against the temperature values in the range of 50-90% folded αX I-domain at each experimental condition. The $\Delta_u G^o$, $\Delta_u H^o$, and $\Delta_u S^o$ at 298 K was then determined, as described in detail in Section 2.5.2 by solving for the linear equation of best fit from the plot of $\Delta_u G$ versus temperature at each condition.

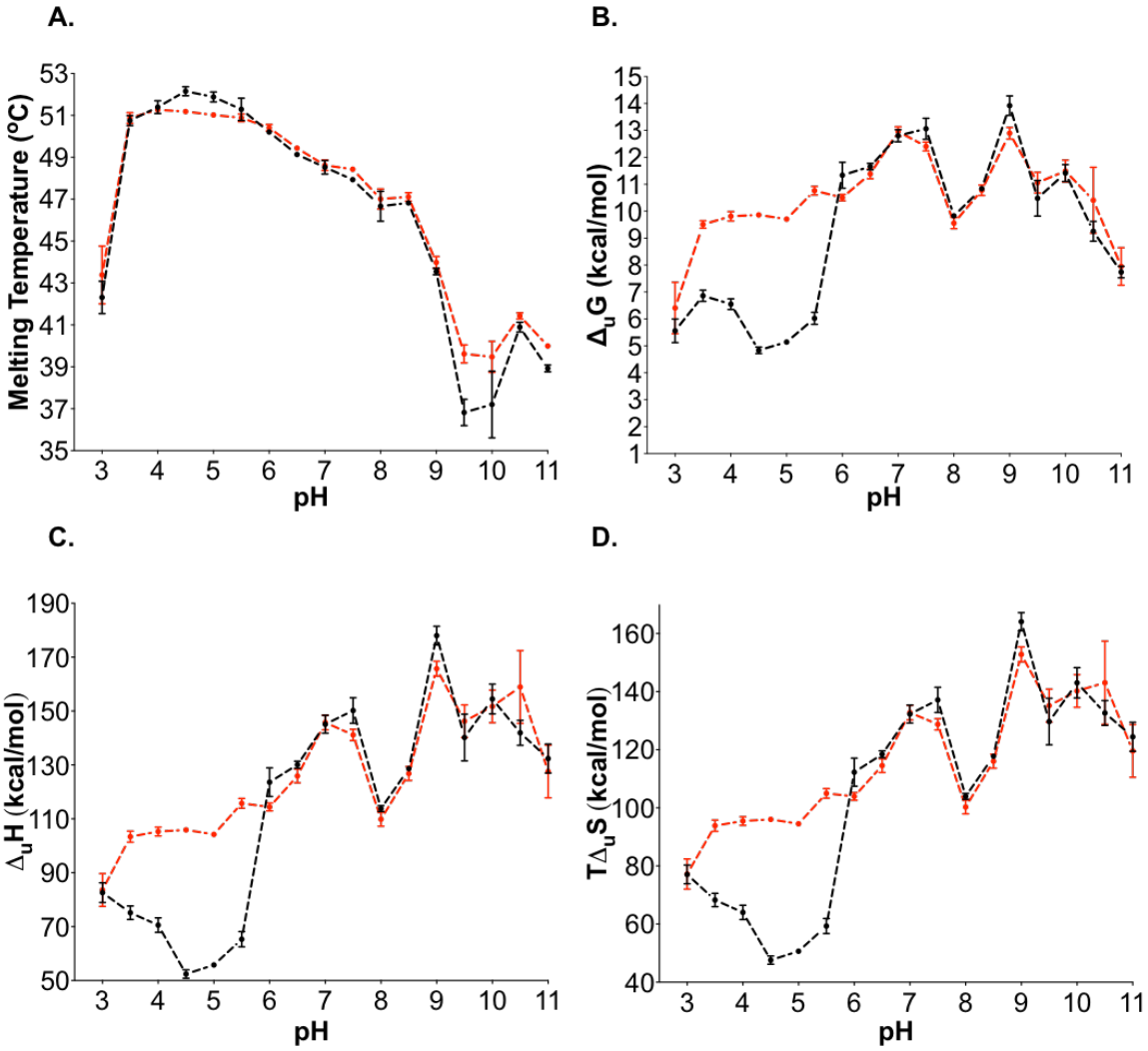

Figure 27: DSF analysis showing difference in the melting temperatures and thermodynamics of Mg^{2+}-bound and Mg^{2+}-less WT αX I-domain unfolding. (A) The T_m of the WT αX I-domain in Mg^{2+}-bound or Mg^{2+}-less conditions did not show any significant difference throughout the pH range of 3—11. **(B-D)** Differences in the thermodynamics parameters between Mg^{2+}-bound or Mg^{2+}-less WT αX I-domain were specifically observed at the pH range of 3—6. Black line and red line represent Mg^{2+}-less and 1 mM Mg^{2+} conditions of the WT αX I-domain unfolding, respectively.

The thermal denaturation of the WT αX I-domain in a pH range demonstrated a similar T_m trend for both Mg^{2+}-less and 1 mM Mg^{2+} conditions (Figure 27A). However, in these two conditions, a differing trend appeared when comparing their unfolding thermodynamics parameters. The Gibbs free energy of unfolding ($\Delta_u G°$) of the WT αX I-

domain containing 1 mM Mg^{2+} swiftly reached 10.5 kcal/mol at pH of 3.5 (Figure 27B). In contrast, for the cation-less WT αX I-domain, the recovery of $\Delta_u G^o$ above 10 kcal/mol occurred only after pH of 6. The $-T\Delta_u S^o$ and $\Delta_u H^o$ also followed a similar trend (Figures 27C, D).

Despite exhibiting similar T_m for αX I-domain unfolding at both cation-less and 1 mM Mg^{2+} conditions at each pH (Figure 27A), their $\Delta_u G^o$ differed at the pH range of 3 to 6. Typically, the pK_a of aspartate residue is at the value of 3.65. Therefore, at pH values higher than 3.65, the aspartate residue is further deprotonated. In our unfolding studies on the WT αX I-domain at 1 mM Mg^{2+} condition, as the pH moves above 3, the $\Delta_u G^o$ significantly increased to 10 kcal/mol. In case of cation-less condition, despite the absence of Mg^{2+}, the stability of the WT αX I-domain reach to similar $\Delta_u G^o$ of 10 kcal/mol after pH reached to 6. This pH-dependent unfolding experiment suggested that the protonation/deprotonation switch of MIDAS aspartates could be important in stabilizing the αX I-domain in solution. It is tempting to speculate that Mg^{2+} might establish some long-range molecular interactions, which probably serve in stabilizing the hydrophobic core of the WT αX I-domain and could not be established below this pKa of MIDAS aspartate or in the absence of Mg^{2+}. Based on these results, I predicted that the MIDAS-aspartates could potentially achieve ionization states different than the typical pK_a.

For further investigation, we determined if the residues, Asp 138 and Asp 240 demonstrated any change in the pK_a between the WT (closed state) and the SILEN (open state) αX I-domain using constant-pH MD simulation (performed by Zahra Mazhar, Briggs Lab). The pK_a of Asp 138 remarkably increased by more than 3 pH units

from 2.2 to 5.4 when moving from the closed to open state in Mg^{2+}-bound condition. In contrast, the pK_a of Asp 240 exhibited an opposing trend with reduction by 1.33 pH units from 3.9 to 2.6 (Table 7). These observations suggested that the change in the protonation states of Asp 138 and Asp 240 play a central role in regulating the αX I-domain conformational change between the closed and the open state.

Table 7: The pK_a values for the aspartate residues at MIDAS determined by using constant-pH MD simulation

	Mg^{2+}-bound closed state αX I-domain (PDB: 5ES4)	**Mg^{2+}-less closed state αX I-domain** (PDB: 1N3Y)	**Mg^{2+}-bound open state αX I-domain** (PDB: 4NEH)
Asp 138	2.2	3.8	5.4
Asp 240	3.9	5.9	2.6

In comparison to the pK_a of Mg^{2+}-bound closed state (2.2 for Asp 138 and 3.9 for Asp 240), the Mg^{2+}-less closed state showed an intermediate pK_a value of 3.8 for Asp 138 and higher pK_a value of 5.9 for Asp 240 (Table 7). The decrease in the pK_a values of both aspartates in the Mg^{2+}-bound state (2.2 for Asp 138 and 3.9 for Asp 240) compared to the Mg^{2+}-free state (3.8 for Asp 138 and 5.9 for Asp 240) indicated that these aspartates are both deprotonated and endow stronger ionic interaction with the bound Mg^{2+}.

This result validated the increase in the $\Delta_u G$ to 10.5 kcal/mol at pH of 3.5 upon Mg^{2+} addition, thereby increasing the stability of the WT αX I-domain (Figure 28B). Therefore, these uncharacteristically regulated changes in the pK_a values of Asp 138 and Asp 240 support the aforementioned differences in the αX I-domain unfolding observed in the absence and presence of Mg^{2+} in the pH range of 3 to 6.

In case of the SILEN αX I-domain, we observed an increase in T_m by approximately 4 ^oC in the Mg^{2+}-bound condition compared to the Mg^{2+}-less condition in the pH range of 3 to 5.5. A decrease in the T_m by approximately 2 ^oC was observed in the pH range of 7 to 8 (Figure 28A). Unlike the WT αX I-domain, Mg^{2+}-binding elicited alteration in the stability of the SILEN αX I-domain as a function of pH which was apparent by the resulting change in the T_m. The Δ_uG^o of the SILEN αX I-domain containing 1 mM Mg^{2+} gradually reached 10 kcal/mol at pH of 5.5. In contrast, for the Mg^{2+}-less SILEN αX I-domain at pH range of 3.5 to 5.5, high Δ_uG of 10 kcal/mol was not obtained; instead it was maintained in the range of 5-6 kcal/mol (Figure 28B). A similar trend was observed for the $-T\Delta_uS^o$ and Δ_uH^o (Figures 28C, D).

Interestingly, the difference in the unfolding nature of the WT and SILEN αX I-domain in Mg^{2+}-less and 1 mM Mg^{2+} condition was observed especially at pH range of 3 to 6. The increase in the stability due to elevated T_m and Δ_uG^o of the SILEN αX I-domain upon Mg^{2+}-binding at pH range of 3 to 6 implied the importance of the Mg^{2+} interaction.

At pH value higher than 3 and below 6, the Asp 138 and Asp 240 along with other intermolecular interactions could be functioning together in coordinating the Mg^{2+} binding and increasing the stability of the SILEN αX I-domain. The αX I-domain structure in the open state (represented by SILEN αX I-domain in our studies) crystallized at pH 7 showed that the Asp 240 loses its interaction with Mg^{2+} and Asp 138 maintains the water-mediated hydrogen bonding to the Mg^{2+}. We predict that at higher pH, the loss of binding of Asp 240 to Mg^{2+} could result in a decrease in the stability of the SILEN αX I-domain.

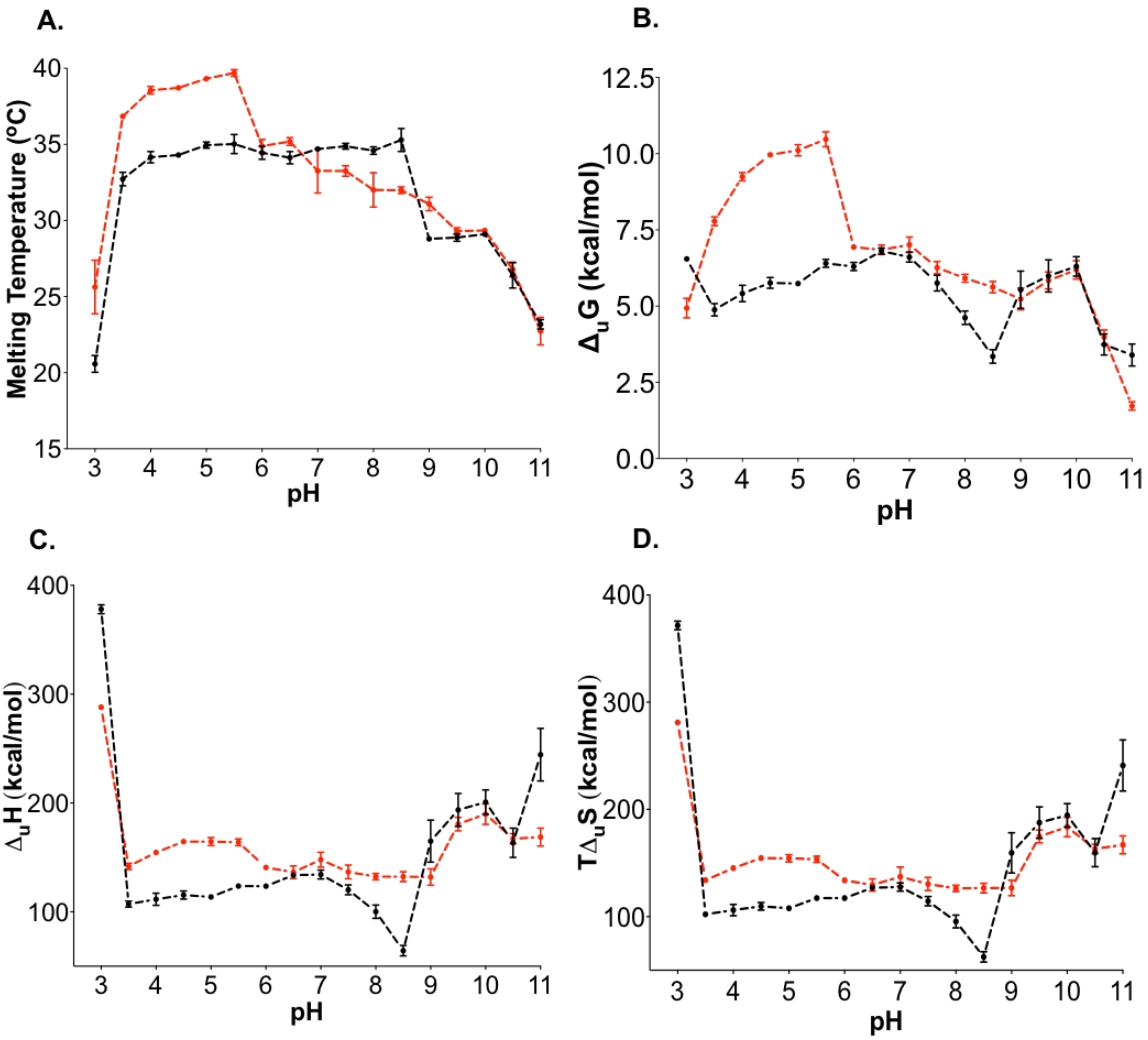

Figure 28: DSF analysis showing difference in the melting temperatures and thermodynamics of Mg^{2+}-bound and Mg^{2+}-less SILEN αX I-domain unfolding. **(A)** The T_m of the SILEN αX I-domain in Mg^{2+}-bound or Mg^{2+}-less conditions did not show any significant difference throughout the pH range of 3—11. **(B-D)** Differences in the thermodynamics parameters between Mg^{2+}-bound or Mg^{2+}-less SILEN αX I-domain were observed at the pH range of 3—6. Black line and red line represent Mg^{2+}-less and 1 mM Mg^{2+} conditions of the SILEN αX I-domain unfolding, respectively.

3.2.6. Effects of increasing concentration of Mg^{2+} on the αX I-domain shape.

Our assessment on change in the melting temperature and thermodynamics of the αX I-domain unfolding upon Mg^{2+}-binding from the DSC and ITC studies revealed that Mg^{2+}-binding elicited an increase in the αX I-domain's stability. The increase in the αX I-domain stability was associated with the change in its secondary structure as revealed by our CD spectral analysis.

For a more direct characterization of the conformational changes induced by Mg^{2+} in the αX I-domain, we collected small and wide-angle X-ray scattering (SWAXS) data of the WT αX I-domain at different Mg^{2+} concentrations. The increasing slope observed in the intensity profiles of the αX I-domain scattering data for solutions with increasing levels of free Mg^{2+} in the range of 0—100 mM was indicative of increment in the size of the αX I-domain (Figures 29A, B). SWAXS datasets of the αX I-domain revealed characteristic bell-shaped pairwise distance distribution curves p(r) of a compact globular scattering biomolecule in solution (Figure 29C).

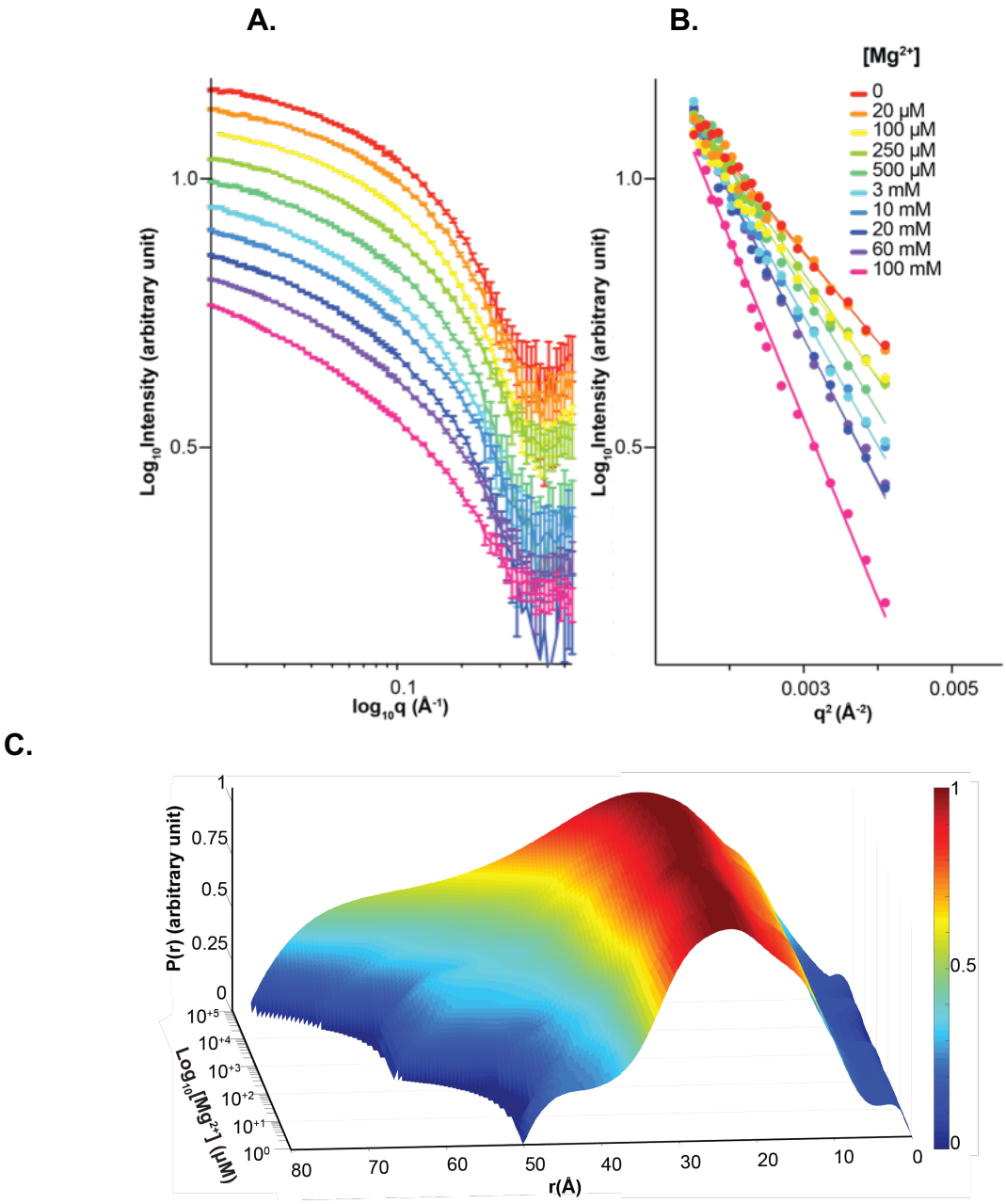

Figure 29: The WT αX I-domain shape-shifting observed with increasing concentrations of Mg^{2+} which progresses the WT αX I-domain towards an open and extended conformational state. SAXS data acquisition reveals increase in the WT αX I-domain size in solution with increase in Mg^{2+} concentrations as depicted by **(A)** Change in the scattering intensity of the WT αX I-domain observed at the Guinier regions with **(B)** corresponding increase in the slope of the Guinier plot with increasing levels of Mg^{2+} in the range of 0—100 mM. **(C)** 3-D plot representing the pairwise distance distribution curves (p(r)) of the scattering vectors versus particle radius r(Å) against different concentrations of Mg^{2+} for the WT αX I-domain shows gradual change in the effective-radius (D_{max}) and radius of gyration (R_g) of the WT αX I-domain in response to Mg^{2+}-addition.

The scaling the scattering profiles using the q_{min}—q_{max} range for investigating the density fluctuations in the αX I-domain sample was a more accurate estimation for analyzing its conformational changes (131). With an increase in the Mg^{2+} concentration in the αX I-domain sample, we observed a decreasing q-range in the linear Guinier regions of the αX I-domain scattering profile. This observation provided an additional evidence for the enlargement of the αX I-domain upon Mg^{2+}-titration (Table 8).

Table 8: Parameters derived from the SAXS data acquisition of the WT αX I-domain at different Mg^{2+} concentrations- the effective-radius (D_{max}), radius of gyration (R_g) and q-range

[Mg^{2+}]	q-range (1/Å)	R_g (Å)	Dmax (Å)
0 µM	0.034 — 0.880	18.33	50.0
20 µM	0.026 — 0.990	18.49	51.0
100 µM	0.039 — 0.990	20.11	62.1
250 µM	0.022 — 0.990	21.72	63.0
500 µM	0.027 — 0.990	22.52	63.0
3 mM	0.023 — 0.990	23.17	63.0
10 mM	0.029 — 0.990	22.74	63.0
20 mM	0.024 — 0.990	25.32	70.0
60 mM	0.019 — 0.990	27.32	77.0
100 mM	0.015 — 0.255	29.55	78.0

Indirect Fourier transformation of intensities of each scattering dataset was with q-ranges between 0.015—0.990 Å (Table 8). These intensities were implemented to estimate the pairwise distance distribution curves (p(r)) of the scattering vectors (Figure 29C). A 3-dimensional plot of the p(r) versus particle radius r(Å) against different concentrations of Mg^{2+} for the WT αX I-domain revealed that the αX I-domain altered its effective-radius (D_{max}) and radius of gyration (R_g) in a step-wise response to Mg^{2+}-

addition. The D_{max} and R_g extended from 50 Å to 78 Å and 18.2 Å to 29.5 Å, respectively (Table 8). It appeared that two conformations of the WT αX I-domain within the time-averaged ensembles exist in solution. Between the two conformations, the first conformational state was depicted to exist in the low micromolar Mg^{2+} concentrations (0 to ~100/250 μM) and exhibited a more compact conformation. The second conformational state exists at mid-to-high millimolar Mg^{2+} range (10 mM—100 mM) which showed a more open and extended conformational state.

In the range where the first distinctive αX I-domain conformational population was observed, MIDAS would not be fully occupied. After Mg^{2+} concentration reached to a half MIDAS occupancy (~50%, which is above 1X K_D of Mg^{2+}-affinity corresponding to 154 μM Mg^{2+} as shown by ITC), a plateau region at Mg^{2+} concentrations in the range of 250 μM—10 mM was observed at which the D_{max} remained steady at 63 Å. Further increment (>98% MIDAS occupancy; corresponding to 10 mM Mg^{2+}) in the Mg^{2+} concentrations to 100 mM generated more extended conformations at which its D_{max} increased to 78 Å and the R_g increased to 29.55 Å.

The dimensionless Kratky plot of $(s.R_g^2)$ I(s) / I(0) as a function of $(s.R_g)$ which is directly calculated from the scattering curve reveals the degree of compactness of the WT αX I-domain at different Mg^{2+} concentrations. The peak roughly shaped like a parabola is the typical representation of a globular protein. We observed that the WT αX I-domain was more compact at Mg^{2+} concentrations ranging from 0-100 μM. The compactness gradually decreased for the αX I-domain and the plot appearance remained similar from 250 μM-10 mM Mg^{2+} concentrations. At higher Mg^{2+} concentrations ranging from 10 mM-100 mM, a broader maximum in the Kratky plots

was displayed which demonstrated that the αX I-domain was less compact (Figure 30). The qualitative assessment of the Kratky plot confirmed that the compactness of the WT αX I-domain decreased upon Mg^{2+}-addition indicating a shift to a more open and extended αX I-domain conformation.

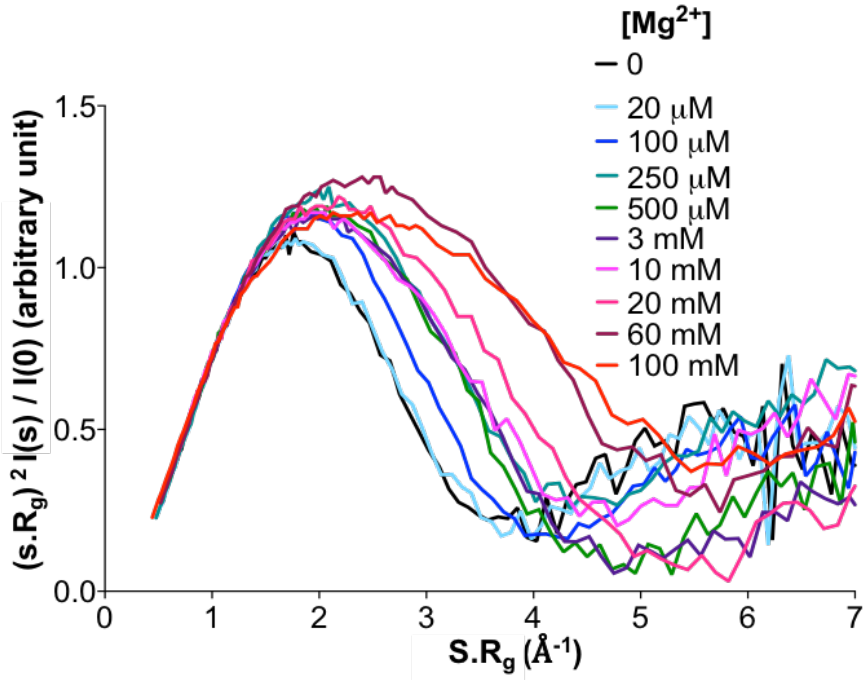

Figure 30: The compactness of the WT αX I-domain decreases with increasing Mg^{2+} concentrations as depicted by SAXS data acquisition. The broadening of the dimensionless Kratky plots indicate decrease in the compactness of the WT αX I-domain with increasing Mg^{2+} concentrations. $S.R_g$ provides information about the shape of the protein.

The I(0)/αX I-domain concentration(c) value, as a parameter independent of the sample concentration, allows reliable determination of the particle size and evaluation of particle aggregates during data analysis (Table 9). The I(0) was calculated using the *y* intercept of the linear regression in the Guinier approximation. The comparable trend observed with the I(0)/c values and qualitative analysis of the dimensionless Kratky plot of the WT αX I-domain upon Mg^{2+}-addition verified that the change in the αX I-domain size observed was indeed due to changes in macromolecular dimensions of the

scattering and not because of intermolecular aggregation events (Figure 30 and Table 9).

Table 9: Experimental conditions and acquired parameters of the WT αX I-domain at different Mg^{2+} concentrations from SAXS analysis- Forward scattering intensity (I(0)), Forward scattering intensity / sample concentration of WT αX I-domain (I(0)/c)

[Mg^{2+}]	[WT αX I-domain] (mg/mL)	I(0) (A.U)	I(0)/c (A.U/ mg)
0 μM	1.92	5.93	3.09
20 μM	2	5.97	2.98
100 μM	2.02	8.44	4.18
250 μM	1.65	8.07	4.89
500 μM	1.45	5.87	4.04
3 mM	1.51	6.45	4.27
10 mM	1.3	5.87	4.51
20 mM	2.07	7.54	3.64
60 mM	1.76	9.96	5.66
100 mM	1.92	13.51	7.04

We were also able to confirm the monodispersity of the WT αX I-domain by acquiring its SEC-SAXS data at Mg^{2+} concentrations in the range of 0-3 mM (Figure 31). Aside from the fact that R_g and D_{max} enlargement followed the same trend as shown in Table 8, the retention volumes of the αX I-domain at different Mg^{2+} concentrations showed a biphasic transition. The center of elution peak of the WT αX I-domain shifted to right gradually from Mg^{2+}-less condition to 100 μM Mg^{2+} condition, after which we observed a leftward shift from 500 μM to 3 mM Mg^{2+}concentrations. We observed a variation in the protein's retention volume at Mg^{2+} concentrations at the range of 0-100 μM (Figure 31-inset). At Mg^{2+} concentrations of 500 μM and 3 mM, the retention volume

remained consistent (Figure 31). These observations supported the aforementioned results obtained by SAXS data acquisition on the αX I-domain as a function of Mg^{2+}-binding.

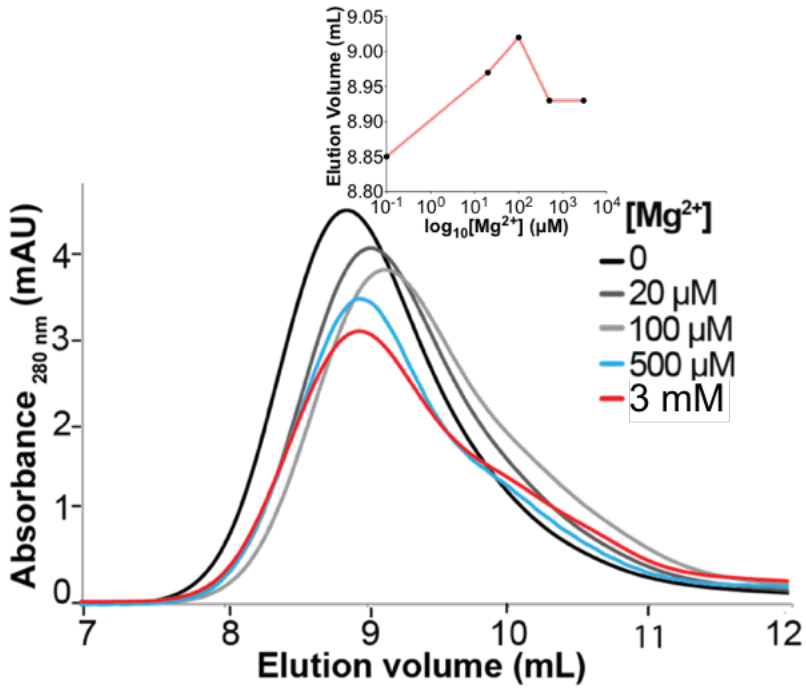

Figure 31: Hydrodynamic radius (R_h) change of the WT αX I-domain at different Mg^{2+} concentrations as probed by SEC. The change in the retention volume of the αX I-domain at Mg^{2+}concentrations indicate change in the R_h of the WT αX I-domain as a function of Mg^{2+} binding.

3.2.7. Roles of Mg^{2+} in the ligand affinity of the αX I-domain.

Even though studies have reported the importance of conformational changes within the αX I-domain in regulating ligand binding (56, 103), the alteration in the αX I-domain ligand-binding affinity as a function of change in its MIDAS occupancy by a divalent cation has not been elucidated. Therefore, we wanted to assess the ligand affinity of any αX I-domain transition states and examine if these states could depict a progressive affinity maturation of the αX I-domain by using surface plasmon resonance (SPR).

To ensure that the ligands, iC3b and fibrinogen, used for immobilization to the SPR sensor chips were non-fragmented, we verified their sizes in the non-reducing and reducing conditions using SDS-PAGE. In the non-reducing conditions, a single band for 181 kDa iC3b and 340 kDa fibrinogen was observed, respectively. In the reducing condition, three iC3b fragments at 75 kDa, 63 kDa, and 43 kDa, as well as fibrinogen fragments at 63.4 kDa, 56 kDa, and 47 kDa, were observed (Figures 32A, B).

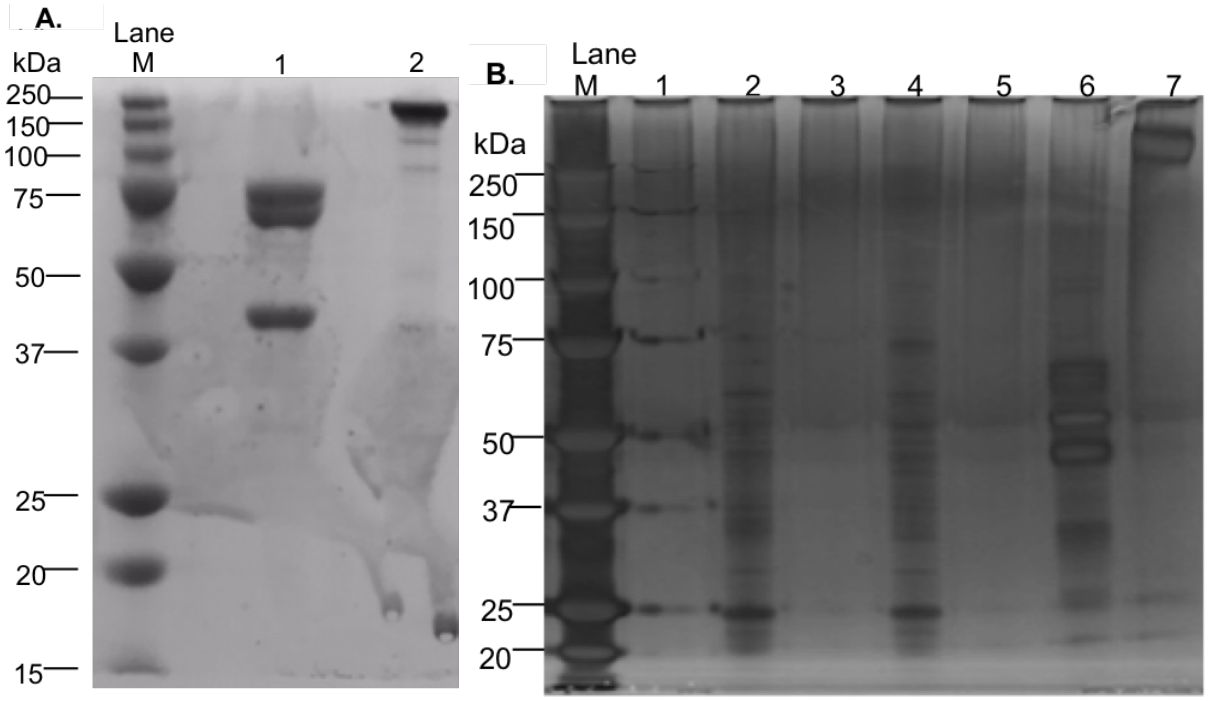

Figure 32: The αX I-domain ligands, iC3b and fibrinogen, used for the SPR binding assays confirmed to be non-fragmented by SDS-PAGE. (A) The 181 kDa band of iC3b was shown in the non-reducing condition (Lane 2) and the three bands were revealed for the iC3b fragments in the reducing condition (Lane 1). **(B)** Fibrinogen in non-reducing condition corresponded to its molecular weight of 340 kDa (Lane 7) and its fragment domains were shown by three bands in the reducing condition (Lane 6).

To test if the observed Mg^{2+}-induced structural changes in solution could impose a regulation onto the ligand affinity, we determined the affinity constants for the αX I-domain binding to fibrinogen and iC3b, respectively, at varying Mg^{2+} concentrations using BIAevaluation software for the SPR assays.

Interestingly, we observed a distinct increment in affinity of the WT αX I-domain to fibrinogen as Mg^{2+} concentration increased, whereas the SILEN αX I-domain did not demonstrate steady affinity. However, the SILEN αX I-domain showed ~10-fold higher affinity to fibrinogen than the WT αX I-domain at Mg^{2+} concentration of 100 μM to 5 mM (Table 10). In the case of the αX I-domain binding to iC3b, the WT and SILEN αX I-domain showed a 2-fold difference at Mg^{2+} concentration of 500 μM and 5 mM (Table 11).

Table 10: Equilibrium association constants of αX I-domains-fibrinogen binding determined from SPR measurements using BIAevaluation software

	Equilibrium association constant (K_A) (M^{-1})	
[Mg^{2+}]	**αX I-domain (WT)**	**αX I-domain (SILEN)**
100 μM	2.41×10^4	20.2×10^4
500 μM	2.67×10^4	37.2×10^4
5 mM	7.70×10^4	51.1×10^4
10 mM	14.9×10^4	25.2×10^4

Table 11: Equilibrium association constants of αX I-domains-iC3b binding determined from SPR measurements using BIAevaluation software

	Equilibrium association constant (K_A) (M^{-1})	
[Mg^{2+}]	**αX I-domain (WT)**	**αX I-domain (SILEN)**
100 μM	7.20×10^4	6.86×10^4
500 μM	6.17×10^4	12.5×10^4
5 mM	5.61×10^4	10.5×10^4
10 mM	8.43×10^4	8.76×10^4

Our analysis of the αX I-domain binding to fibrinogen and iC3b, respectively, deduced two significant findings. First, these results suggested a role of Mg^{2+} in enhancing the affinity of the WT αX I-domain to its ligands. Secondly, our results showed that the SILEN αX I-domain demonstrated a higher ligand affinity to its ligands than the WT αX I-domain.

However, these affinity constants determined by using the 1:1 binding model did not consider the structural heterogeneity of protein-ligand interaction into the affinity analysis; yet we clearly observed Mg^{2+}-dependent structural heterogeneity of the αX I-domain in our CD and SWAXS measurements. It is important to note that the typical SPR data for the αM I-domain, the closest sister-homolog of the αX I-domain with >60% identity, also displayed nonconformity with simple binding models (107).

Therefore, for a more accurate and reliable analysis of the αX I-domain-ligand interaction studies, we implemented the EVILFIT algorithm, which extended the simple one-site model to that of an entire distribution of heterogeneous binding interactions. The SPR binding-traces of the αX I-domain-ligand interactions were analyzed using the distribution model that accounted for heterogeneous interactions such as structural interconversion or immobilized ligand heterogeneity on the SPR surface (Figure 33) (118).

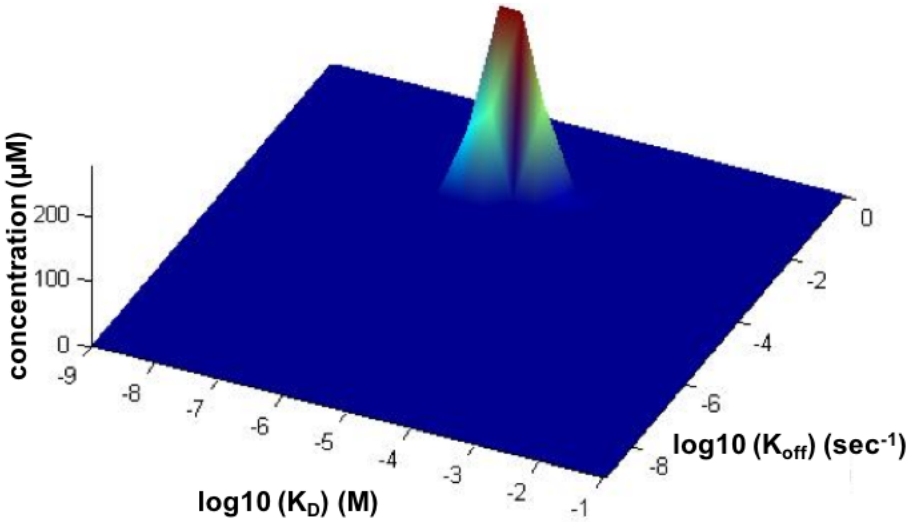

Figure 33: Representative 3-D contour plot of the αX I-domain binding to its ligand at different concentrations of Mg^{2+}. The 3-D distribution plot demonstrating the αX I-domain-ligand affinity as the equilibrium dissociation constant (K_D) as x-coordinates, the dissociation rate constant (k_{off}) as y-coordinates and the abundance of the probed interaction(s) as z-coordinates for the αX I-domain binding to its ligand.

We observed that the fibrinogen-coated surfaces produced robust SPR signals for the WT and SILEN αX I-domain at different Mg^{2+} concentrations (Figure 34). These sensograms provided two-dimensional differential distribution plots that were further processed to assess the structural heterogeneity and determine the affinity constants (Figure 35).

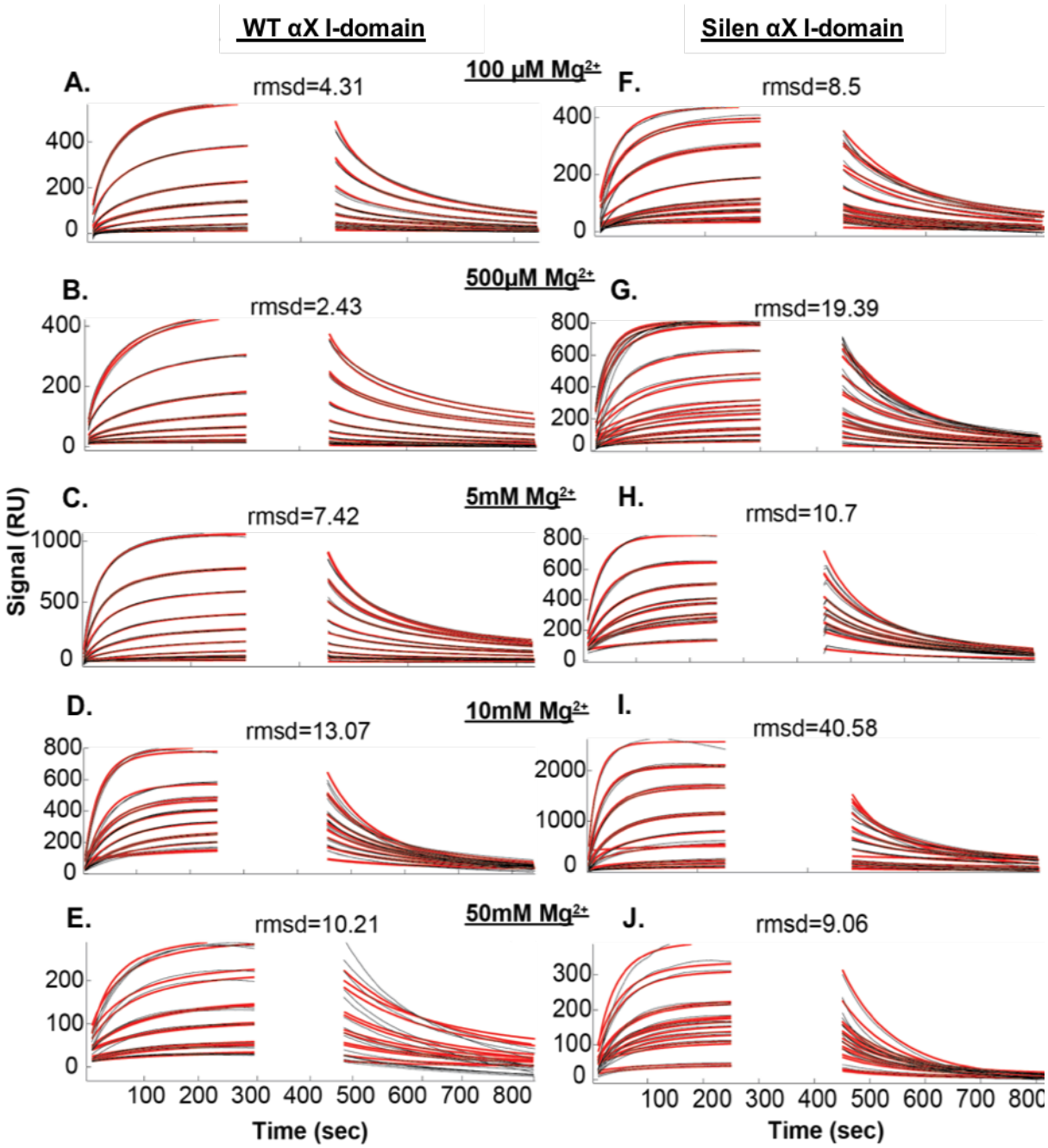

Figure 34: SPR measurements of αX I-domain binding to fibrinogen at different concentrations of Mg^{2+}. The sensograms were fitted using EVILFIT software at Mg^{2+} concentrations of 100 μM, 500 μM, 5 mM, 10 mM, and 50 mM, respectively for the **(A-E)** WT αX I-domain and **(F-J)** SILEN αX I-domain. The sensograms were aligned using the software-Scrubber before the fitting them by EVILFIT.

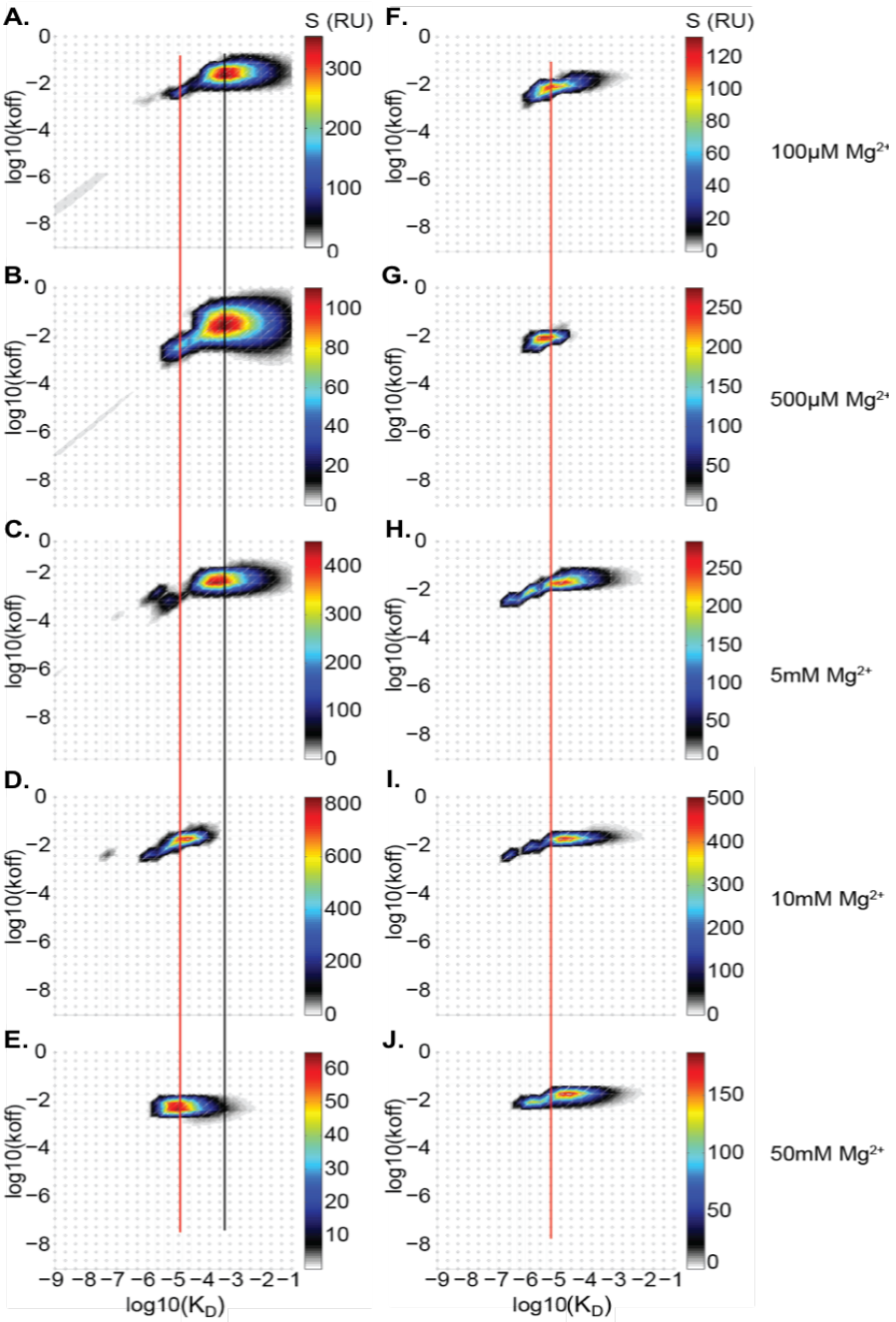

Figure 35: Distributions of the αX I-domain binding interactions to its ligand, fibrinogen at different concentrations of Mg^{2+} depict step-wise affinity maturation of the WT αX I-domain. Results reporting K_D (in M) and k_{off} (in sec^{-1}) distributions were calculated with standard Tikhonov-Phillips regularization using EVILFIT analysis for **(A-E)** the WT αX I-domain and **(F-J)** the SILEN αX I-domain at indicated Mg^{2+} concentrations. The distributions are presented as a contour plot with the color temperature interpolated from the αX I-domain population at the K_D and k_{off} coordinates.

Using the contour map, we analyzed the distribution of binding sites for αX I-domain-ligand interactions (Figure 35). At 100 μM and 500 μM Mg^{2+}, the WT αX I-domain binding to fibrinogen indicated the existence of a mixed ensemble of WT αX I-domain conformations in solution. This conformational ensemble was depicted by a major population demonstrating a lower affinity with a K_D around 10^{-3} M and a minor population showing higher affinity with a K_D around 10^{-5} M (Figures 35A, B). Upon increasing Mg^{2+} concentration to 5 mM, the main K_D peak shifted towards a higher affinity state (412 μM). Also, the heterogeneity of the major conformational ensemble on the K_D/k_{off} matrix was reduced (Figure 35C). At 10 mM and 50 mM Mg^{2+}, the affinity was fully matured and reached high affinities with K_D values of 16.8 μM and 22.2 μM, respectively. At higher Mg^{2+} concentrations, the structural heterogeneity of the WT αX I-domain reached a minimum, as shown by reduced dispersity in the contour map (Figures 35D, E). It is important to note that the conventional equilibrium association constant (K_A) measurement using single-site binding was around 10^4 M^{-1} (Table 10), which is roughly average of observed major affinities in 2D-EVILFIT sensograms (Figure 35 and Table 12).

Unlike the WT αX I-domain, increasing the Mg^{2+} concentration from 100 μM to 50 mM did not induce a stepwise affinity maturation of the SILEN αX I-domain in binding to fibrinogen, and the 2D-space of the K_D-k_{off} binding surface did not appear to shrink (Figures 35F-J). At all Mg^{2+} concentrations, the SILEN αX I-domain exhibited similar affinities to fibrinogen, ranging from 4.3 μM to 17.9 μM. These observations in the SPR binding events suggested that the SILEN αX I-domain exists in a limited conformational heterogeneity in comparison to the WT αX I-domain.

Notably, in the contour map distributions, the k_{off} value throughout all Mg^{2+} concentrations changed minimally. With increasing Mg^{2+} concentration, the k_{off} values decreased slightly in the range of 0.022—0.005 sec^{-1} for the WT αX I-domain and increased marginally in the range of 0.007—0.016 sec^{-1} for the SILEN αX I-domain (Table 12). From the equation of $K_D = k_{off}/k_{on}$, we determined that the variations observed in the K_D values were resulted from the association rate (k_{on}) values (Table 12).

From 100 μM to 10 mM Mg^{2+}, the observed increment in the k_{on} values from 24.74 $M^{-1}sec^{-1}$ to 809.52 $M^{-1}sec^{-1}$ endowed an increase in affinity of the WT αX I-domain to fibrinogen. At a high Mg^{2+} concentration of 50 mM, the k_{on} was slightly reduced to 238.74 $M^{-1}sec^{-1}$ and k_{off} was reduced to 0.005 sec^{-1} (Table 12).This concurrent decrease in the k_{on} and k_{off} values led to ~3-fold lower affinity of the WT αX I-domain binding to fibrinogen at 50 mM Mg^{2+} than that at 10 mM Mg^{2+}.

Table 12: Equilibrium dissociation constant (K_D), association constant (k_{on}), and dissociation constant(k_{off}) for αX I-domains-fibrinogen binding determined from SPR measurements using EVILFIT algorithm

	αX I-domain (WT)			αX I-domain (SILEN)		
$[Mg^{2+}]$	**K_D (M)**	**k_{off} (sec^{-1})**	**k_{on} ($M^{-1}sec^{-1}$)**	**K_D (M)**	**k_{off} (sec^{-1})**	**k_{on} ($M^{-1}sec^{-1}$)**
100 μM	8.73 x	0.022	24.74	1.14×10^{-5}	0.008	661.40
500 μM	8.00 x	0.022	27.38	0.43×10^{-5}	0.007	1662.79
5 mM	4.12 x	0.019	46.36	1.37×10^{-5}	0.016	1189.78
10 mM	0.17 x	0.014	809.52	1.69×10^{-5}	0.015	881.66
50 mM	0.22 x	0.005	238.74	1.79×10^{-5}	0.015	832.40

These results indicated that the increase in Mg^{2+}-binding to the WT αX I-domain elicits an increase in the fibrinogen affinity. This affinity increase, that we describe as "affinity maturation", arises from an increase in the on-rate. Moreover, the SILEN αX I-domain showed significantly higher k_{on} values than the WT αX I-domain, naturally resulting in its increased affinity to fibrinogen than the WT αX I-domain (Table 12).

We also measured, using ImageJ software, the 2D-K_D/k_{off} counter surface area in Figure 35 that represents the range of binding heterogeneity in the αX I-domain-fibrinogen interaction at different Mg^{2+} concentrations. We observed that these surface areas ranged from 1581—6971 a.u. which increased at Mg^{2+} concentrations from 100 μM to 500 μM Mg^{2+} and declined afterward. In contrast, the surface area values for binding of the SILEN αX I-domain to fibrinogen stayed steady, ranging from 1103—2426 a.u (Table 13 and Figure 36). The minimal change in the SILEN αX I-domain surface area compared to that of the WT αX I-domain throughout different Mg^{2+} concentrations suggested that a less significant structural heterogeneity of the SILEN αX I-domain was introduced via Mg^{2+}-titration (Figure 36). After a progressive or stepwise decrease in the surface area for the fibrinogen- WT αX I-domain with increasing Mg^{2+} concentrations, the area of 2497 a.u. at 50 mM Mg^{2+} was reached, which was similar to that of the SILEN αX I-domain in the same Mg^{2+} concentration (2360 a.u at 50 mM Mg^{2+}) (Table 13). This observation indicated that Mg^{2+}-binding possibly reduces the conformational heterogeneity in interaction of the αX I-domain binding to fibrinogen.

Table 13: Signal surface area of αX I-domain-fibrinogen binding determined from SPR measurements

	Signal Surface Area (a.u)	
[Mg^{2+}]	**αX I-domain (WT)**	**αX I-domain (SILEN mutant)**
100 μM	3650	1952
500 μM	6971	1103
5 mM	4178	2426
10 mM	1581	2075
50 mM	2497	2360

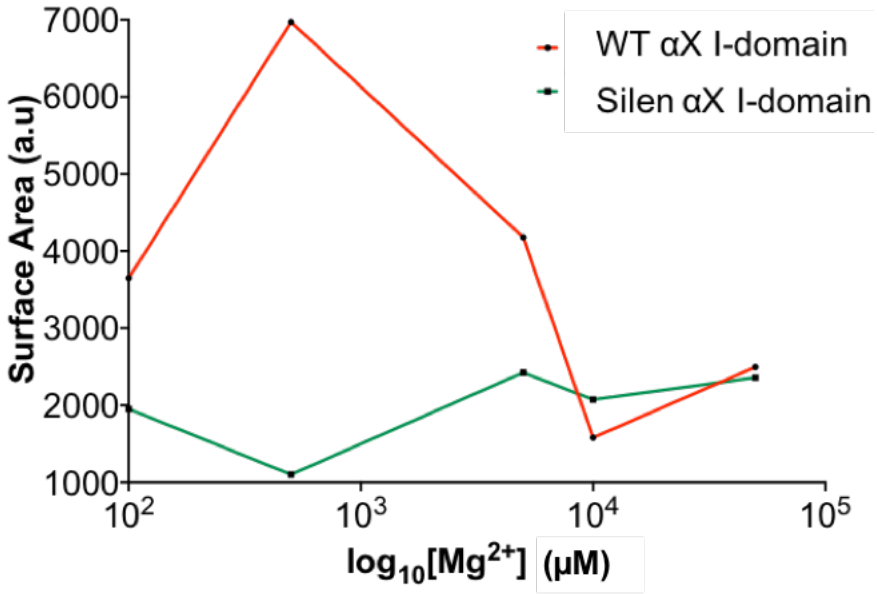

Figure 36: Change in structural heterogeneity of the αX I-domain upon Mg^{2+}-binding. Decrease in the surface area for the WT αX I-domain binding to fibrinogen (red line) was observed with increase in Mg^{2+} concentrations. Mg^{2+}-binding did not exhibit similar effect on the SILEN αX I-domain (green line).

Next, we carried out SPR binding analysis of the αX I-domain to iC3b-coated surfaces (Figure 37).

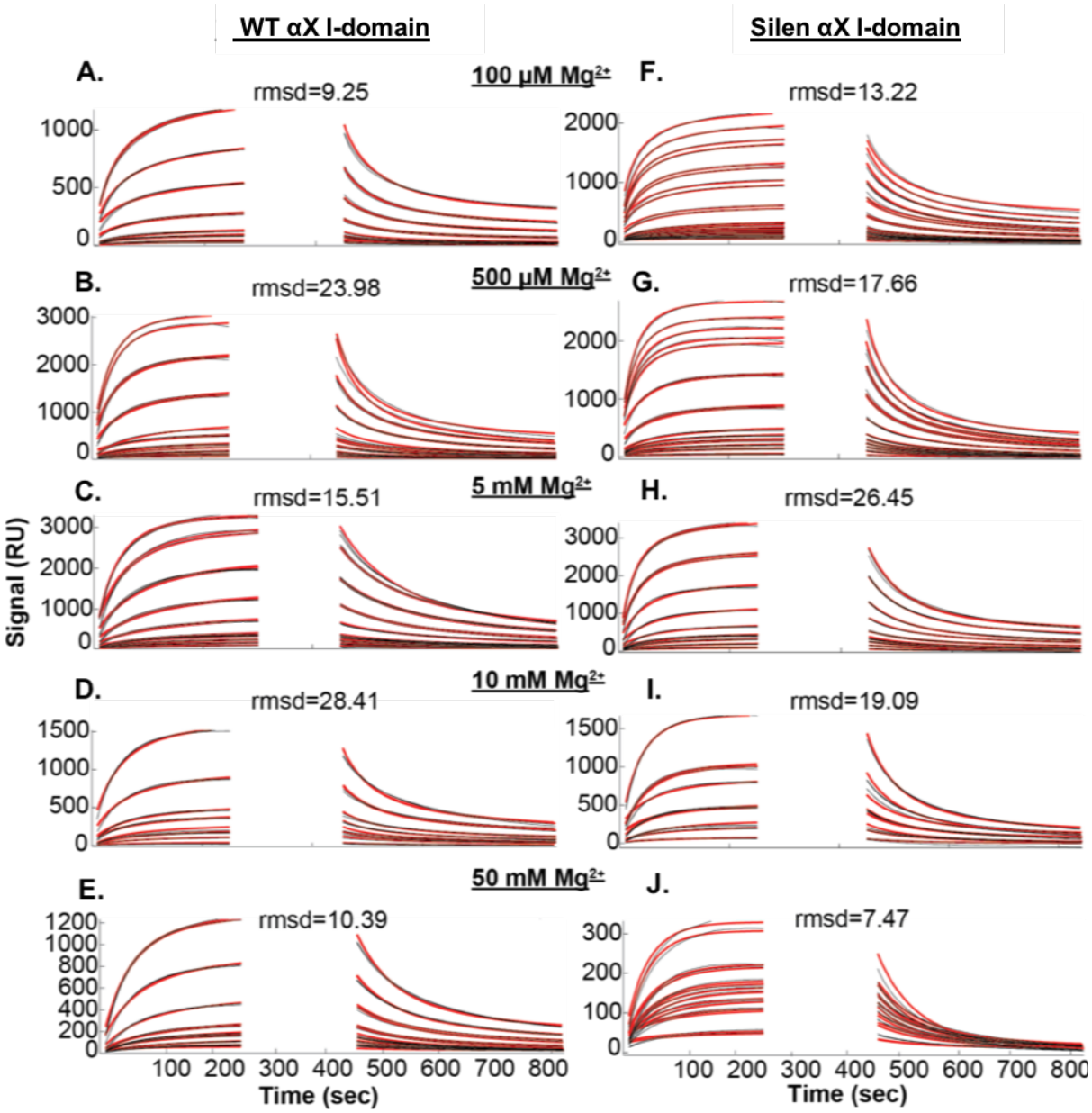

Figure 37: SPR measurements of αX I-domain binding to iC3b at different concentrations of Mg^{2+}. The sensograms were fitted using EVILFIT software at Mg^{2+} concentrations of 100 μM, 500 μM, 5 mM, 10 mM, and 50 mM, respectively for **(A-E)** the WT αX I-domain and **(F-J)** the SILEN αX I-domain. The sensograms were aligned using the software-Scrubber before the fitting them using EVILFIT.

From the 2D-contour maps for the WT αX I-domain at Mg^{2+} concentrations ranging from 100 μM to 5 mM Mg^{2+}, we observed a major population demonstrating a lower affinity with K_D of 10^{-4} M and a minor population showing higher affinity with K_D of 10^{-5} M for the WT αX I-domain binding to iC3b (Figures 38A-C).

At 100 μM and 500 μM where the αX I-domain MIDAS is not saturated with Mg^{2+}, the WT αX I-domain exhibited lower affinity to iC3b with K_D values of 200 μM and 322 μM, respectively (Table 14). At higher Mg^{2+} concentrations, the main K_D peak slightly shifted towards a higher affinity with K_D values of 161 μM, 25.2 μM, and 132 μM at 5 mM, 10 mM, and 50 mM, respectively (Table 14). At 10 mM and 50 mM Mg^{2+}, the major K_D peak shifted towards higher affinity as the minor population at K_D of 50 μM was diminished (Figures 38D, E). These observations indicated the existence of a mixed ensemble of WT αX I-domain conformations in solution, which was similarly observed in WT αX I-domain binding to fibrinogen.

Interestingly, unlike the heterogenous interactions observed for SILEN αX I-domain-fibrinogen, we observed a stepwise shift towards a higher affinity with increasing Mg^{2+} concentrations for the SILEN αX I-domain binding iC3b. The SILEN αX I-domain showed similar lower affinity to iC3b at 100 μM and 500 μM with K_D of 1.27 mM and 855 μM, respectively. At higher Mg^{2+} concentrations, the affinity significantly increased with K_D values of 95.1 μM, 133 μM, and 18.6 μM at 5 mM, 10 mM, and 50 mM Mg^{2+}, respectively (Table 14). Furthermore, the 2D-K_D/k_{off} binding matrix diminished at higher concentrations of 5 mM to 50 mM for both WT and SILEN αX I-domain (Figures 38C-E and 38H-J).

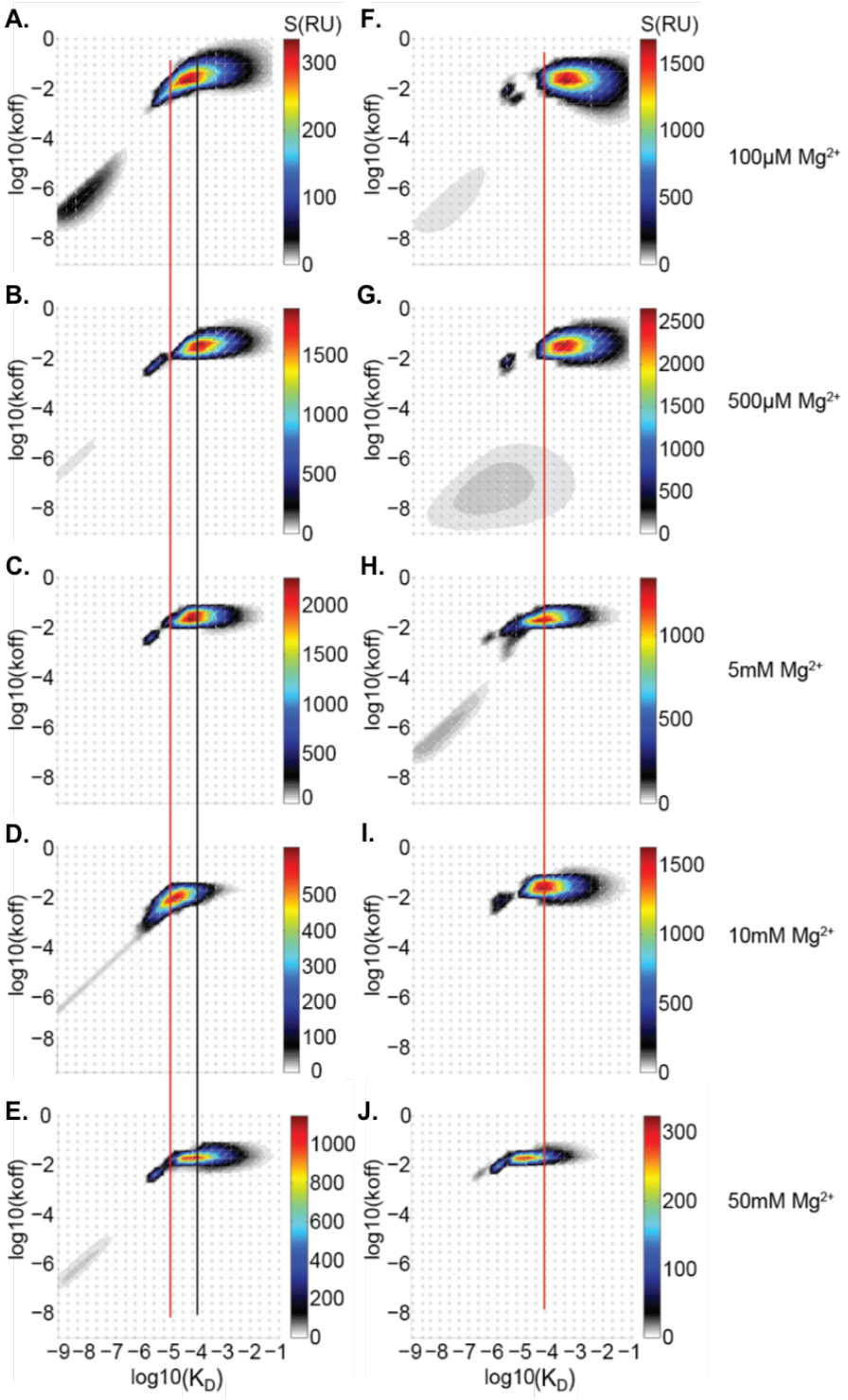

Figure 38: Distributions of the αX I-domain binding interactions to its ligand, iC3b at different concentrations of Mg^{2+} depicts affinity maturation of the αX I-domain upon increase in Mg^{2+} concentrations. Results reporting K_D (in M) and k_{off} (in sec^{-1}) distributions were calculated with standard Tikhonov-Phillips regularization using EVILFIT analysis for **(A-E)** the WT αX I-domain and **(F-J)** the SILEN αX I-domain at indicated Mg^{2+} concentrations ranging from 100 μM to 50 mM.

Table 14: Equilibrium dissociation constant (K_D), association constant (k_{on}), and dissociation constant (k_{off}) αX I-domains-iC3b binding determined from SPR measurements using EVILFIT algorithm

	αX I-domain (WT)			αX I-domain (SILEN)		
[Mg^{2+}]	**K_D (M)**	**k_{off} (sec^{-1})**	**k_{on} ($M^{-1}sec^{-1}$)**	**K_D (M)**	**k_{off} (sec^{-1})**	**k_{on} ($M^{-1}sec^{-1}$)**
100 µM	2.00 x 10^{-4}	0.031	154.50	12.7 x	0.020	15.35
500 µM	3.22 x 10^{-4}	0.031	94.72	8.55 x	0.032	36.84
5 mM	1.61 x 10^{-4}	0.024	147.20	0.95 x	0.021	223.97
10 mM	0.25 x 10^{-4}	0.008	307.14	1.33 x	0.024	177.44
50 mM	1.32 x 10^{-4}	0.017	131.82	0.19 x	0.018	973.12

The dissociation constant (k_{off}) values for the WT αX I-domain-iC3b interactions at 100 µM and 500 µM Mg^{2+} remained consistent at 0.031 sec^{-1} and decreased at higher Mg^{2+} concentrations. However, the k_{off} values varied throughout the range of Mg^{2+} concentrations for the SILEN αX I-domain-iC3b interactions (Table 14).

The surface area depicting the binding of the WT αX I-domain to iC3b ranged from 2241—4317 a.u. and the SILEN αX I-domain binding to iC3b was observed in the range of 1484—4911 a.u (Table 15 and Figure 39). The stoichiometry of αX I-domain binding to iC3b reported suggests approximately six different binding sites for the αX I-domain in iC3b (137). This binding site heterogeneity could result from the structural heterogeneity of the αX I-domain or multiple available binding site of the immobilized iC3b, or both. In contrast, the αX I-domain binds to a single distinct site at Gly-Pro-Arg in the N-terminal domain of the α chain of fibrinogen. This distinct interaction site for αX

I-domain binding to fibrinogen allowed us distinctly to observe αX I-domain affinity maturation in our αX I-domain-fibrinogen SPR studies.

Table 15: Signal surface area of αX I-domain-iC3b binding determined from SPR measurements

$[Mg^{2+}]$	αX I-domain (WT)	αX I-domain (SILEN mutant)
100 μM	4317	4911
500 μM	3221	3757
5 mM	2372	2772
10 mM	2241	3293
50 mM	2707	1484

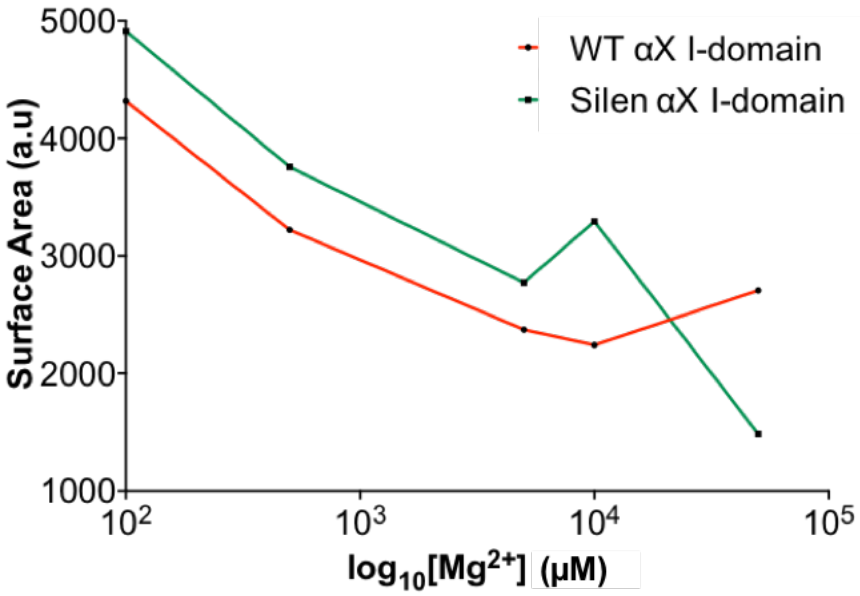

Figure 39: Decrease in the signal surface area of the αX I-domain binding to iC3b with increasing concentrations of Mg^{2+}. Decrease in the surface area for the WT (red line) and SILEN αX I-domain binding to iC3b (green line) was observed with increase in Mg^{2+} concentrations.

3.3 Discussion

3.3.1 Roles of Mg^{2+} in the αX I-domain affinity, stability, and shape-shifting.

3.3.1.1 Affinities of divalent cations to the αX I-domain.

Our studies using ITC showed that the divalent cations exhibited weak association to the αX I-domain at 25 °C with their affinities in the low micromolar range. Studies on the αM I-domain showed binding constants for the divalent cations - Mn^{2+}, Mg^{2+}, and Ca^{2+} at K_D of 33 μM, 555 μM, and 1200 μM, respectively (2). The αL I-domain showed dissociation constant for Mn^{2+}, Mg^{2+}, and Ca^{2+} at K_D of 3.16 μM, 19.42 μM, and 384 μM, respectively (138).

In our studies, a two-fold lower affinity was observed for Mg^{2+}-binding to the WT αX I-domain compared to Mg^{2+} or Mn^{2+}-binding to the SILEN αX I-domain (Section 3.2.2; Figure 19). In similar experiments for the αM I-domain, a 6-fold lower affinity was observed (139). Moreover, Mg^{2+} affinities of the αX and αM I-domains are lower than that of the αL I-domain. In the affinity measurements, binding affinities are measured with the assurance that concentration of proteins and cations are precise, but many external effects could introduce error to the protein or cation concentration. Therefore, binding data, when K_D values have two or more fold difference, must be analyzed cautiously. In the comparison of Mg^{2+} to αI-domains, the αL I-domain has shown remarkable affinity difference, which is more than 10-fold in comparison to the αX and αM I-domains. Interestingly, αL ligands are limited to ICAM molecules, yet the ligands for αX and αM range from ICAMs to fibrinogen and complement molecules. Further detailed work is required to elucidate how cations in MIDAS of each αI-domain play roles in ligand selectivity and affinity, and if the chemical environment around the cation

or local dynamics motions are responsible from selecting ligands and determining the ligand affinities for these αI-domains. For instance, identity between αM and αX I-domains is about 60%, but αL shares only 38% and 33% of identity with αX and αM, respectively. Therefore, it is likely that the ligand specificity by each αI-domain arises from differences in the local molecular environment especially in the vicinity of the MIDAS site.

The difference in the binding-enthalpy contribution of the cations to the αX I-domain could be possibly due to the difference in their electronegativities: 1.55 Pauling units for Mn^{2+}, Mg^{2+} of 1.32 Pauling units, and Ca^{2+} of 1.00 Pauling units (140). The higher the electronegativity of cations, the stronger the degree their electrostatic attraction was with the interacting residues in the hydrophobic core of the αX I-domain. Also, more electrostatic attraction might result in higher affinity. For example, 90% MIDAS occupancy was achieved at the lowest concentration for Mn^{2+} at 800 μM (Figures 25A, B). A higher concentration of Mg^{2+} at 1.5 mM (Figures 24A, B) and Ca^{2+} at 5mM (Figure 25C) was required for complete MIDAS occupancy in our DSF studies.

The favorable entropy observed in the WT αX I-domain upon cation-binding potentially arises from increased configurational entropy due to αX I-domain backbone or side chain mobility during MIDAS reconfiguration and disruption of the hydration shell with released water molecule at the cation binding interface (141-143). One water molecule released from a protein system contributes to ~0.69 kcal/mol to the favorable ΔG (144, 145). The favorable entropies were observed for the WT αX I-domain upon cation binding; $T\Delta S$ of 2.14 kcal/mol, 3.34 kcal/mol, and 3.16 kcal/mol for Mg^{2+}, Mn^{2+}, and Ca^{2+}, respectively. Since one water molecule is released during opening or Mg^{2+}-

binding, which will amount no more than 1.4 kcal/mol, we predict that there is conformational change associated with the observed change in TΔS. In contrast, the Mg^{2+}-binding to SILEN αX I-domain resulted in the decrease in entropy change with TΔS of -1.05 kcal/mol for Mg^{2+} and -2.72 kcal/mol for Mn^{2+}. Thus, cation binding to the SILEN αX I-domain could result in forming a more ordered structure in the presence of Mg^{2+}.

Since the αXβ2 binds promiscuously, the capability of undesirable premature immediate activation must be controlled. This physiological balance of the readiness of the αX I-domain activation is potentially attributed to the low energy difference between the closed and the open states, with the SILEN αX I-domain exhibiting only 10-fold higher ligand affinity than the WT αX I-domain from our affinity studies using physiologically relevant ligands. The low energy difference is possibly due to the αX I-domain's intrinsic flexibility contributed by multiple ensemble states of the αXI-α7 helix. Our observations are supported by the αM I-domain affinity studies showing a 10-fold increase in ligand affinity for the open state αM I-domain than the closed state αM I-domain (83). Strong ligand binding is not necessarily desired from a physiological perspective due to the fact that the ligand is required to release at a certain point of the biological process occurring such as during leukocyte migration, microbial clearance, or immune synapse formation.

3.3.1.2 Mg^{2+} couples MIDAS to the allosteric sites.

The normal mode analysis (NMA), a simulation technique conducted by Zahra Mazhar in our lab, showed that Mg^{2+}-binding residues (Asp-X-Ser-X-Ser motif, Thr 207, and Asp 240) are directly linked to the allosteric sites of the αX I-domain. If the coupling

between the MIDAS and allosteric sites of the αX I-domain is regulated, partially if not fully, by Mg^{2+}, stability and structural changes of the αX I-domain could be probed by DSC and DSF studies via titration of Mg^{2+}.

In DSC, addition of Mg^{2+} increased the T_m of the WT αX I-domain about 10 ^oC and the $\Delta H_{unfolding}$ by 128 kcal/mol. The DSC profile of the SILEN αX I-domain upon Mg^{2+}-binding also showed the similar T_m increase of about 9 ^oC although the $\Delta H_{unfolding}$ was of 19 kcal/mol (Table 6). The SILEN αX I-domain appeared to show two transitions in its DSC profile (Figure 23B). For both WT and SILEN αX I-domain, the changes in T_m and $\Delta H_{unfolding}$ were prominent after reaching approximately 75% saturation in the MIDAS by Mg^{2+}-binding.

In the DSF profiles of the αX I-domain, we detected a drastic change in its T_m after 90% of the MIDAS occupancy was reached. Due to high multiplicity in the dataset, we could quantitatively assess the thermal unfolding event of proteins and statistically verify whether the αX I-domain unfolding followed the mono-phasic or the bi-phasic transition model. The bi-phasic transition model was a better representation of the differential change in the melting profiles of the Mg^{2+}-binding to the αX I-domain which suggested that at least two different conformations exist for the αX I-domain in solution (Figures 24 and 25).

On a technical note, T_m values obtained from DSF and DSC were different for the corresponding conditions, which were potentially due to the dye-binding event contributing positive or negative energetics to the protein unfolding in DSF. Despite the differences in the T_m values, in both DSF and DSC techniques, the αX I-domain

unfolding event during the Mg^{2+}-titration followed almost identical ΔT_m, yet the actual T_m values were determined by DSC.

3.3.1.3 Mg^{2+} modifies ionization states of two critical aspartate residues.

In the cation-less MIDAS, a water molecule is present which directly interacts with Ser 140, Ser 142, Thr 207, and Asp 240 (Figure 40A). In the Mg^{2+}-occupied MIDAS, the oxygen atoms to the primary and secondary coordination sphere around the divalent cation are contributed by five residues of the αX I-domain and several water molecules. Ser 140 is always in the primary coordination sphere regardless of the MIDAS activation status. In the closed state, Asp 240 is in the primary coordination sphere and Thr 207 is in the second coordination sphere (Figure 40B). In Ser 140, Ser 142, and Thr 207 are in the primary coordination sphere, whereas Asp 138 and Asp 240 are in the secondary coordination sphere and fix the positions of coordinating water molecules (Figure 40C). Thus, Asp 138 in both the closed and open state maintains a water-mediated interaction with Mg^{2+}. In contrast, Asp 240 loses direct contact with Mg^{2+} and instead maintains water-mediated interaction on transitioning from the closed to the open αX I-domain state (Figures 40B, C).

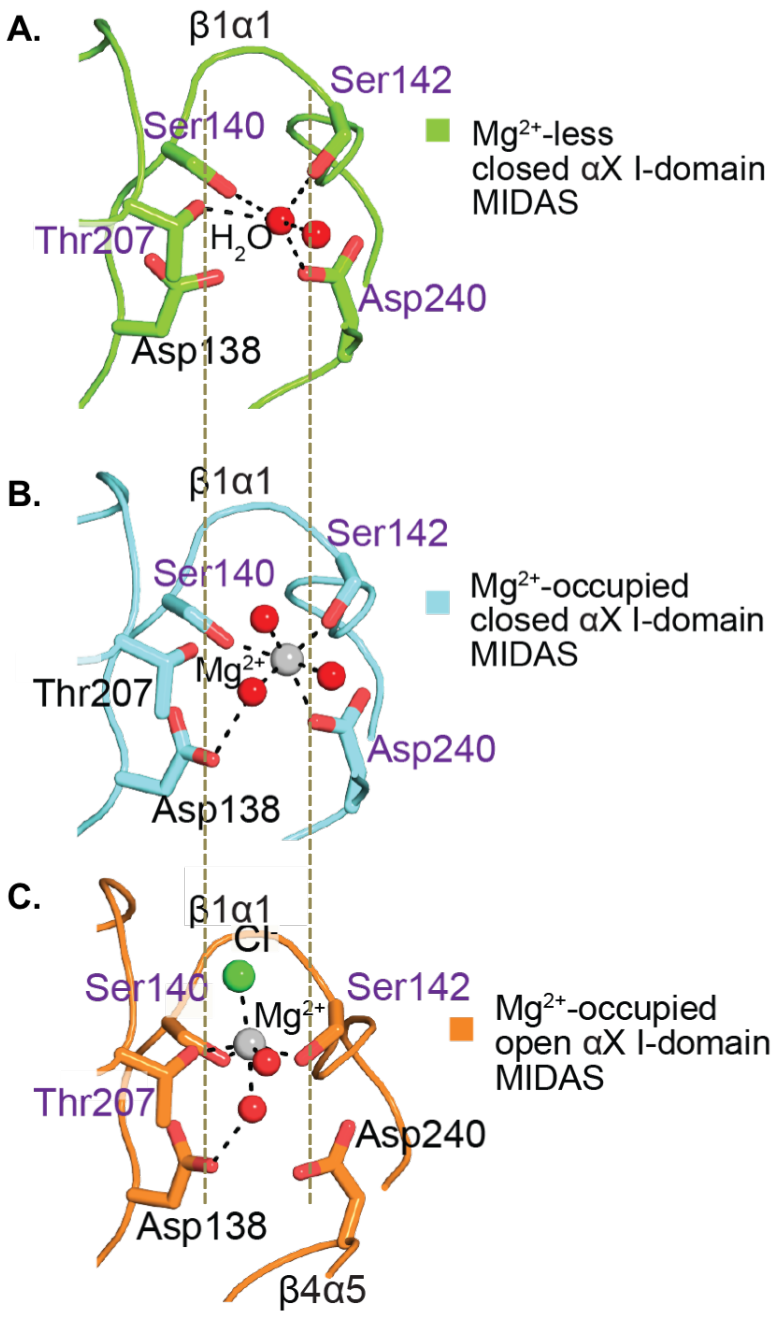

Figure 40: MIDAS coordination of the αX I-domain in the Mg^{2+}-less and Mg^{2+}-occupied conditions. (A) The αX I-domain in cation-less condition has water molecule at MIDAS interacting with Ser 140, Ser 142, Thr 207, and Asp 240. Thr 207 gains and Asp 240 loses direct contact with Mg^{2+} in **(B)** the closed state and instead maintains water-mediated interaction on transitioning to **(C)** the open state of the αX I-domain. 2.5 Å lateral movement of Mg^{2+} on transitioning from closed to open state of the αX I-domain is indicated within the dashed line.

The theoretical isoelectric point (pI) of the αX I-domain is 7.16 with equal number of 21 positively and 21 negatively charged residues as determined by Expasy protparam tool, but pK_as of each negatively and positively charged residues are determined by their microenvironment. The constant pH-MD simulation showed that on moving from the Mg^{2+}-less to the Mg^{2+}-occupied condition, the pK_a values of two aspartate residues, Asp 138 and Asp 240, reduced; Asp 138 from 3.8 to 2.2 and Asp 240 from 5.9 to 3.9. Both aspartates in the MIDAS is present in a hydrophobic sink where Mg^{2+} interactions are surrounded by the conserved hydrophobic residues, such as Ile 137 and Ile 143. Hence, the pK_a values of the ionizable Asp groups must be arranged for maintaining favorable coulombic interactions and lower dielectric constant in the presence and absence of Mg^{2+}.

To experimentally assess whether the Mg^{2+}-binding affects the overall αX I-domain stability at different pH values, we examined the thermodynamics of Mg^{2+}-binding to the αX I-domain. Even though the T_m for the αX I-domain unfolding at both Mg^{2+}-less and Mg^{2+}-occupied conditions did not change while varying the pH (Figure 27A), we distinctly observed the Δ_uG^o of 10 kcal/mol upon Mg^{2+}-binding at the pH range of 3 to 6. In the absence of Mg^{2+}, the Δ_uG^o was at ~5 kcal/mol from pH 3 to 6, and 10 kcal/mol after pH 6. This increase in overall stability of the αX I-domain at a lower pH range in the presence of Mg^{2+} is also potentially linked to the correlation in residue-network from MIDAS to the αXI-α7 helix (or any allosteric sites). Briefly, the ionizable groups potentially make important contributions to the function and stability of proteins to facilitate biological processes as shown in other studies (146-148), and a similar phenomenon of aspartates with atypical pKa alteration upon Mg^{2+}-binding in the αX I-

domain could be playing role in regulating the metal and ligand affinities of the αX I-domain as well as establishing the allosteric coupling between MIDAS and the allosteric sites.

3.3.1.4 Mg^{2+}-binding reduces conformational heterogeneity and enlarges the αX I-domain.

Our in-solution experiments from CD and SAXS showed Mg^{2+}-dependent change in the αX I-domain's helical content and its overall shape. Specifically, the p(r) distribution plot of in-solution SAXS showed two major transitions, if not more, of the αX I-domain upon Mg^{2+}-binding (Figure 29C); the observation that corresponds to the biphasic denaturation observed in our DSF studies (Figures 24A, B). The first transition phase possibly indicates the structural changes in the αX I-domain when Mg^{2+}-dependent coupling between MIDAS to the αXI-α7 helix or other undefined allosteric regions is established—the residue network connecting MIDAS to the αXI-α7 helix as shown by our NMA analysis. In this stage, the MIDAS is not fully saturated with Mg^{2+}. The second transition phase potentially corresponds to the Mg^{2+}-dependent affinity maturation event, which was observed in the SPR (Figures 35D, E) and the cell-based assays (performed by Zeinab Moussa in our lab). Indeed, when the affinity matures, the αXI-α7 helix enlarges to roughly to 26 Å (79), which corresponds to the similar change in D_{max} in our p(r) distribution plot. The indication of the second transition stage is also supported by our DSF analysis in which the stability of the αX I-domain increases drastically after approximately 70% MIDAS saturation by Mg^{2+}-binding. The two distinct ensemble populations observed in SAXS analysis reinforced the occurrence of biphasic

structural transition of the αX I-domain upon Mg^{2+}-addition as observed in our DSC and DSF studies.

Even though our solution SAXS experiments showed the enlargement and existence of at least two intermediate states of the αX I-domain during its structural changes upon Mg^{2+}-binding, this technique only provides summation of all conformational ensembles (149). Therefore, determining the number of intermediate states in solution is challenging when using experimental strategies such as crystallography and cryo-EM, but indirect evidence can be obtained by computational analysis of NMR observables. Furthermore, the 3D NMR spectra of the Mg^{2+}-bound αX I-domain showed evidence of peak splitting of residues at the MIDAS and the α7 helix indicating the structural changes at these regions of the αX I-domain upon Mg^{2+}-binding. These NMR datasets validated that the addition of Mg^{2+} induced the αX I-domain to adopt at least two different conformational states in solution. It is imperative to note that this conformational heterogeneity is the most likely culprit in crystallization of the αX I-domain in the metal-bound condition in my and others' crystallization efforts. Interestingly, the crystal structure of the isolated αX I-domain with a metal bound to MIDAS is not available even though structure of the metal-bound isolated αM I-domain (121, 150), αL I-domain 87, 151), and αD I-domain (from the Şen lab, Collins Aboagye's unpublished results) have been determined.

3.3.1.5 Mg^{2+} matures ligand affinity of the αX I-domain.

In our SPR affinity measurements, we observed highly dispersed affinity values for the WT αX I-domain binding to fibrinogen in the non-saturating Mg^{2+} concentrations until 500 μM Mg^{2+} (Figures 35A, B and 36). The increase in the ligand affinity of the WT

αX I-domain appeared to be evident at Mg^{2+} concentration of 5 mM. Moving towards Mg^{2+}-saturated MIDAS, the observed heterogeneity in αX I-fibrinogen binding is essentially skewed to more homogenous interactions as revealed by reduction in surface area (Figures 35 C-E). The SILEN αX I-domain in all Mg^{2+} conditions showed similar affinities in the 2D-binding isotherms (Figure 35 F-J), and the 2D-counter surface area did not change significantly throughout all conditions (Figure 36). These observations indicated that the SILEN αX I-domain did not undergo similar affinity maturation event during Mg^{2+}-titration, but has a fixed-affinity. This observation is highly expected because Ile 314→Gly mutation locks the αX I-domain in an alternate high-affinity state.

There could be two different explanations for detecting heterogenous ligand-binding events. The first reason could be that the fibrinogen immobilized to the sensor chip has high structural heterogeneity such as different post-translational modifications and non-specific proteolysis. The second reason could be that the αX I-domain structure is heterogenous. The first scenario is unlikely because, in all of the affinity measurements, we used the same fibrinogen-bound surface in our binding SPR experiments and confirmed the reproducibility of our binding curves—showing always same SPR surface activity. Therefore, it would be expected that the observed heterogenous ligand binding events solely resulted from the structural heterogeneity of the αX I-domain.

In a second experiment, we decided to use iC3b as a ligand because the stoichiometry reported in a previous study for the αX I-domain binding to iC3b suggests possibility of their six different binding interfaces on iC3b (137), each of which might

have a different affinity. As expected, iC3b-SPR binding analysis is challenging. Based on the analysis using maximum entropy regularization, multi-binding sites on the iC3b and the conformational heterogeneity of the αX I-domain became obstacles when distinctly refining the affinity values in these SPR measurements. Yet, the WT αXI-domain binding to iC3b in the conventional 1:1 binding analysis showed increase in overall affinity during Mg^{2+}-titration (Figure 37 and Table 11).

Our findings on structural heterogeneity and affinity maturation of the αX I-domain by the SPR analysis were further confirmed by testing functional relevance of the Mg^{2+}-dependent affinity maturation events on cell surface-expressed αXβ2 receptors (this experiment was done by Zeinab Moussa-The Şen lab). The αXβ2-HEK293T transfected cells at saturating Mg^{2+} conditions also induced increased affinity to iC3b-sensitized erythrocytes in physiologically-relevant rosetting assays. We were certain that the increased affinity solely depended on the Mg^{2+}-induced αX I-domain opening event. This confirmation was based on two mechanistically different approaches with an inhibitory monoclonal antibody, TS1/18, and small-molecule inhibitor, XVA 143, respectively, used for inhibiting the αI/βI domain coupling event.

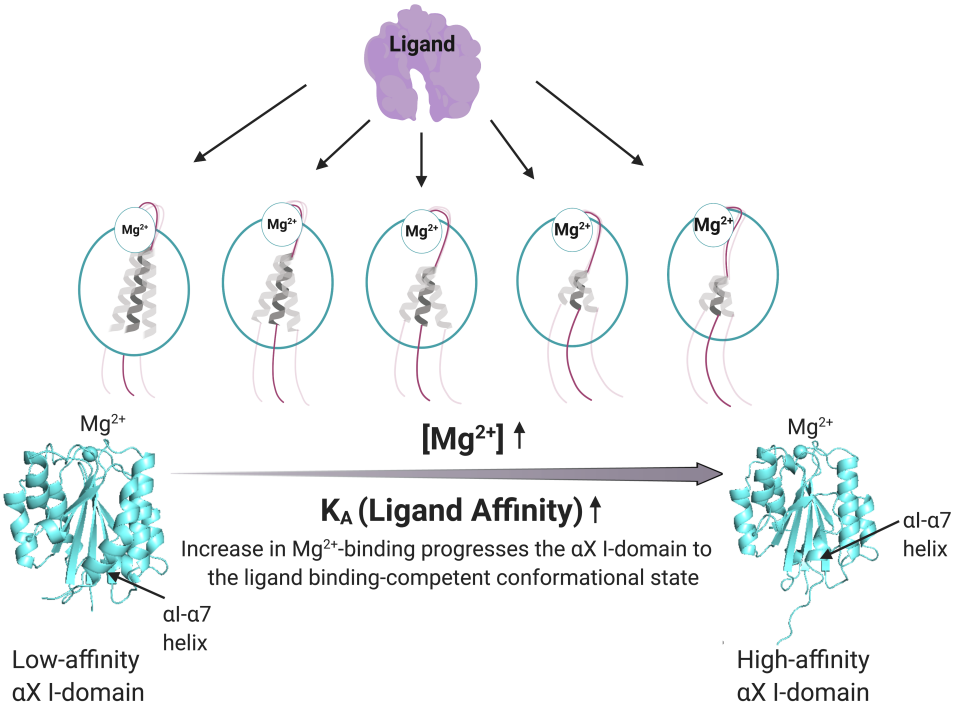

Figure 41: Schematic representation of the effect of Mg^{2+}-binding on the αX I-domain conformation and its ligand affinity.

In conclusion, my studies elucidated the roles of Mg^{2+} in the αX I-domain structural changes and its ligand-binding mechanism. We demonstrated that the Mg^{2+} induces conformational changes in the αX I-domain and biases its thermodynamic equilibrium towards the ligand-binding competent state(s) (Figure 41). We showed that the overall αX I-domain stability is directly linked to its MIDAS occupancy, where two critical aspartate residues appear to couple MIDAS to the rest of the αX I-domain. The binding-competent intermediate states of the αX I-domain existing in solution and minimal ligand affinity difference between the closed and the open state could contribute to the widescale conformational changes of the αXβ2. These conformational changes of the αXβ2 enable this promiscuous receptor to respond instantaneously to multiple ligands and allow leukocytes to mount appropriate rapid immune response to function in the innate immunity.

CHAPTER 4

SIMVASTATIN BINDS AND ACTS AS AN ANTAGONIST TO THE αX-I DOMAIN.

4.1 Introduction

Immune surveillance is guided by the regulation of adhesion and migration of myeloid cells like leukocytes. The aberrant leukocyte migration contributes to inflammatory responses in many immune dysregulations such as atherosclerosis, autoimmune encephalitis, arthritis, and Leukocyte Adhesion Deficiency (LAD) (23, 27, 37, 151). The regulation of integrin αXβ2 is a crucial process involved in recruiting leukocytes from circulation to atherosclerotic lesions (152). In the αX (CD11c) $^{-/-}$ and apolipoprotein E (apoE)$^{-/-}$ -deficient mouse model of hypercholesterolemia, the αXβ2 expression was shown to increase on blood monocytes (152). The αX-deficiency decreased firm adhesion of monocytes on the adhesion molecules, VCAM-1 and E-selectin, and reduced atherosclerosis in these mice (37). These studies demonstrated that integrin αXβ2 overexpression contributes to the development of atherosclerosis associated with hypercholesterolemia, which is pathologically characterized by leukocyte activation, migration across inflamed endothelium, and its deposition on the arterial walls. Therefore, αXβ2 antagonism could be a conducive approach in treating atherosclerotic pathologies in which leukocytes are unconventionally activated due to inflammation. The implications of αXβ2 in multiple autoinflammatory pathologies indicate that this receptor expressed on the extracellular surface could be a promising target for anti-inflammatory therapies.

Studies undertaken with leukocyte integrin blocking antibodies have shown a reduction in delayed-type hypersensitivity, monocyte adhesion to epithelial cells, and

inhibition of superoxide production (42, 153). Targeting β2-integrins using antibody-based therapies has been challenging wherein treatment with efalizumab resulted in fatal progressive multifocal leukoencephalopathy (154). Therefore, to overcome this challenge, identifying non-antibody-based antagonists of αXβ2 is an attractive approach. Despite accumulating literature of small molecule acting as antagonists or agonists to β2-integrins, current lack of αXβ2 inhibitors in clinical use could be attributed to a substantial gap in knowledge of β2-integrin activation at the molecular level (155-158).

Identifying a small molecule antagonist to the αX-I domain and determining its binding mechanism can aid in better understanding the αX-I domain's conformational changes, which is directly related to αXβ2 activation. Remarkably, simvastatin has been shown to bind to the αM I-domain, a sister homolog of the αX I-domain (107).

In this study, we identified hydroxy-form of simvastatin as an αXβ2 antagonist and characterized the structural basis for its mode of action. We utilized the following biophysical techniques in probing simvastatin- the αX I-domain interaction studies.

Heteronuclear Single Quantum Coherence (HSQC): In the protein ^{15}N-HSQC experiment, the nitrogen nuclei within the ^{15}N-labeled protein correlate to hydrogen (^{1}H) atoms attached to them (Figure 42). The HSQC spectrum shows one signal for every amino acid residue, which is the backbone N-H signal, except for proline, to which no peak corresponds (159).

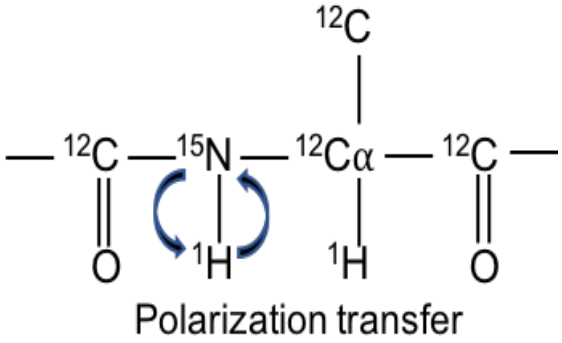

Figure 42: Representation of the active route by which magnetization is transferred between nuclei by spin-spin J coupling. In the ^{1}H-^{15}N-HSQC, the magnetization is transferred from hydrogen to the corresponding ^{15}N nuclei. The magnetization is evolved on the nitrogen and then transferred back to the hydrogen for detection.

The acquired $^{1}H/^{15}N$ spectrum provides a fingerprint of the protein to be used as a reference spectrum. A subsequent experiment utilizes a ligand titration approach using the ligand to follow changes in the protein target resonances in relation to the concentration of the ligand. A significant shift in the resonance position of a peak in the protein-ligand spectrum compared to the reference spectrum might show ligand binding to the protein. This interaction results in modifications in the interacting sites' chemical environment, and consequently, causes amino acid residue-specific chemical shift perturbations of the nuclei at the binding interface or at allosteric sites. The ligand titration method allows measurement of protein-ligand dissociation constant (K_D) through correlations of fractional chemical shift perturbation with total ligand concentration, assuming that the rate of complex dissociation (k_{off}) is quick on an NMR timescale (159).

HSQC here involves a transfer of magnetization from the proton's (^{1}H) nucleus to the nitrogen's (^{15}N) nucleus using the INEPT (Insensitive Nuclei Enhancement by

Polarization Transfer) pulse sequence (a signal enhancement method) (Figures 42 and 43) (160). An INEPT sequence followed by t1 evolution time allows the indirect detection of the ^{15}N chemical shifts. The mixing time used corresponds to a reverse INEPT sequence. A t2 evolution time enables the direct detection of ^{1}H chemical shifts. The proton (^{1}H) exhibits a greater equilibrium magnetization and creates a stronger signal (159, 160).

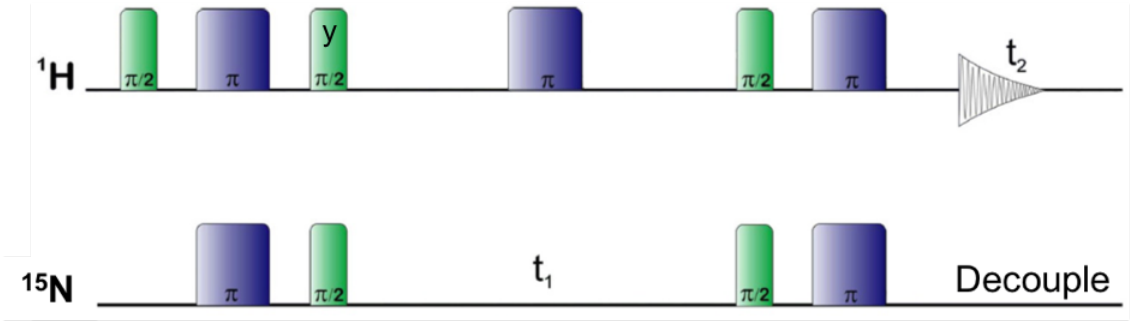

Figure 43: Pulse sequence for observing heteronuclear ^{1}H-^{15}N correlations using the HSQC experiment. The magnetization from ^{1}H is transferred to the ^{15}N nuclei. After refocusing the evolution of the coupling using a centrally placed ^{1}H 180°pulse in the middle of t1. The magnetization is transferred back to the ^{1}H where the correlation is observed t2.
Adapted from *Ljubica Tasic et al. (2015). Monitoring intermolecular and intramolecular interactions by NMR spectroscopy. Applications of NMR Spectroscopy., Vol. 3, 180-266.*

Saturation Transfer Difference (STD): STD is a powerful NMR method based on intramolecular and intermolecular magnetization transfer *via* the Nuclear Overhauser Effect (NOE) (161). NOE is defined as the change in the intensity of one spin when the spin transition of another nucleus in the spatial proximity is perturbed from equilibrium population due to saturation (162, 163). STD permits the detection of protein-ligand interaction and, in favorable cases, allows the ligand epitope to be inferred. The chemical exchange of a given molecule between a free state or protein-bound state is identified by this experiment (164). For a strong STD signal, the irradiation time of 2

seconds and a 100-fold excess of the ligand are typically implemented (165). Technically, STD examines the difference between two ^{1}H-NMR spectra acquired from two different experiments.

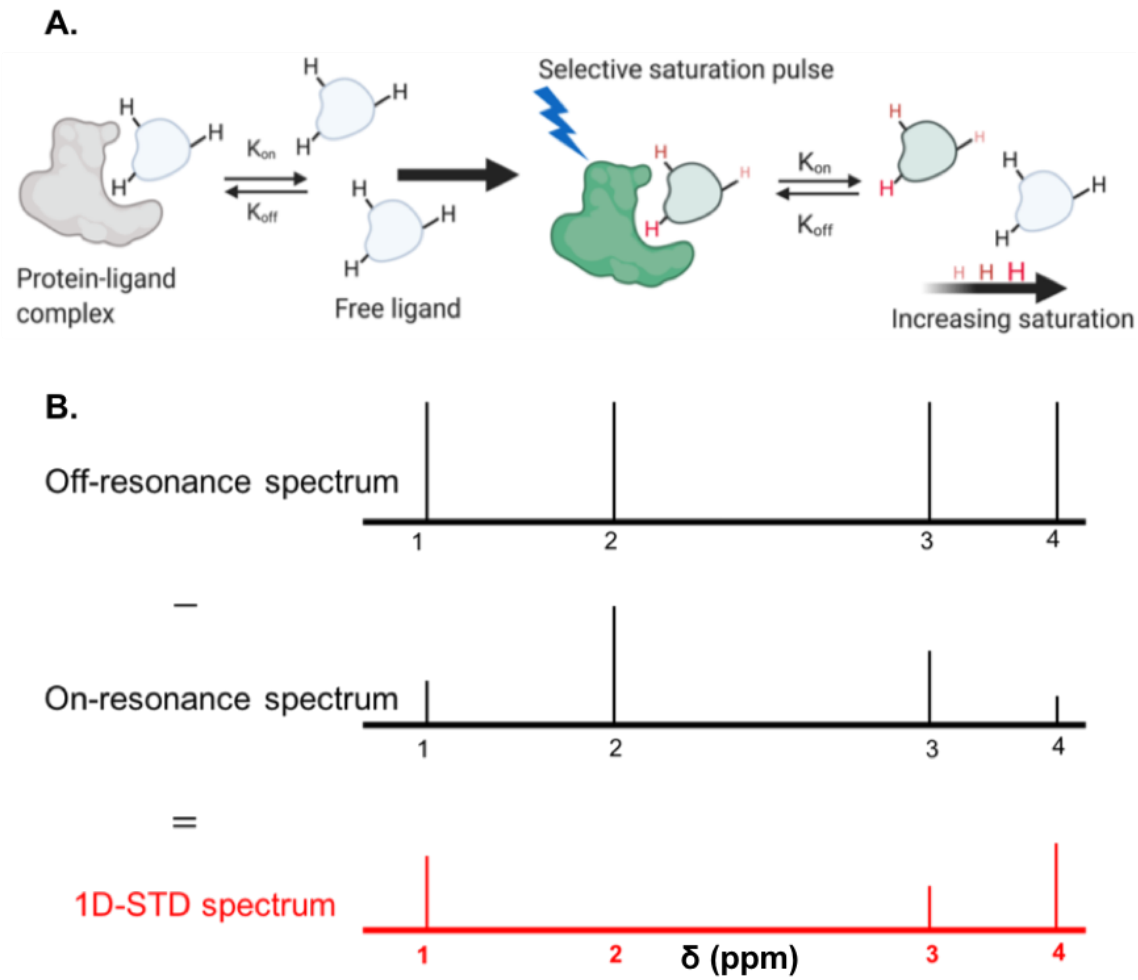

Figure 44: Illustration of the STD experiment scheme. (A) Schematic view of ligand epitope mapping in STD experiment. The protein protons are selectively saturated at a specific frequency. The saturation is then transferred to the interacting ligand. Depending on the proximity to the protein protons, the ligand proton signals are affected differently as indicated by different a colored proton (H) for increasing saturation. **(B)** STD spectrum is generated by subtraction of "on-resonance" spectrum from "off-resonance" spectrum. Created with BioRender.com

The first experiment, called the "on-resonance" experiment, involves various proton magnetizations of the selectively irradiated protein (Figure 44B). The irradiation is carried out through a series of frequency-selective radiofrequency (RF) pulses for a

few seconds. The selective saturation is conducted by applying radiofrequency series to a frequency window containing protein resonance and not the ligand's resonances at least within 1—2 ppm. The saturation is propagated across the entire protein through spin diffusion. It initiates from the point of application to protein protons by intramolecular ^{1}H-^{1}H cross-relaxation pathway (165). The interacting ligand picks up the saturation of protein protons located at the binding site. This process affects the NMR active nuclei of the ligand molecules interacting at the protein binding site. The saturation eventually dissociates back into the free solution where the saturated state remains (Figure 44A). The ligand continues to exchange on and off the protein while saturation energy continues to enter the system through consistent radiofrequency application leading to amplification of the signal (159, 163, 165, 166). The on-resonance irradiation frequency values are typically fixed at the upfield region at approximately -1 ppm for protein-small molecule interactions because this spectral region does not contain ligand nuclei resonances (161). The significant line width of protein signals found in this upfield region allows selective saturation (161).

In the second experiment, called the "off-resonance" experiment, the irradiation frequency is set at a value where no receptor or ligand is present and results in a reference spectrum (Figure 44B). The ligand protons that interact with the protein protons through the intermolecular NOE exhibit a decrease in intensity in the "on-resonance" spectrum, whereas intensity variation does not occur in the "off-resonance" spectrum (Figure 44B). The intensity of the ligand's protons is differentially affected, depending on their distance to the protein binding site (Figure 44A). Saturation is exclusively transferred to protons bound to the protein such that the ligand saturation is

higher for the protons that are in closer contact with the protein. The acquired spectrum from the “on-resonance” experiment is subtracted from the “off-resonance” spectrum (159, 163, 165). The resulting difference spectrum only contains the signals of ligand molecules demonstrating binding affinity (Figure 44B). The protein resonance is either not visible or is scarcely visible due to its minimal concentration or due to the application of relaxation filtering before detection (159). The ligand’s functional groups are identified to determine the interacting molecules at the ligand-binding interface (167). Thus, *the STD technique differentiates binding molecules from the non-binding molecules in a protein-ligand mixture.* STD proves to be a versatile tool that provides evidence of ligand-protein interaction and allows to obtain the ligand epitope mapping (163).

4.2 Results

4.2.1 Affinity measurement of a small molecule - simvastatin to the αX I-domain.

To determine if the small molecule- the hydroxy form of simvastatin binds to the SILEN αX I-domain, we assessed thermal unfolding of the αX I-domain at varying simvastatin concentrations using DSF. The hydroxy-acid form of simvastatin used in our studies is herein simply referred to as simvastatin. We examined the melting temperatures of 11.8 μM αX I-domain with 1 mM Mg^{2+} at different simvastatin concentrations in the range of 0 to 7.5 mM. Interestingly, we observed a decline in the melting temperature of the SILEN αX I-domain with the addition of simvastatin beyond a concentration of 300 μM. This observation indicated that simvastatin bound to the αX I-domain and decreased its stability. Simvastatin, in its hydroxy acid form, was found to bind the αX I-domain with a low affinity at a K_D value of 861± 22 μM (Figure 45).

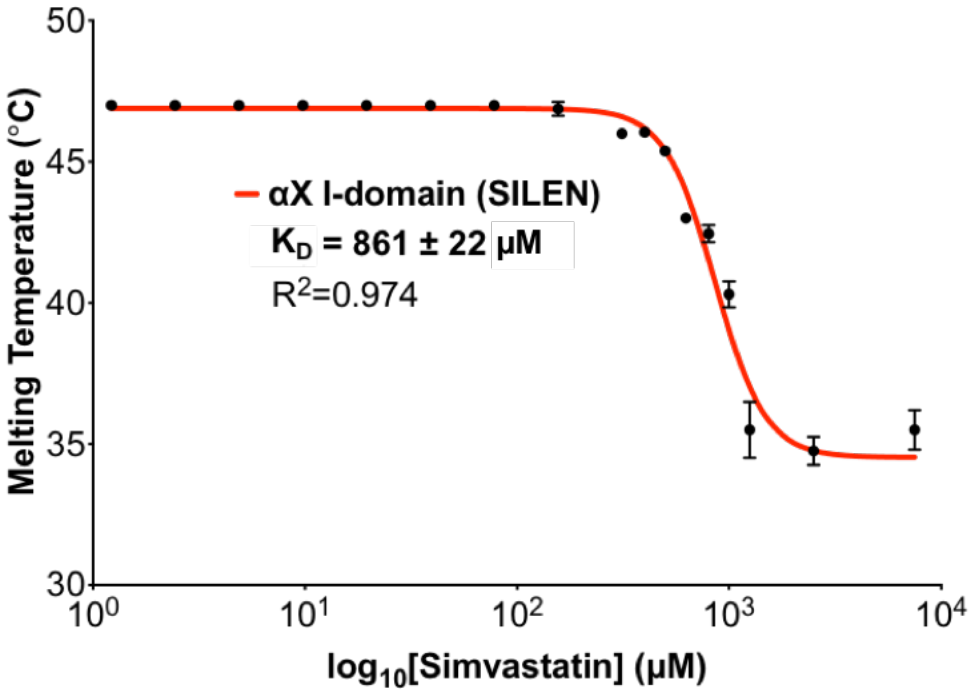

Figure 45: Simvastatin binding to αX I-domain decreases its stability. Decrease in the melting temperature (T_m) of the SILEN αX I-domain from 47 °C to 34.7 °C observed with increasing concentrations of simvastatin ranging from 0-7.5 mM using differential scanning fluorimetry.

To further validate simvastatin's affinity to the αX I-domain, we performed an HSQC-NMR measurement by titrating increasing concentrations of simvastatin to 25 μM ^{15}N-labelled SILEN αX I-domain. Since the Ile 314 Gly mutated (SILEN) αX I-domain represented the endpoint of the high ligand-binding affinity of the αX I-domain, we could observe the maximal affinity of simvastatin to the αX I-domain in this conformational state. The acquisition of ^{15}N-HSQC spectra of the SILEN αX-I domain was carried by titrating simvastatin. The change in the chemical perturbation ($\Delta\delta$) was measured by the peak shift in HSQC spectra of the SILEN αX I-domain residues as shown with a representation in an inset box (Figure 46A). We observed that the simvastatin titration induced a chemical shift in the SILEN αX I-domain spectra. This observation indicated

structural alteration of the αX I-domain due to simvastatin binding. The K_D value for simvastatin affinity to the SILEN αX I-domain was determined to be 202 ± 18 μM (Figures 46A, B). The affinity constant for simvastatin binding to the SILEN αX I-domain determined from NMR data agreed with the result from our DSF study.

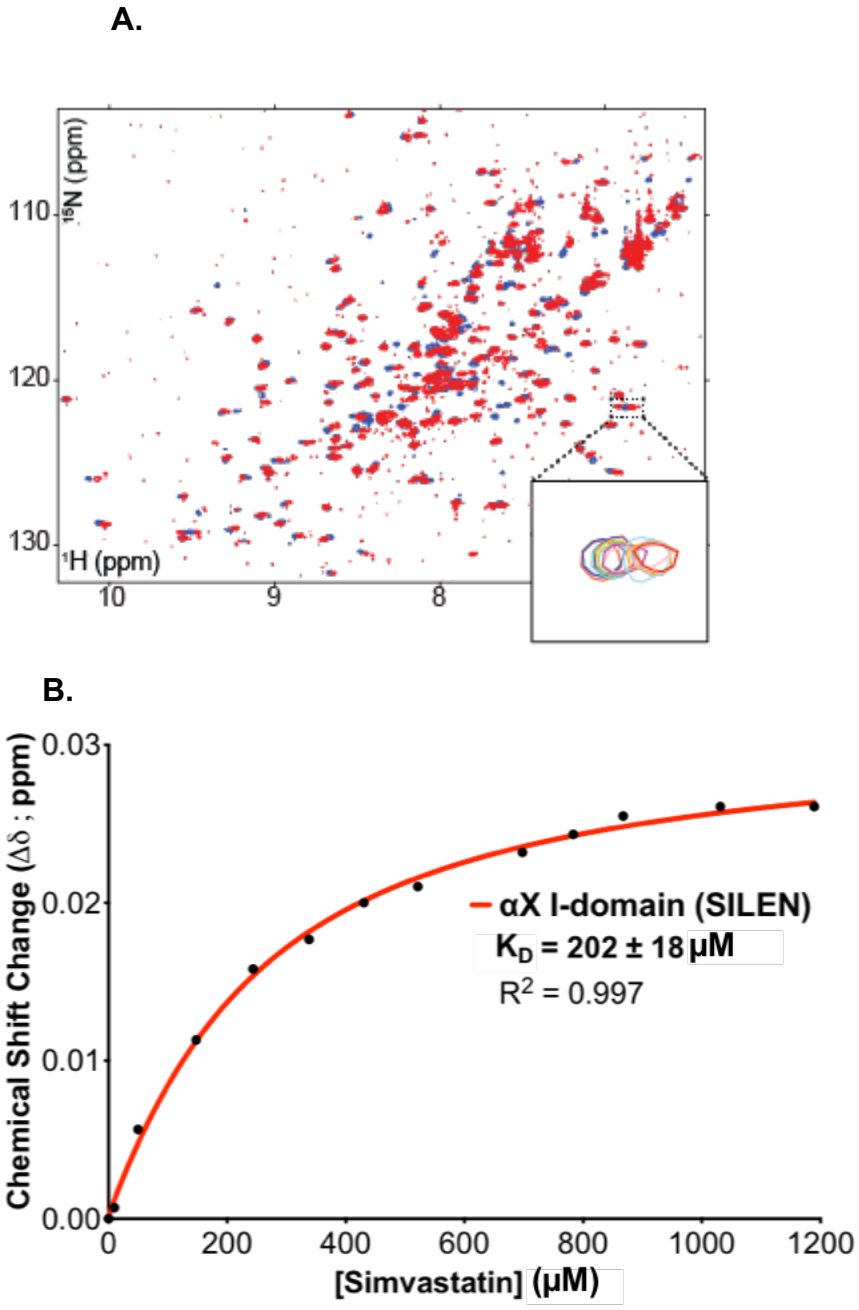

Figure 46: The chemical shift perturbation observed in the ^{1}H/^{15}N HSQC NMR spectra upon simvastatin titration to the SILEN αX I-domain indicated binding of simvastatin to the αX-I domain. (A) 1D ^{1}H/^{15}N HSQC NMR spectra of the SILEN αX I-domain is shown in red and simvastatin-SILEN αX I-domain complex is shown in blue. **(B)** Determination of simvastatin affinity to the SILEN αX I-domain by plotting the change in chemical shift of the SILEN αX I-domain residues upon simvastatin addition.

4.2.2 Molecular basis of the simvastatin-αX I-domain interactions.

Once we established that simvastatin bound to the αX I-domain, we next characterized the simvastatin-αX I-domain binding specificity at an atomic level by identifying the simvastatin moieties involved in this interaction. First, the predicted 1D ^{1}H spectrum of the simvastatin molecule was obtained using the website nmrdb.org (168). We next assigned the spectral signals in this predicted 1D ^{1}H spectrum to the corresponding protons in simvastatin based on Biological Magnetic Resonance Data Bank (Figures 47A, B). This predicted spectrum served as a reference of each proton's spectral position for comparison to the acquired spectra from our STD experiments. The classification of protons from the hydroxy-acid simvastatin molecule to the spectral position was essentially based on the associated functional groups of the molecule.

STD-NMR relied on the intermolecular transfer of saturation from the αX I-domain protons to simvastatin. Simvastatin's spectral window ranged from 1 to 6 ppm. We selectively saturated the αX I-domain outside this spectral window. The magnetization was then transferred to simvastatin by spin diffusion. Utilizing the proton position of simvastatin based on Biological Magnetic Resonance Data Bank shown in Figure 48A, we effectively assigned the proton positions of the simvastatin in our experimental 1D ^{1}H spectrum of simvastatin (black line) and the STD spectra (red line) (Figure 48B).

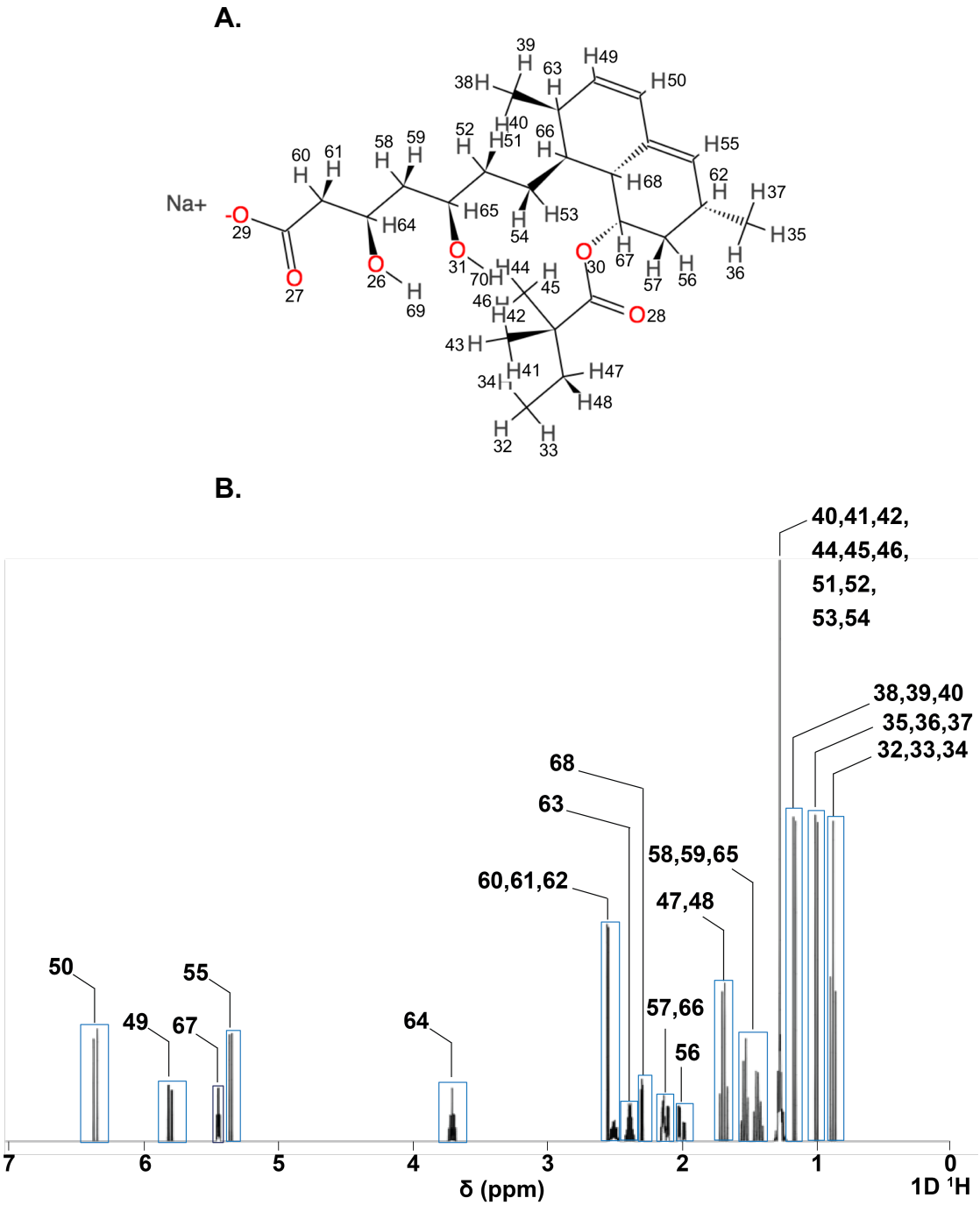

Figure 47: **Assignment of each proton present in hydroxy-acid simvastatin to the predicted 1D ^{1}H spectrum provided a reference map for the protons' estimated spectral position. (A)** Structure of hydroxy-acid form of simvastatin identifying each proton in the molecule. **(B)** Assignment of the signals in the predicted 1D ^{1}H spectrum of hydroxy-acid simvastatin to the corresponding proton in the chemical structure shown in (A).

In our STD experiment, the 1D ^{1}H spectrum of simvastatin is represented by the black line (Figure 48B). The STD-NMR spectrum shown in the red line demonstrates the proton saturation of the αX I-domain transferred to simvastatin. The simvastatin protons' signals were affected differently depending on their proximity to the αX I-domain protons displayed as the relative degree of saturation (Figure 48B). Irradiation of the αX I-domain at a resonance where no ligand signals were present led to a selective and efficient saturation of the αX I-domain by spin diffusion. The building block of simvastatin participating in the strongest contact with the αX I-domain showed the most intense NMR signals enabling the mapping of simvastatin's binding epitope.

Noticeably, in the STD NMR, the aliphatic protons, H32, H33, H34, H35, H36, H37, H38, H39, H40, H41, H42, H43, H44, H45, and H46, of the methyl groups (CH_3) of simvastatin exhibited intermediate intensities at farthest upfield frequency values between 0 and —1.3 ppm (Figures 48A, B) (169). This observation suggested that these methyl groups' interaction contributed, to some extent, to the simvastatin-αX I-domain binding. The weak saturation intensities of H47, H48, H51, H52, H53, H54, H56, H57, H58, and H59, of the methylene groups (CH_2) present in the vicinity of the carboxylic group of simvastatin appeared between 1.3 and —2.0 ppm (169). These protons demonstrating low saturation intensities in our STD NMR spectrum also indicated their interaction at the binding site of the αX I-domain. The highest degree of saturation, which appeared between 3 and 4 ppm, was observed for the H60, H61, H69, and H70, protons near the alcohol (-OH) and carboxylate (-COOH) group of simvastatin where the lactone ring was cleaved. These protons appear to be inserted into the MIDAS region together with the carboxylate and interacts effectively with the protein

residues around it. Also, a good degree of saturation for H64 and H65 protons observed in our STD spectrum provided evidence for the proximity simvastatin's carboxylic group to the protons of the αX I-domain surface with binding specificity in solution (Figures 48A, B). The proton chemical shifts and associated coupling comparing the simvastatin with lactone-ring and hydroxy-form of simvastatin are listed in Table 16. The definitions for chemical shift ambiguity index value can be found in Appendix 3.

These results suggested that simvastatin's interaction with the αX I-domain occurs through its carboxylic group and potentially through its binding to the Mg^{2+} at the αX I-domain MIDAS. The methyl groups' proton saturation transfer indicated that these hydrophobic moieties possibly stabilize the simvastatin at the binding interface *via* hydrophobic interactions and bury the Mg^{2+}-carboxylate interaction.

Figure 48: **Reference 1D ^{1}H spectrum of simvastatin and saturation transfer difference ^{1}H-NMR spectrum of the αX I-domain-simvastatin complex overlayed.** **(A)** Chemical structure of hydroxy-acid form of simvastatin depicting each proton in the molecule. **(B)** Reference 1D ^{1}H NMR spectrum (black) of simvastatin and STD-NMR spectra (red) of the αX I-domain-simvastatin complex demonstrates that protons near the carboxyl group reflect closest proximity to the αX I-domain-simvastatin binding interface as shown by highest degree of saturation. The methyl groups of simvastatin exhibited intermediate saturation intensities at farthest upfield frequency values between 0 and —1 ppm. The experiment was carried out at the molar ratio of 1:40 for the αX I-domain-simvastatin complex. The highest intensity saturation region is shown as an inset in 48B.

A.

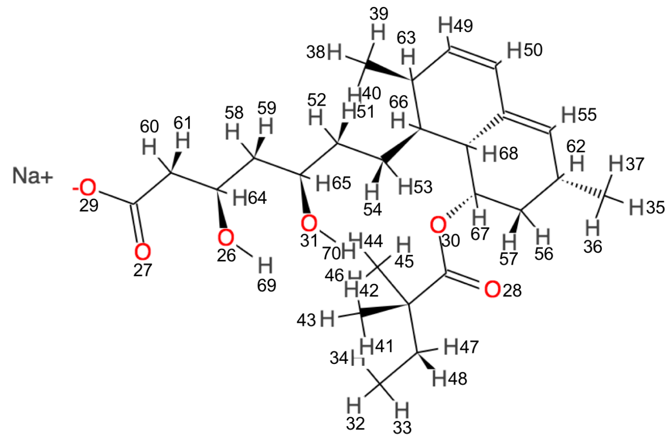
Na+
-O
29
O
27
O
26
H
69
O
31
70H
O
30
O28

B.

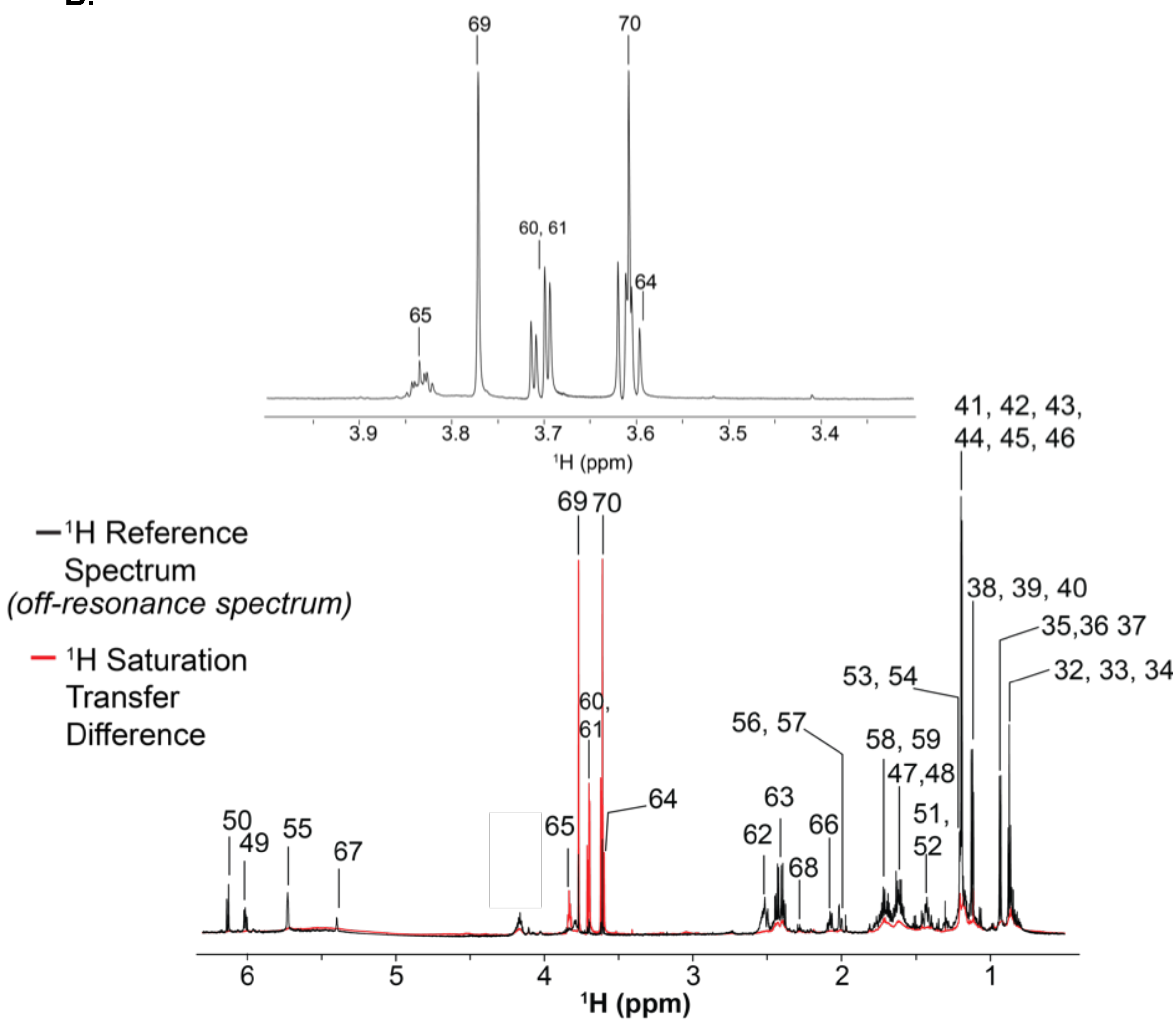
69
70
60, 61
65
64
3.9
3.8
3.7
3.6
3.5
3.4
¹H (ppm)
¹H Reference Spectrum
(off-resonance spectrum)
¹H Saturation Transfer Difference
69 70
60, 61
64
65
50
49
55
67
62
63
68
66
56, 57
53, 54
58, 59
47,48
51, 52
41, 42, 43, 44, 45, 46
38, 39, 40
35,36 37
32, 33, 34
6
5
4
3
2
1
¹H (ppm)

Table 16: Proton chemical shifts for lactone-ring and hydroxy-form simvastatin

Lactone Ring Simvastatin			Hydroxy Form Simvastatin			
Atom ID	**Chemical Shift**	**Ambiguity Code**	**Atom ID**	**Chemical Shift**	**Ambiguity Code**	**Identified Coupling**
H31	0.767	1	H32	0.871	1	t
H32	0.767	1	H33	0.871	1	t
H33	0.767	1	H34	0.871	1	t
H37	0.8408	1	H38	1.123	1	t
H38	0.8408	1	H39	1.123	1	t
H39	0.8408	1	H40	1.123	1	t
H34	1.0221	1	H35	0.935	1	d
H35	1.0221	1	H36	0.935	1	d
H36	1.0221	1	H37	0.935	1	d
H40	1.0567	1	H41	1.19	2	s
H41	1.0567	1	H42	1.19	2	s
H42	1.0567	1	H43	1.19	2	s
H43	1.0567	1	H44	1.197	2	s
H44	1.0567	1	H45	1.197	2	s
H45	1.0567	1	H46	1.197	2	s
H57	1.2696	4	H58	1.692	2	ddd
H50	1.2999	1	H51	1.43	2	td
H51	1.2999	1	H52	1.43	2	td
H46	1.4808	1	H47	1.595	2	
H47	1.4808	1	H48	1.627	2	
H65	1.5887	1	H66	2.081		
H52	1.6343	4	H53	1.204	2	d
H58	1.7029	4	H59	1.72	2	ddd
H53	1.7659	4	H54	1.204	2	d
H55	1.8208	4	H56	2.001	2	
H56	1.9716	4	H57	2.018	4	
H67	2.2994	1	H68	2.081	1	dd
H62	2.3605	1	H63	2.416	1	qdd
H59	2.3809	4	H60	3.697	2	d
H61	2.3969	1	H62	2.516	1	
H60	2.626	4	H61	3.711	2	d
H64	4.1021	1	H65	3.794	1	tt
H63	4.47	1	H64	4.163	1	tt
H66	5.2093	1	H67	5.396	1	dd
H54	5.5038	1	H55	5.727	1	
H48	5.782	1	H49	6,012	1	dd
H49	5.9647	1	H50	6.132	1	d
H68	3.549	1	H69	3.773	1	
			H70	3.61	1	

To further ascertain the molecules involved in simvastatin's interaction to the αX I-domain, molecular docking of simvastatin to the αX I-domain was carried out using the Glide docking tool of Schrödinger Induced Fit Docking program. Modeling of simvastatin-αX I-domain complex demonstrated that carboxylate moiety of simvastatin directly interacts with the Mg^{2+} and the surrounding residues, Thr 207, Ser 140, Ser 142, Glu 244 through hydrophilic interactions. The residues Phe 206, Gly 205, and Gly 141 exhibited hydrophobic interactions with the methyl groups of simvastatin (Figure 49A). This docking result depicting hydrophobic interactions was in agreement with our STD-NMR data. Interestingly, the carboxylate group of simvastatin interacting with Mg^{2+} was buried in the ligand-binding site and stabilized by hydrophilic interactions as I predicted in our STD study. This interaction site was further surrounded by the hydrophobic residues and stabilized by van der Waals interaction (Figure 49B).

In previous structural studies using X-ray crystallography by the Jensen group, simvastatin was also shown to bind to the αM I-domain, a sister homolog of the αX I-domain (107). The αX I-domain residues such as Phe 206, Thr 207, Gly 141 correspond to the residues-Arg 208, Thr 209, Gly 141 of the αM I-domain, respectively (Figures 49B, D).

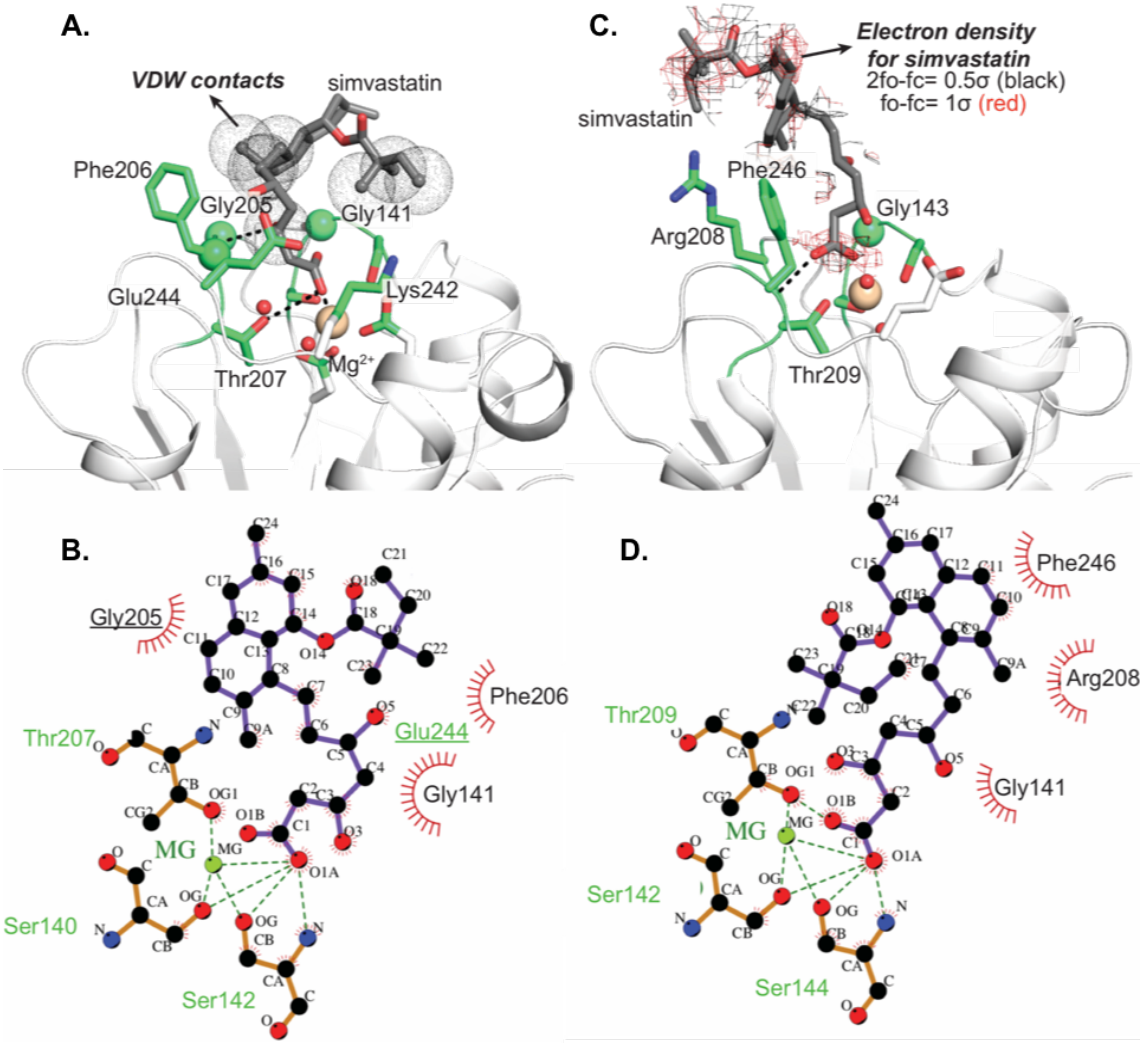

Figure 49: Molecular docking of simvastatin to the αI-domains reveal key amino acid interactions. (A, B) Molecular docking of simvastatin to the αX I-domain revealing that the carboxyl group of hydrolyzed simvastatin associates with Mg^{2+} at the MIDAS through hydrophilic interactions with Ser 140, Ser 142, Thr 207, and Glu 244 (shown in dotted lines), whereas the spiked red arcs represent the aromatic moiety of simvastatin interacts with Gly 141, Gly 205, and Phe 206 through hydrophobic interactions. **(C, D)** Molecular docking of simvastatin to the αM I-domain demonstrates that the negative electron density of simvastatin (shown in red mesh) potentially indicates that structural assignment of simvastatin in its crystal complex with the αM I-domain is possibly not be the best representation for demonstrating the molecular basis of simvastatin binding.
Molecular docking studies conducted and figure generated by Dr. Yanyun Liu (Briggs Lab).

Using density-difference maps, we evaluated the structural quality of the simvastatin-αM I-domain binding region. Two of the common ways to evaluate electron densities are by using F_0-F_c and $2F_0$-F_c density-difference maps.

F_0 is the observed structure factor amplitude that is used in calculating the direct experimental map. F_c is the structure factor calculated from a model (170). A positive density in the F_0-F_c map is observed in the areas where the model has missing atoms. A negative density in the F_0-F_c map is exhibited for the areas where the model contains atoms that should not be present. Therefore, the F_0-F_c density-difference map, typically contoured at (+) and (-) 3 σ, depicts where the experimental data and the model differ (171). In the $2F_0$-F_c density-difference map, the observed structure factor amplitudes are weighted heavily such that even the areas where the model and data agree will be covered by electron density. Therefore, the atoms that should not be at their current positions in the model will have little to no electron density, whereas the empty peaks mark positions where atoms must be added to the model to agree with the data (171).

In the crystal structure of the αM I-domain-simvastatin complex, the electron density of simvastatin is not properly formed in the crystal lattice. The F_0-F_c density-difference map indicated negative density (red mesh) for most moieties of simvastatin in the crystal structure model (Figure 49C) despite the reported high resolution of 2 Å. This implied that these constituents of simvastatin in the crystal complex were highly flexible and averaged out or even not present. In the $2F_0$-F_c difference density map, we observed little to no electron densities of simvastatin near the aromatic ring and hydrocarbon chain next to the carboxylic group, which indicated that these molecules were perhaps incorrectly positioned in the model. The αM I-domain-simvastatin complex

was determined by soaking the αM I-domain crystal in a 1 mM simvastatin solution and was not co-crystallized (107). Studies have reported that soaking of preformed crystal to simvastatin-containing crystallization liquor can have some disadvantages, such as the binding mode observed in a soaked structure may not accurately represent the solution binding mode, which is pertinent to any steric hindrance or protein conformational changes (172, 173).

Typically, the ligand-protein binding is stabilized by intermolecular forces. On comparing with the αX and αM I-domain-simvastatin complex obtained from molecular docking studies, the assigned molecular constituents in the αM I-domain-simvastatin crystal complex should likely be stabilized by hydrophobic and van der Waal's interactions (Figures 49A, C). An interesting observation was that the orientation of simvastatin-αX I-domain complex from our docking studies showed that the spatial arrangement differed from that of the simvastatin-αM I-domain complex; the decalin moiety was flipped horizontally thereby showing characteristics of a diastereomer (Fig. 49C, D).

4.2.3 Simvastatin decreases αX I-domain affinity to its natural ligand-iC3b.

To further characterize the effect of simvastatin, we conducted a SPR binding assay at varying concentrations of simvastatin. To the sensor chip immobilized with iC3b, 10 μM of the SILEN αX I-domain at different concentrations of simvastatin ranging from 0 to 500 μM were injected. We observed a progressive decrease in sensogram signal response with an increase in the simvastatin concentration (Figure 50A). This data demonstrated that simvastatin showed an antagonistic effect for binding of the

SILEN αX I-domain to its ligand- iC3b and its half-maximal inhibitory concentrations (IC_{50}) was determined to be 44.6 ± 8.5 μM (Figure 50B).

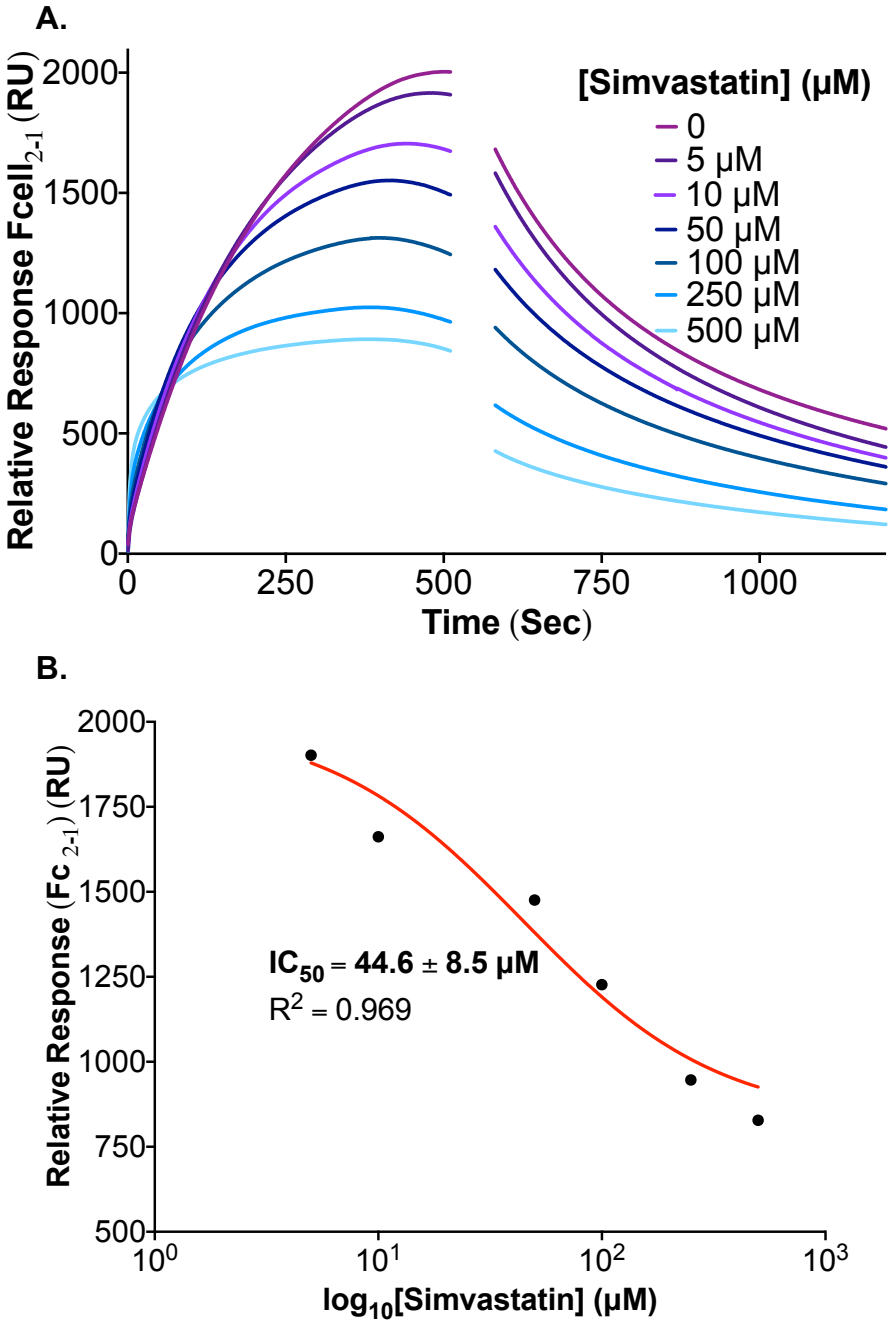

Figure 50: Simvastatin acts as an antagonist of the αX-I domain binding to the ligand, iC3b. (A) SPR binding assay demonstrated a decrease in the sensogram response for the SILEN αX I-domain with increasing simvastatin concentrations ranging from 0—500 μM. **(B)** Determination of the half-maximal inhibitory concentration (IC_{50}) of simvastatin to the SILEN αX I-domain binding to iC3b by plotting the relative sensogram response of the SILEN αX I-domain upon increment in simvastatin concentration.

In chapter 4, we demonstrated for the first time that simvastatin interacts with the αX I-domain with an affinity in the micromolar range. Our DSF and NMR studies reported the simvastatin affinity to the αX I-domain at K_D of 861± 22 μM and 202 ± 18 μM, respectively. From our STD-NMR and molecular docking studies, we elucidated the binding mode of interaction between simvastatin and the αX I-domain. Our molecular docking results depicted that the carboxylate moiety of simvastatin directly interacts with the Mg^{2+} and the surrounding residues have extensive hydrophobic interactions with the methyl groups of simvastatin. The evidence for these hydrophobic interactions was provided by observations in our STD-NMR studies in which the methyl groups of simvastatin exhibited saturation transfer. Subsequently, we showed that simvastatin antagonizes the αX I-domain binding to its ligand- iC3b with an IC_{50} of 44.6 ± 8.5 μM.

Integrins are known to interact with their ligand through an invariant negatively charged residue. The carboxylic group of simvastatin endows similar interaction for its binding to the αX I-domain. Therefore, our studies on the characterization of simvastatin interaction with the αX I-domain binding could provide advancement in understanding the molecular basis of interaction for the αX I-domain to its ligands and a platform to understand the basis behind differences observed among binding affinities of the αX I-domain to its multiple ligands.

4.3 Discussion

4.3.1 Molecular basis of simvastatin-the αX I-domain interaction.

Statins act as immunosuppressants independent of their cholesterol lowering abilities (108). Studies have reported that simvastatin affects the intraepithelial lymphocytes and lovastatin alters the leukocyte distribution in Peyer patches (109, 111).

These studies suggest that statins' contribution to the immunomodulatory effects is linked to the gut-associated secondary lymphoid tissues that respond to gut-derived antigen from food and microbes. The secondary lymphoid tissues support maturation of T cells and are the hub of adaptive immune responses wherein interactions between lymphocytes and antigen-bearing dendritic cells are facilitated. These myeloid dendritic cells express αXβ2 which assist in their migration and drain into the Peyer patches upon encountering the antigens (174). The αXβ2 antagonism could be one of the therapeutic strategies to regulate immune response. Therefore, we characterized the molecular basis of simvastatin binding to αXβ2 and its role in integrin conformational changes.

4.3.1.1 Simvastatin binds to the αX I-domain.

In our studies, we showed that simvastatin binds to the αX I-domain MIDAS with mid-micromolar range affinity. This finding agrees with the studies reporting lower micromolar range affinity for simvastatin binding the αM I-domain at the MIDAS motif as competitive antagonist (107) whereas simvastatin, lovastatin, and mevastatin binding to the distal site of αL I-domain as allosteric antagonists (110). We also identified that the hydroxy acid form of simvastatin actively binds to the αX I-domain through its carboxylate group.

The molecular modeling of simvastatin-αX I-domain complex showed the carboxylate moiety of simvastatin to directly interact with the Mg^{2+} and the surrounding residues at the αX I-domain MIDAS through hydrophilic interactions. This hydrophilic binding interaction was further buried by hydrophobic residues and stabilized by van der Waals interactions. In comparison, in the simvastatin-αM I-domain complex, the positively charged residue Arg 208 in the αM I-domain is present instead of the

hydrophobic residue Phe 206 in the αX I-domain (Figures 51A, B). On comparing the spatial arrangement of simvastatin-αX- and αM-I-domain complexes, the orientation of decalin moiety of simvastatin differed.

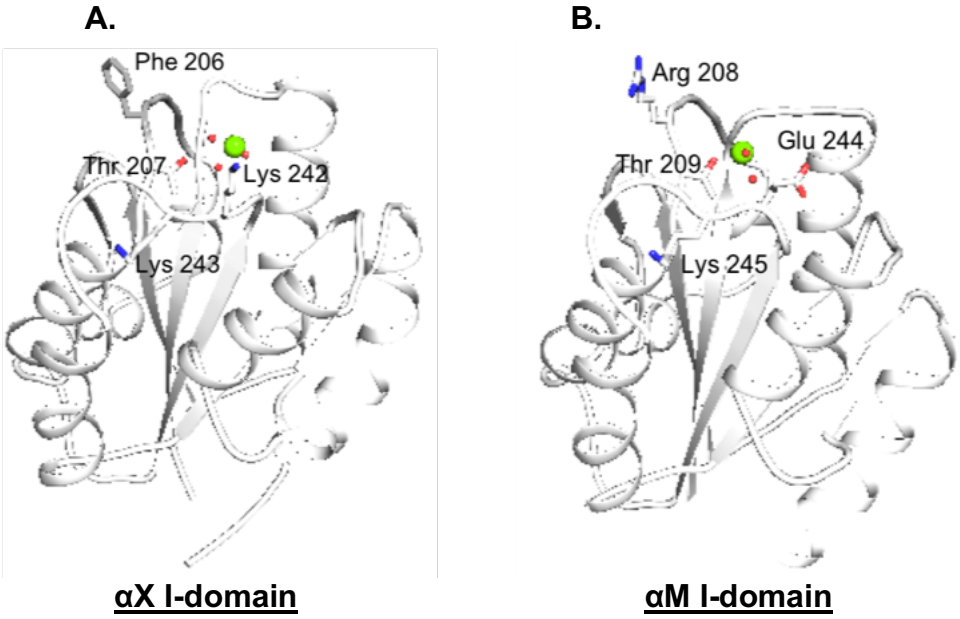

Figure 51: Crystal structures of the αX I-domain and the αM I-domain showing corresponding amino acid differences at MIDAS. (A) The hydrophobic residue-Phe 206 and positively charged residue-Lys 242 of the αX I-domain are substituted by the corresponding **(B)** positively charged residue-Arg 208 and negatively charged residue Glu 244, respectively, in the αM I-domain.

We identified that the simvastatin binding to the αX I-domain differed from that of the αM I-domain based on their differences in charge, hydrophobic properties, and spatial arrangement of binding. Despite high homology between the αX and αM I-domain, these differences in the mode of binding of simvastatin offers us a promising scaffold to design integrin-specific inhibitors in the future studies.

Studies have shown that the ligand affinity to integrins is highly favored by low dielectric environment propensity which validates the propensity of MIDAS motif to be buried in the hydrophobic core with hydrophobic residues surrounding the hydrophilic interactions of Mg^{2+} (175). Even though both αXβ2 and αMβ2 bind to negatively

charged molecules, considerable evidence has shown that only αMβ2 is inclined to bind cationic species as well such as myelin basic protein (MBP) (60), cathelicidin antimicrobial peptide LL-37 (176), pleiotrophin (61), and opioid peptide dynorphin A (62), all of which has overall positive charges.

The αX I-domain differs from the other αI-domains by a groove that contains positively charged residues running through the MIDAS. For example, in the αM I-domain, this positively charged groove is interrupted by the substitution of the αM-Glu 244 instead of the αX-Lys 242 residue (Figure 51A, B). These molecular properties could be beneficial in designing integrin-specific and potent derivatives of the simvastatin. For example, a lovastatin-based αLβ2 inhibitor called LFA703, a designed compound, that showed increased inhibitory activity of αLβ2 but did not affect the HMG-CoA reductase capability is a good example of development of second generation repurposed drug (110).

4.3.1.2 Simvastatin antagonizes the binding of the αX I-domain to its ligands.

Our affinity measurements showed that simvastatin antagonizes the binding of the αX I-domain to its natural ligand, iC3b at the half maximal inhibitory concentration (IC_{50}) of 44.5 μM in SPR assay and 62 μM in cell-based assay (performed by Zeinab Moussa from our lab). These findings agree with the study that identified simvastatin to interact with the αM I-domain and acted as an antagonist to αMβ2 binding to iC3b with an IC_{50} of 35 μM (107). The effectiveness of statins is dependent on their local concentration in the tissues. Two individual studies have reported that the plasma concentrations of statins are in the low nanomolar range (177, 178). However, statins are excessively degraded before being available in the blood, thereby leading to the

nanomolar plasma concentrations. These low concentrations of statins would not be effective since simvastatin's IC_{50} from our affinity studies along with cellular assays reported by other groups depict that statins' inhibitory role to integrins are observed only in the micromolar range (107, 110, 113).

One explanation to justify integrin's sensitivity to simvastatin inhibition is that statins reach the mucosal immune system before the liver or plasma (107). For instance, experimental evidence has shown that the concentration of rosuvastatin is ~500-fold higher in the bile than in plasma indicating that statins are possibly active in intestinal environment (179). The concentration of statins in the environment of intraepithelial leukocytes and vital lymphoid tissues is likely to be higher than in the blood plasma but requires further investigation.

Herein, using NMR techniques, molecular docking approach, and binding assays, we identified the first αXβ2 competitive antagonist, simvastatin, and characterized the molecular interactions of simvastatin with the αX I-domain. In summary, understanding the molecular basis of simvastatin interaction to the αX I-domain opens perspective of targeting the αX I-domain MIDAS motif by inhibitors structurally derived from simvastatin which can provide a platform to advance the development of selective and potent αXβ2 antagonists for autoimmune therapies.

4.4 Future Directions

4.4.1 Developing simvastatin-derived αXβ2 antagonists.

To identify the αXβ2 antagonist and determine the molecules of the αX-I domain involved in ligand-binding interactions, we conducted biophysical characterization by using NMR and molecular docking approaches. Structural and biophysical

characterization are important studies for understanding structural features of integrins and can provide insights in designing small molecule inhibitors or activators of β2-integrins. While our study paved a way for future studies on simvastatin-derived drug design to target αXβ2, further work is required to understand the integrin activation mechanism in light of allosteric structural changes occurring in integrin. The X-ray crystallography method has better application for stationary and rigid proteins, contrasting to the integrin's structural dynamic features. αXβ2-ligand interactions elucidated by negative EM images could provide structural information on the changes in the ligand binding interface of αXβ2. However, there is a concern that negative stain EM would introduce conformation bias to αXβ2-ligand complex formation since the sample preparation would involve heavy metal stain, absorbing on carbon film and dehydration (180). Intriguingly, mechanistic insights into integrin αVβ8 ligand specificity and TGF-β activation has been provided using single particle cryo-EM in which αVβ8 in its intermediate conformations of extended closed state was able to elicit integrin activation mechanisms (181). Therefore, for better authenticity, cryo-EM using phospholipid nanodiscs would be a remarkable approach for revealing binding interactions between αXβ2 and its ligands like fibrinogen, iC3b or small molecules in better resolution and closer to physiological condition on cell surface. This information would be valuable in guiding structure-based drug design of αXβ2 inhibitors or activators.

4.4.2 Study the effects of transition metals on the αX I-domain conformation and examine flexible regions of the αX I-domain.

In this study, we showed that the thermodynamics profile of the αX I-domain differs on binding to different cations- Mg^{2+}, Mn^{2+}, and Ca^{2+}. We specifically elucidated the Mg^{2+}-dependent structural changes occurring in the αX I-domain that progresses the αX I-domain to a ligand binding-competent state. Changes in integrin-ligand affinity have been observed as a function of cations like Mg^{2+}, Mn^{2+}, Ca^{2+}, and Zn^{2+} (138, 182-184). αI-domain crystal structures have also been observed in presence of Co^{2+}, Cd^{2+}, Ni^{2+}, and Zn^{2+} (185). It would be interesting to examine if the αX I-domain and then other αI-domains could bind different divalent cations (ITC and CD studies), if and how structural heterogeneity is introduced (SAXS) in solution and if these cations alter integrin affinity and conformation (SPR and cell based-assays). The side chain pH titration NMR studies could be used to directly determine if the pKa changes of the MIDAS aspartate residues occur in solution. In addition, the computational metadynamics metainference approach used for obtaining an ensemble of models for a structurally heterogenous system can be implemented to characterize the transition states of the αX I-domain observed in our SAXS and NMR studies.

The conformational flexibility of the integrin assumes a central role in the molecular mechanism of integrin-ligand interactions. The global and local conformational changes of the WT and SILEN αX-I domain, and αXβ2 can be analyzed in the presence and absence of Mg^{2+} and simvastatin, respectively, via hydrogen/ deuterium exchange (HDX) mass spectrometry and NMR-HDX. These approaches would allow monitoring of time-dependent exchange of labile hydrogens to the solvent

rich in deuterium to provide site-specific information on local stability and exploring the impact of slower timescale dynamic events. The mapping of the peptide fragments' shifts would elucidate the most flexible regions. NMR-HDX studies on the α1 I-domain of the collagen binding α1β1 integrin has shown that ligand-binding event was associated with significant conformational changes in the αC and α7 helices of α1 I-domain which in turn demonstrated the relationship between local destabilization and propensity of allosteric structural changes (186).

In the αI- and βI- domains, the α1- and α7- helices are mechanically working in concert in shifting MIDAS between the low-affinity to high-affinity I-domain state. Besides, the significant change in the α7-helix, a conserved phenylalanine residue in the αI-α1 helix has been shown to be critical in stabilizing the movement of β6-α7 loop and α7- helix on transitioning to higher ligand-affinity state (187). Notably, a unique β6-α7 loop conformation in αVβ8 has shown to facilitate movement of the α1 helix which is present at the ligand binding pocket of the β8 βI-domain (analogous to the αI-domain) to transition it to high affinity state but without coupling β6-α7 loop reshaping and the α7-helix pistoning that is generally observed in other integrins (188). It would be very interesting to investigate these site-specific changes in the αX I-domain which can help in discerning the allosteric mechanism involved in ligand binding of the αXβ2.

BIBLIOGRAPHY

1. Hynes RO. Integrins: bidirectional, allosteric signaling machines. Cell. 2002;110(6):673-87.

2. Abram CL, Lowell CA. The ins and outs of leukocyte integrin signaling. Annu Rev Immunol. 2009;27:339-62.

3. Kürzinger K, Reynolds T, Germain RN, Davignon D, Martz E, Springer TA. A novel lymphocyte function-associated antigen (LFA-1): cellular distribution, quantitative expression, and structure. J Immunol. 1981;127(2):596-602.

4. Hynes R. Relationships between fibronectin and the cytoskeleton. Cell Surf Rev. 1981;7:97-139.

5. Hynes RO. Fibronectin and its relation to cellular structure and behavior. Cell Biology of Extracellular Matrix. Springer US; 1981;17: 295-334.

6. Hynes RO, Yamada KM. Fibronectins: multifunctional modular glycoproteins. J Cell Biol. 1982;95(2):369-77.

7. Humphries MJ. Integrin structure. Biochem Soc Trans. 2000;28(4):311-39.

8. Takada Y, Ye X, Simon S. The integrins. Genome Biol. 2007;8(5):215.

9. Bouvard D, Pouwels J, De Franceschi N, Ivaska J. Integrin inactivators: balancing cellular functions in vitro and in vivo. Nat Rev Mol Cell Biol. 2013;14(7):430-42.

10. Ginsberg MH, Partridge A, Shattil SJ. Integrin regulation. Curr Opin Cell Biol. 2005;17(5):509-16.

11. Arnaout MA, Mahalingam B, Xiong JP. Integrin structure, allostery, and bidirectional signaling. Annu Rev Cell Dev Biol. 2005;21:381-410.

12. Miyazaki N, Iwasaki K, Takagi J. A systematic survey of conformational states in β1 and β4 integrins using negative-stain electron microscopy. J Cell Sci. 2018;131(10):216754.

13. Mitroulis I, Alexaki VI, Kourtzelis I, Ziogas A, Hajishengallis G, Chavakis T. Leukocyte integrins: role in leukocyte recruitment and as therapeutic targets in inflammatory disease. Pharmacol Ther. 2015;147:123-35.

14. Luo BH, Carman CV, Springer TA. Structural basis of integrin regulation and signaling. Annu Rev Immunol. 2007;25:619-47.

15. Bednarczyk M, Stege H, Grabbe S, Bros M. β2 Integrins-multi-functional leukocyte receptors in health and disease. Int J Mol Sci. 2020;21(4):1402.

16. Fagerholm SC, Guenther C, Llort Asens M, Savinko T, Uotila LM. Beta2-integrins and interacting proteins in leukocyte trafficking, immune suppression, and immunodeficiency disease. Front Immunol. 2019;10:254.

17. Tan SM. The leucocyte β2 (CD18) integrins: the structure, functional regulation and signalling properties. Biosci Rep. 2012;32(3):241-69.

18. Schittenhelm L, Hilkens CM, Morrison VL. β(2) Integrins as regulators of dendritic cell, monocyte, and macrophage function. Front Immunol. 2017;8:1866.

19. Venet F, Monneret G. Advances in the understanding and treatment of sepsis-induced immunosuppression. Nat Rev Nephrol. 2018;14(2):121-37.

20. Brinkman CC, Rouhani SJ, Srinivasan N, Engelhard VH. Peripheral tissue homing receptors enable T cell entry into lymph nodes and affect the anatomical distribution of memory cells. J Immunol. 2013;191(5):2412-25.

21. Farstad IN, Halstensen TS, Kvale D, Fausa O, Brandtzaeg P. Topographic distribution of homing receptors on B and T cells in human gut-associated lymphoid tissue: relation of L-selectin and integrin alpha 4 beta 7 to naive and memory phenotypes. Am J Pathol. 1997;150(1):187-99.

22. Gorfu G, Rivera-Nieves J, Ley K. Role of beta7 integrins in intestinal lymphocyte homing and retention. Curr Mol Med. 2009;9(7):836-50.

23. Hu X, Wohler JE, Dugger KJ, Barnum SR. Beta2-integrins in demyelinating disease: not adhering to the paradigm. J Leukoc Biol. 2010;87(3):397-403.

24. Dustin ML. Cell adhesion molecules and actin cytoskeleton at immune synapses and kinapses. Curr Opin Cell Biol. 2007;19(5):529-33.

25. Carrasco YR, Fleire SJ, Cameron T, Dustin ML, Batista FD. LFA-1/ICAM-1 Interaction lowers the threshold of B cell activation by facilitating B cell adhesion and synapse formation. Immunity. 2004;20(5):589-99.

26. Osman MS, Burshtyn DN, Kane KP. Activating Ly-49 Receptors regulate LFA-1-mediated adhesion by NK cells. J Immunol. 2007;178(3):1261-7.

27. Fischer A, Lisowska-Grospierre B, Anderson DC, Springer TA. Leukocyte adhesion deficiency: molecular basis and functional consequences. Immunodefic Rev. 1988;1(1):39-54.

28. Nath SK, Han S, Kim-Howard X, Kelly JA, Viswanathan P, Gilkeson GS, et al. A nonsynonymous functional variant in integrin-alpha(M) (encoded by ITGAM) is associated with systemic lupus erythematosus. Nat Genet. 2008;40(2):152-4.

29. Kuijpers TW, Van Lier RA, Hamann D, de Boer M, Thung LY, Weening RS, et al. Leukocyte adhesion deficiency type 1 (LAD-1)/variant: a novel immunodeficiency syndrome characterized by dysfunctional beta2 integrins. J Clin Invest. 1997;100(7):1725-33.

30. Mathew EC, Shaw JM, Bonilla FA, Law SK, Wright DA. A novel point mutation in CD18 causing the expression of dysfunctional CD11/CD18 leucocyte integrins in a patient with leucocyte adhesion deficiency (LAD). Clin Exp Immunol. 2000;121(1):133-8.

31. Bunting M, Harris ES, McIntyre TM, Prescott SM, Zimmerman GA. Leukocyte adhesion deficiency syndromes: adhesion and tethering defects involving beta 2 integrins and selectin ligands. Curr Opin Hematol. 2002;9(1):30-5.

32. Hom G, Graham RR, Modrek B, Taylor KE, Ortmann W, Garnier S, et al. Association of systemic lupus erythematosus with C8orf13-BLK and ITGAM-ITGAX. N Engl J Med. 2008;358(9):900-9.

33. Harley JB, Alarcón-Riquelme ME, Criswell LA, Jacob CO, Kimberly RP, Moser KL, et al. Genome-wide association scan in women with systemic lupus erythematosus identifies susceptibility variants in ITGAM, PXK, KIAA1542 and other loci. Nat Genet. 2008;40(2):204-10.

34. Keizer GD, Te Velde AA, Schwarting R, Figdor CG, De Vries JE. Role of p150,95 in adhesion, migration, chemotaxis and phagocytosis of human monocytes. Eur J Immunol. 1987;17(9):1317-22.

35. Metlay JP, Witmer-Pack MD, Agger R, Crowley MT, Lawless D, Steinman RM. The distinct leukocyte integrins of mouse spleen dendritic cells as identified with new hamster monoclonal antibodies. J Exp Med. 1990;171(5):1753-71.

36. Bilsland CA, Diamond MS, Springer TA. The leukocyte integrin p150,95 (CD11c/CD18) as a receptor for iC3b. Activation by a heterologous beta subunit and localization of a ligand recognition site to the I domain. J Immunol. 1994;152(9):4582-9.

37. Wu H, Gower RM, Wang H, Perrard XY, Ma R, Bullard DC, et al. Functional role of CD11c+ monocytes in atherogenesis associated with hypercholesterolemia. Circulation. 2009;119(20):2708-17.

38. Galon J, Gauchat JF, Mazières N, Spagnoli R, Storkus W, Lötze M, et al. Soluble Fcgamma receptor type III (FcgammaRIII, CD16) triggers cell activation through interaction with complement receptors. J Immunol. 1996;157(3):1184-92.

39. Loike JD, Sodeik B, Cao L, Leucona S, Weitz JI, Detmers PA, et al. CD11c/CD18 on neutrophils recognizes a domain at the N terminus of the A alpha chain of fibrinogen. Proc Natl Acad Sci U S A. 1991;88(3):1044-8.

40. Garnotel R, Rittié L, Poitevin S, Monboisse JC, Nguyen P, Potron G, et al. Human blood monocytes interact with type I collagen through alpha x beta 2 integrin (CD11c-CD18, gp150-95). J Immunol. 2000;164(11):5928-34.

41. Blackford J, Reid HW, Pappin DJ, Bowers FS, Wilkinson JM. A monoclonal antibody, 3/22, to rabbit CD11c which induces homotypic T cell aggregation: evidence that ICAM-1 is a ligand for CD11c/CD18. Eur J Immunol. 1996;26(3):525-31.

42. Sadhu C, Ting HJ, Lipsky B, Hensley K, Garcia-Martinez LF, Simon SI, et al. CD11c/CD18: novel ligands and a role in delayed-type hypersensitivity. J Leukoc Biol. 2007;81(6):1395-403.

43. Ihanus E, Uotila LM, Toivanen A, Varis M, Gahmberg CG. Red-cell ICAM-4 is a ligand for the monocyte/macrophage integrin CD11c/CD18: characterization of the binding sites on ICAM-4. Blood. 2007;109(2):802-10.

44. Vorup-Jensen T, Chi L, Gjelstrup LC, Jensen UB, Jewett CA, Xie C, et al. Binding between the integrin alphaXbeta2 (CD11c/CD18) and heparin. J Biol Chem. 2007;282(42):30869-77.

45. Davis GE. The Mac-1 and p150,95 beta 2 integrins bind denatured proteins to mediate leukocyte cell-substrate adhesion. Exp Cell Res. 1992;200(2):242-52.

46. Vorup-Jensen T, Carman CV, Shimaoka M, Schuck P, Svitel J, Springer TA. Exposure of acidic residues as a danger signal for recognition of fibrinogen and other macromolecules by integrin alphaXbeta2. Proc Natl Acad Sci U S A. 2005;102(5):1614-9.

47. Xu S, Wang J, Wang JH, Springer TA. Distinct recognition of complement iC3b by integrins αXβ2 and αMβ2. Proc Natl Acad Sci U S A. 2017;114(13):3403-8.

48. Chen X, Yu Y, Mi LZ, Walz T, Springer TA. Molecular basis for complement recognition by integrin αXβ2. Proc Natl Acad Sci U S A. 2012;109(12):4586-91.

49. Papanastasiou M, Koutsogiannaki S, Sarigiannis Y, Geisbrecht BV, Ricklin D, Lambris JD. Structural implications for the formation and function of the complement effector protein iC3b. J Immunol. 2017;198(8):3326-35.

50. Ricklin D, Hajishengallis G, Yang K, Lambris JD. Complement: a key system for immune surveillance and homeostasis. Nat Immunol. 2010;11(9):785-97.

51. Jensen RK, Bajic G, Sen M, Springer TA, Vorup-Jensen T, Andersen GR. Complement receptor 3 forms a compact high affinity complex with iC3b. bioRxiv. 2020:2020.04.15.043133.

52. Choi J, Buyannemekh D, Nham SU. Moieties of Complement iC3b Recognized by the I-domain of Integrin αXβ2. Mol Cells. 2020;43(12):1023-34.

53. Nham SU. Characteristics of fibrinogen binding to the domain of CD11c, an alpha subunit of p150,95. Biochem Biophys Res Commun. 1999;264(3):630-4.
54. Choi J, Nham SU. Loops within the CD11c I domain critical for specific recognition of fibrinogen. Biochem Biophys Res Commun. 2002;292(3):756-60.

55. Lishko VK, Podolnikova NP, Yakubenko VP, Yakovlev S, Medved L, Yadav SP, et al. Multiple binding sites in fibrinogen for integrin alphaMbeta2 (Mac-1). J Biol Chem. 2004;279(43):44897-906.

56. Lukácsi S, Gerecsei T, Balázs K, Francz B, Szabó B, Erdei A, et al. The differential role of CR3 (CD11b/CD18) and CR4 (CD11c/CD18) in the adherence, migration and podosome formation of human macrophages and dendritic cells under inflammatory conditions. PLoS One. 2020;15(5):232432.

57. Hogg N, Takacs L, Palmer DG, Selvendran Y, Allen C. The p150,95 molecule is a marker of human mononuclear phagocytes: comparison with expression of class II molecules. Eur J Immunol. 1986;16(3):240-8.

58. Gahmberg CG, Tolvanen M, Kotovuori P. Leukocyte adhesion--structure and function of human leukocyte beta2-integrins and their cellular ligands. Eur J Biochem. 1997;245(2):215-32.

59. Lu C, Ferzly M, Takagi J, Springer TA. Epitope mapping of antibodies to the C-terminal region of the integrin beta 2 subunit reveals regions that become exposed upon receptor activation. J Immunol. 2001;166(9):5629-37.

60. Stapulionis R, Oliveira CL, Gjelstrup MC, Pedersen JS, Hokland ME, Hoffmann SV, et al. Structural insight into the function of myelin basic protein as a ligand for integrin alpha M beta 2. J Immunol. 2008;180(6):3946-56.

61. Shen D, Podolnikova NP, Yakubenko VP, Ardell CL, Balabiyev A, Ugarova TP, et al. Pleiotrophin, a multifunctional cytokine and growth factor, induces leukocyte responses through the integrin Mac-1. J Biol Chem. 2017;292(46):18848-61.

62. Podolnikova NP, Brothwell JA, Ugarova TP. The opioid peptide dynorphin A induces leukocyte responses via integrin Mac-1 (αMβ2, CD11b/CD18). Mol Pain. 2015;11:33.

63. Vorup-Jensen T, Jensen RK. Structural immunology of complement receptors 3 and 4. Front Immunol. 2018; 9:2716.

64. Jawhara S, Pluskota E, Cao W, Plow EF, Soloviev DA. Distinct effects of integrins αXβ2 and αMβ2 on leukocyte subpopulations during inflammation and antimicrobial responses. Infect Immun. 2017;85(1):644-56.

65. Bajic G, Yatime L, Sim RB, Vorup-Jensen T, Andersen GR. Structural insight on the recognition of surface-bound opsonins by the integrin I domain of complement receptor 3. Proc Natl Acad Sci U S A. 2013;110(41):16426-31.
66. Jawhara S, Pluskota E, Verbovetskiy D, Skomorovska-Prokvolit O, Plow EF, Soloviev DA. Integrin αXβ2 is a leukocyte receptor for Candida albicans and is essential for protection against fungal infections. J Immunol. 2012;189(5):2468-77.

67. Tacke F, Alvarez D, Kaplan TJ, Jakubzick C, Spanbroek R, Llodra J, et al. Monocyte subsets differentially employ CCR2, CCR5, and CX3CR1 to accumulate within atherosclerotic plaques. J Clin Invest. 2007;117(1):185-94.

68. Campbell ID, Humphries MJ. Integrin structure, activation, and interactions. Cold Spring Harb Perspect Biol. 2011;3(3):4994.

69. Arnaout MA, Goodman SL, Xiong JP. Structure and mechanics of integrin-based cell adhesion. Curr Opin Cell Biol. 2007;19(5):495-507.

70. Manandhar P, Abousaway O, Le T, Sen M. Role of structural dynamics in leukocyte integrins function: interplay between the shape-shifting mechanism and allostery. Int J Cell Sci & Mol Biol. 2017; 3(4): 555617.

71. Li R, Bennett JS, Degrado WF. Structural basis for integrin alphaIIbbeta3 clustering. Biochem Soc Trans. 2004;32(Pt3):412-5.

72. Luo BH, Springer TA, Takagi J. A specific interface between integrin transmembrane helices and affinity for ligand. PLoS Biol. 2004;2(6):776-86.

73. Lau TL, Dua V, Ulmer TS. Structure of the integrin alphaIIb transmembrane segment. J Biol Chem. 2008;283(23):16162-8.

74. Adair BD, Yeager M. Three-dimensional model of the human platelet integrin alpha IIb beta 3 based on electron cryomicroscopy and x-ray crystallography. Proc Natl Acad Sci U S A. 2002;99(22):14059-64.

75. Vinogradova O, Haas T, Plow EF, Qin J. A structural basis for integrin activation by the cytoplasmic tail of the alpha IIb-subunit. Proc Natl Acad Sci U S A. 2000;97(4):1450-5.

76. Xiong JP, Stehle T, Diefenbach B, Zhang R, Dunker R, Scott DL, et al. Crystal structure of the extracellular segment of integrin alphaV beta3. Science. 2001;294(5541):339-45.

77. Zhu J, Luo BH, Xiao T, Zhang C, Nishida N, Springer TA. Structure of a complete integrin ectodomain in a physiologic resting state and activation and deactivation by applied forces. Mol Cell. 2008;32(6):849-61.

78. Sen M, Springer TA. Leukocyte integrin αLβ2 headpiece structures: the αI domain, the pocket for the internal ligand, and concerted movements of its loops. Proc Natl Acad Sci U S A. 2016;113(11):2940-5.

79. Sen M, Yuki K, Springer TA. An internal ligand-bound, metastable state of a leukocyte integrin, αXβ2. J Cell Biol. 2013;203(4):629-42.

80. Larson RS, Corbi AL, Berman L, Springer T. Primary structure of the leukocyte function-associated molecule-1 alpha subunit: an integrin with an embedded domain defining a protein superfamily. J Cell Biol. 1989;108(2):703-12.

81. Schürpf T, Springer TA. Regulation of integrin affinity on cell surfaces. Embo J. 2011;30(23):4712-27.

82. Xiao T, Takagi J, Coller BS, Wang JH, Springer TA. Structural basis for allostery in integrins and binding to fibrinogen-mimetic therapeutics. Nature. 2004;432(7013):59-67.

83. McCleverty CJ, Liddington RC. Engineered allosteric mutants of the integrin alphaMbeta2 I domain: structural and functional studies. Biochem J. 2003;372(Pt 1):121-7.

84. Takagi J, Petre BM, Walz T, Springer TA. Global conformational rearrangements in integrin extracellular domains in outside-in and inside-out signaling. Cell. 2002;110(5):599-11.

85. Nishida N, Xie C, Shimaoka M, Cheng Y, Walz T, Springer TA. Activation of leukocyte beta2 integrins by conversion from bent to extended conformations. Immunity. 2006;25(4):583-94.

86. Springer TA, Dustin ML. Integrin inside-out signaling and the immunological synapse. Curr Opin Cell Biol. 2012;24(1):107-15.

87. Shimaoka M, Xiao T, Liu JH, Yang Y, Dong Y, Jun CD, et al. Structures of the alpha L I domain and its complex with ICAM-1 reveal a shape-shifting pathway for integrin regulation. Cell. 2003;112(1):99-111.

88. Wolfenson H, Lavelin I, Geiger B. Dynamic regulation of the structure and functions of integrin adhesions. Dev Cell. 2013;24(5):447-58.

89. Askari JA, Buckley PA, Mould AP, Humphries MJ. Linking integrin conformation to function. J Cell Sci. 2009;122(Pt 2):165-70.

90. Liddington RC. Structural aspects of integrins. Adv Exp Med Biol. 2014;819:111-26.

91. Bachmann M, Kukkurainen S, Hytönen VP, Wehrle-Haller B. Cell Adhesion by integrins. Physiol Rev. 2019;99(4):1655-99.

92. Kaplan ZS, Jackson SP. The role of platelets in atherothrombosis. Hematology Am Soc Hematol Educ Program. 2011;2011:51-61.

93. Stoll G, Kleinschnitz C, Nieswandt B. Molecular mechanisms of thrombus formation in ischemic stroke: novel insights and targets for treatment. Blood. 2008;112(9):3555-62.

94. Frijns CJ, Kappelle LJ. Inflammatory cell adhesion molecules in ischemic cerebrovascular disease. Stroke. 2002;33(8):2115-22.

95. Rosenkranz AR, Mayadas TN. Leukocyte-endothelial cell interactions - lessons from knockout mice. Exp Nephrol. 1999;7(2):125-36.

96. Carter WG, Kaur P, Gil SG, Gahr PJ, Wayner EA. Distinct functions for integrins alpha 3 beta 1 in focal adhesions and alpha 6 beta 4/bullous pemphigoid antigen in a new stable anchoring contact (SAC) of keratinocytes: relation to hemidesmosomes. J Cell Biol. 1990;111(6 Pt 2):3141-54.

97. Hodivala-Dilke KM, DiPersio CM, Kreidberg JA, Hynes RO. Novel roles for alpha3beta1 integrin as a regulator of cytoskeletal assembly and as a trans-dominant inhibitor of integrin receptor function in mouse keratinocytes. J Cell Biol. 1998;142(5):1357-69.

98. Fan Z, Kiosses WB, Sun H, Orecchioni M, Ghosheh Y, Zajonc DM, et al. High-affinity bent β2-integrin molecules in arresting neutrophils face each other through binding to ICAMs in cis. Cell Rep. 2019;26(1):119-30.

99. Saggu G, Okubo K, Chen Y, Vattepu R, Tsuboi N, Rosetti F, et al. Cis interaction between sialylated FcγRIIA and the αI-domain of Mac-1 limits antibody-mediated neutrophil recruitment. Nat Commun. 2018;9(1):5058.

100. Alon R, Dustin ML. Force as a facilitator of integrin conformational changes during leukocyte arrest on blood vessels and antigen-presenting cells. Immunity. 2007;26(1):17-27.

101. Zwartz GJ, Chigaev A, Dwyer DC, Foutz TD, Edwards BS, Sklar LA. Real-time analysis of very late antigen-4 affinity modulation by shear. J Biol Chem. 2004;279(37):38277-86.

102. Astrof NS, Salas A, Shimaoka M, Chen J, Springer TA. Importance of force linkage in mechanochemistry of adhesion receptors. Biochemistry. 2006;45(50):15020-8.

103. Vorup-Jensen T, Ostermeier C, Shimaoka M, Hommel U, Springer TA. Structure and allosteric regulation of the alpha X beta 2 integrin I domain. Proc Natl Acad Sci U S A. 2003;100(4):1873-8.

104. Legge GB, Kriwacki RW, Chung J, Hommel U, Ramage P, Case DA, et al. NMR solution structure of the inserted domain of human leukocyte function associated antigen-1. J Mol Biol. 2000;295(5):1251-64.

105. Sen M, Koksal AC, Yuki K, Wang J, Springer TA. Ligand- and cation-induced structural alterations of the leukocyte integrin LFA-1. J Biol Chem. 2018;293(17):6565-77.

106. Xiong JP, Li R, Essafi M, Stehle T, Arnaout MA. An isoleucine-based allosteric switch controls affinity and shape shifting in integrin CD11b A-domain. J Biol Chem. 2000;275(49):38762-7.

107. Jensen MR, Bajic G, Zhang X, Laustsen AK, Koldsø H, Skeby KK, et al. Structural basis for simvastatin competitive antagonism of complement receptor 3. J Biol Chem. 2016;291(33):16963-76.

108. Jain MK, Ridker PM. Anti-inflammatory effects of statins: clinical evidence and basic mechanisms. Nat Rev Drug Discov. 2005;4(12):977-87.

109. Wang Y, Li D, Jones D, Bassett R, Sale GE, Khalili J, et al. Blocking LFA-1 activation with lovastatin prevents graft-versus-host disease in mouse bone marrow transplantation. Biol Blood Marrow Transplant. 2009;15(12):1513-22.

110. Weitz-Schmidt G, Welzenbach K, Brinkmann V, Kamata T, Kallen J, Bruns C, et al. Statins selectively inhibit leukocyte function antigen-1 by binding to a novel regulatory integrin site. Nat Med. 2001;7(6):687-92.

111. Zhang J, Osawa S, Takayanagi Y, Ikuma M, Yamada T, Sugimoto M, et al. Statins directly suppress cytokine production in murine intraepithelial lymphocytes. Cytokine. 2013;61(2):540-5.

112. Shimaoka M, Springer TA. Therapeutic antagonists and conformational regulation of integrin function. Nat Rev Drug Discov. 2003;2(9):703-16.

113. Kallen J, Welzenbach K, Ramage P, Geyl D, Kriwacki R, Legge G, et al. Structural basis for LFA-1 inhibition upon lovastatin binding to the CD11a I-domain. J Mol Biol. 1999;292(1):1-9.

114. Lehto J, Paajanen A, Harjula R, Leinonen H. Hydrolysis and H^+Na^+ exchange by chelex 100 chelating resin. Reactive Polymers. 1994;23(2):135-40.

115. Wright TA, Stewart JM, Page RC, Konkolewicz D. Extraction of thermodynamic parameters of protein unfolding using parallelized differential scanning fluorimetry. J Phys Chem Lett. 2017;8(3):553-8.

116. Sreerama N, Woody RW. Estimation of protein secondary structure from circular dichroism spectra: comparison of CONTIN, SELCON, and CDSSTR methods with an expanded reference set. Anal Biochem. 2000;287(2):252-60.

117. Zhao H, Gorshkova II, Fu GL, Schuck P. A comparison of binding surfaces for SPR biosensing using an antibody–antigen system and affinity distribution analysis. Methods. 2013;59(3):328-35.

118. Svitel J, Balbo A, Mariuzza RA, Gonzales NR, Schuck P. Combined affinity and rate constant distributions of ligand populations from experimental surface binding kinetics and equilibria. Biophys J. 2003;84(6):4062-77.

119. Svitel J, Boukari H, Van Ryk D, Willson RC, Schuck P. Probing the functional heterogeneity of surface binding sites by analysis of experimental binding traces and the effect of mass transport limitation. Biophys J. 2007;92(5):1742-58.

120. Li J, Springer TA. Integrin extension enables ultrasensitive regulation by cytoskeletal force. Proc Natl Acad Sci U S A. 2017;114(18):4685-90.

121. Lee JO, Bankston LA, Arnaout MA, Liddington RC. Two conformations of the integrin A-domain (I-domain): a pathway for activation? Structure. 1995;3(12):1333-40.

122. Lu C, Shimaoka M, Ferzly M, Oxvig C, Takagi J, Springer TA. An isolated, surface-expressed I domain of the integrin alphaL beta2 is sufficient for strong adhesive function when locked in the open conformation with a disulfide bond. Proc Natl Acad Sci U S A. 2001;98(5):2387-92.

123. Shimaoka M, Lu C, Palframan RT, von Andrian UH, McCormack A, Takagi J, et al. Reversibly locking a protein fold in an active conformation with a disulfide bond: integrin alphaL I domains with high affinity and antagonist activity in vivo. Proc Natl Acad Sci U S A. 2001;98(11):6009-14.

124. Li J, Springer TA. Energy landscape differences among integrins establish the framework for understanding activation. J Cell Biol. 2018;217(1):397-412.

125. Velázquez-Campoy A, Ohtaka H, Nezami A, Muzammil S, Freire E. Isothermal titration calorimetry. Curr Protoc Cell Biol. 2004;Chapter 17:Unit 17.8.

126. Johnson CM. Differential scanning calorimetry as a tool for protein folding and stability. Arch Biochem Biophys. 2013;531(1-2):100-9.

127. Niesen FH, Berglund H, Vedadi M. The use of differential scanning fluorimetry to detect ligand interactions that promote protein stability. Nat Protoc. 2007;2(9):2212-21.

128. Greenfield NJ. Using circular dichroism spectra to estimate protein secondary structure. Nat Protoc. 2007;1(6):2876-90.

129. Yao H, Wynendaele E, Xu X, Kosgei A, De Spiegeleer B. Circular dichroism in functional quality evaluation of medicines. J Pharm Biomed Anal. 2018;147:50-64.

130. Kikhney AG, Svergun DI. A practical guide to small angle X-ray scattering (SAXS) of flexible and intrinsically disordered proteins. FEBS Lett. 2015;589(19 Pt A):2570-7.

131. Grant TD, Luft JR, Carter LG, Matsui T, Weiss TM, Martel A, et al. The accurate assessment of small-angle X-ray scattering data. Acta Crystallogr D Biol Crystallogr. 2015;71(Pt 1):45-56.

132. Putnam CD, Hammel M, Hura GL, Tainer JA. X-ray solution scattering (SAXS) combined with crystallography and computation: defining accurate macromolecular structures, conformations and assemblies in solution. Q Rev Biophys. 2007;40(3):191-285.

133. Day ES, Capili AD, Borysenko CW, Zafari M, Whitty A. Determining the affinity and stoichiometry of interactions between unmodified proteins in solution using Biacore. Anal Biochem. 2013;440(1):96-107.

134. Gorshkova, II, Svitel J, Razjouyan F, Schuck P. Bayesian analysis of heterogeneity in the distribution of binding properties of immobilized surface sites. Langmuir. 2008;24(20):11577-86.

135. Ali V, Prakash K, Kulkarni S, Ahmad A, Madhusudan KP, Bhakuni V. 8-anilino-1-naphthalene sulfonic acid (ANS) induces folding of acid unfolded cytochrome c to molten globule state as a result of electrostatic interactions. Biochemistry. 1999;38(41):13635-42.

136. Zhou HX, Pang X. Electrostatic interactions in protein structure, folding, binding, and condensation. Chem Rev. 2018;118(4):1691-741.

137. Vorup-Jensen T. Surface plasmon resonance biosensing in studies of the binding between β_2 integrin I domains and their ligands. Methods Mol Biol. 2012;757:55-71.

138. Vorup-Jensen T, Waldron TT, Astrof N, Shimaoka M, Springer TA. The connection between metal ion affinity and ligand affinity in integrin I domains. Biochim Biophys Acta. 2007;1774(9):1148-55.

139. Ajroud K, Sugimori T, Goldmann WH, Fathallah DM, Xiong JP, Arnaout MA. Binding affinity of metal ions to the CD11b A-domain is regulated by integrin activation and ligands. J Biol Chem. 2004;279(24):25483-8.

140. Allred AL. Electronegativity values from thermochemical data. J Inorg Nucl Chem. 1961;17(3):215-21.

141. Lee KH, Xie D, Freire E, Amzel LM. Estimation of changes in side chain configurational entropy in binding and folding: general methods and application to helix formation. Proteins. 1994;20(1):68-84.

142. Brady GP, Sharp KA. Entropy in protein folding and in protein-protein interactions. Curr Opin Struct Biol. 1997;7(2):215-21.

143. Dahanayake JN, Mitchell-Koch KR. How does solvation layer mobility affect protein structural dynamics? Front Mol Biosci. 2018;5(65):1-20.

144. Habermann SM, Murphy KP. Energetics of hydrogen bonding in proteins: a model compound study. Protein Sci. 1996;5(7):1229-39.

145. Haider K, Wickstrom L, Ramsey S, Gilson MK, Kurtzman T. Enthalpic breakdown of water structure on protein active-site surfaces. J Phys Chem B. 2016;120(34):8743-56.

146. Pace CN, Grimsley GR, Scholtz JM. Protein ionizable groups: pK values and their contribution to protein stability and solubility. J Biol Chem. 2009;284(20):13285-9.

147. Hofer F, Kraml J, Kahler U, Kamenik AS, Liedl KR. Catalytic Site pK(a) values of aspartic, cysteine, and serine proteases: constant pH MD simulations. J Chem Inf Model. 2020;60(6):3030-42.

148. Rinaldo D, Field MJ. A computational study of the open and closed forms of the N-lobe human serum transferrin apoprotein. Biophys J. 2003;85(6):3485-501.

149. Vestergaard B. Analysis of biostructural changes, dynamics, and interactions - small-angle X-ray scattering to the rescue. Arch Biochem Biophys. 2016;602:69-79.

150. Lee JO, Rieu P, Arnaout MA, Liddington R. Crystal structure of the A domain from the alpha subunit of integrin CR3 (CD11b/CD18). Cell. 1995;80(4):631-8.

151. Schittenhelm L, Robertson J, Pratt AG, Hilkens CM, Morrison VL. Dendritic cell integrin expression patterns regulate inflammation in the rheumatoid arthritis joint. Rheumatology (Oxford). 2020;30:686.

152. Thorp E, Subramanian M, Tabas I. The role of macrophages and dendritic cells in the clearance of apoptotic cells in advanced atherosclerosis. Eur J Immunol. 2011;41(9):2515-8.

153. te Velde AA, Keizer GD, Figdor CG. Differential function of LFA-1 family molecules (CD11 and CD18) in adhesion of human monocytes to melanoma and endothelial cells. Immunology. 1987;61(3):261-7.

154. Papp KA. Efalizumab: Advancing psoriasis management with a novel, targeted T-cell modulator. Drugs Today (Barc). 2004;40(11):889-99.

155. Shimaoka M, Salas A, Yang W, Weitz-Schmidt G, Springer TA. Small molecule integrin antagonists that bind to the beta2 subunit I-like domain and activate signals in one direction and block them in the other. Immunity. 2003;19(3):391-402.

156. Yang W, Carman CV, Kim M, Salas A, Shimaoka M, Springer TA. A small molecule agonist of an integrin, alphaLbeta2. J Biol Chem. 2006;281(49):37904-12.

157. Keating SM, Clark KR, Stefanich LD, Arellano F, Edwards CP, Bodary SC, et al. Competition between intercellular adhesion molecule-1 and a small-molecule antagonist for a common binding site on the alphal subunit of lymphocyte function-associated antigen-1. Protein Sci. 2006;15(2):290-303.

158. Maiguel D, Faridi MH, Wei C, Kuwano Y, Balla KM, Hernandez D, et al. Small molecule-mediated activation of the integrin CD11b/CD18 reduces inflammatory disease. Sci Signal. 2011;4(189):57.

159. Fattori J, Rodrigues FHS, Pontes JGM, Paula Espíndola A, Tasic L. Chapter 6 - Monitoring intermolecular and intramolecular interactions by NMR spectroscopy. Applications of NMR Spectroscopy: Volume 3: Bentham Science Publishers; 2015. p. 180-266.

160. Mandal PK, Majumdar A. A comprehensive discussion of HSQC and HMQC pulse sequences. Concepts in Magnetic Resonance. 2004;20:1-23.

161. Bhunia A, Bhattacharjya S, Chatterjee S. Applications of saturation transfer difference NMR in biological systems. Drug Discov Today. 2012;17(9-10):505-13.

162. Fernández C, Jahnke W. New approaches for NMR screening in drug discovery. Drug Discov Today Technol. 2004;1(3):277-83.

163. Mayer M, Meyer B. Group epitope mapping by saturation transfer difference NMR to identify segments of a ligand in direct contact with a protein receptor. J Am Chem Soc. 2001;123(25):6108-17.

164. Brender JR, Krishnamoorthy J, Ghosh A, Bhunia A. Binding moiety mapping by saturation transfer difference NMR. Methods Mol Biol. 2018;1824:49-65.

165. Airoldi C, Merlo S, Sironi E. Chapter 4 - NMR molecular recognition studies for the elucidation of protein and nucleic acid structure and function. Applications of NMR Spectroscopy: Bentham Science Publishers; 2015. p. 147-219.

166. Unione L, Galante S, Díaz D, Cañada FJ, Jiménez-Barbero J. NMR and molecular recognition. The application of ligand-based NMR methods to monitor molecular interactions. MedChemComm. 2014;5(9):1280-9.

167. Vogtherr M, Peters T. Application of NMR based binding assays to identify key hydroxy groups for intermolecular recognition. J Am Chem Soc. 2000;122(25):6093-9.

168. Aires-de-Sousa J, Hemmer MC, Gasteiger J. Prediction of 1H NMR chemical shifts using neural networks. Anal Chem. 2002;74(1):80-90.

169. Nieva-Echevarría B, Goicoechea E, Manzanos MJ, Guillén MD. A method based on 1H NMR spectral data useful to evaluate the hydrolysis level in complex lipid mixtures. Food Res Int. 2014;66:379-87.

170. Minichino A, Habash J, Raftery J, Helliwell JR. The properties of (2Fo - Fc) and (Fo - Fc) electron-density maps at medium-to-high resolutions. Acta Crystallogr D Biol Crystallogr. 2003;59(Pt 5):843-9.

171. Lamb AL, Kappock TJ, Silvaggi NR. You are lost without a map: Navigating the sea of protein structures. Biochim Biophys Acta. 2015;1854(4):258-68.

172. Ehrmann FR, Stojko J, Metz A, Debaene F, Barandun LJ, Heine A, et al. Soaking suggests "alternative facts": Only co-crystallization discloses major ligand-induced interface rearrangements of a homodimeric tRNA-binding protein indicating a novel mode-of-inhibition. PLoS One. 2017;12(4):e0175723.

173. Danley DE. Crystallization to obtain protein-ligand complexes for structure-aided drug design. Acta Crystallogr D Biol Crystallogr. 2006;62(Pt 6):569-75.

174. Lelouard H, Fallet M, de Bovis B, Méresse S, Gorvel JP. Peyer's patch dendritic cells sample antigens by extending dendrites through M cell-specific transcellular pores. Gastroenterology. 2012;142(3):592-601.

175. San Sebastian E, Mercero JM, Stote RH, Dejaegere A, Cossío FP, Lopez X. On the affinity regulation of the metal-ion-dependent adhesion sites in integrins. J Am Chem Soc. 2006;128(11):3554-63.

176. Zhang X, Bajic G, Andersen GR, Christiansen SH, Vorup-Jensen T. The cationic peptide LL-37 binds Mac-1 (CD11b/CD18) with a low dissociation rate and promotes phagocytosis. Biochim Biophys Acta. 2016;1864(5):471-8.

177. Chataway J, Schuerer N, Alsanousi A, Chan D, MacManus D, Hunter K, et al. Effect of high-dose simvastatin on brain atrophy and disability in secondary progressive multiple sclerosis (MS-STAT): a randomised, placebo-controlled, phase 2 trial. Lancet. 2014;383(9936):2213-21.

178. Björkhem-Bergman L, Lindh JD, Bergman P. What is a relevant statin concentration in cell experiments claiming pleiotropic effects? Br J Clin Pharmacol. 2011;72(1):164-5.

179. Bergman E, Forsell P, Tevell A, Persson EM, Hedeland M, Bondesson U, et al. Biliary secretion of rosuvastatin and bile acids in humans during the absorption phase. Eur J Pharm Sci. 2006;29(3-4):205-14.

180. Ye F, Hu G, Taylor D, Ratnikov B, Bobkov AA, McLean MA, et al. Recreation of the terminal events in physiological integrin activation. J Cell Biol. 2010;188(1):157-73.

181. Campbell MG, Cormier A, Ito S, Seed RI, Bondesson AJ, Lou J, et al. Cryo-EM reveals integrin-mediated TGF-β activation without release from latent TGF-β. Cell. 2020;180(3):490-501.

182. Dransfield I, Cabañas C, Craig A, Hogg N. Divalent cation regulation of the function of the leukocyte integrin LFA-1. J Cell Biol. 1992;116(1):219-26.

183. Labadia ME, Jeanfavre DD, Caviness GO, Morelock MM. Molecular regulation of the interaction between leukocyte function-associated antigen-1 and soluble ICAM-1 by divalent metal cations. J Immunol. 1998;161(2):836-42.

184. Brown KL, Banerjee S, Feigley A, Abe H, Blackwell TS, Pozzi A, et al. Salt-bridge modulates differential calcium-mediated ligand binding to integrin α1- and α2-I domains. Sci Rep. 2018;8(1):2916.

185. Emsley J, Knight CG, Farndale RW, Barnes MJ, Liddington RC. Structural basis of collagen recognition by integrin alpha2beta1. Cell. 2000;101(1):47-56.

186. Nunes AM, Zhu J, Jezioro J, Minetti CA, Remeta DP, Farndale RW, et al. Intrinsic local destabilization of the C-terminus predisposes integrin α1 I domain to a conformational switch induced by collagen binding. Protein Sci. 2016;25(9):1672-81.

187. Wang Z, Thinn AMM, Zhu J. A pivotal role for a conserved bulky residue at the α1-helix of the αI integrin domain in ligand binding. J Biol Chem. 2017;292(50):20756-68.

188. Wang J, Su Y, Iacob RE, Engen JR, Springer TA. General structural features that regulate integrin affinity revealed by atypical αVβ8. Nat Commun. 2019;10(1):5481.

APPENDICES

Appendix 1: Composition of media used for *Escherichia coli* culture to express the αX I-domain

Luria-Bertani (LB) Media

For one liter of LB broth, 10 g tryptone, 5 g yeast extract, and 10 g NaCl were dissolved in 800 mL of water. The mixture was ensured to maintain a pH of 7.4, and water was added up to one liter. The broth was autoclaved. For plates, 15 g of agar was added to the broth to achieve a final concentration of 1.5%.

5X M9 Solution

5X M9 solution was prepared by adding 64 g $Na_2HPO_4.7H_2O$, 15 g KH_2PO_4, AND 2.5 g NaCl to 1 L MilliQ water and autoclaved.

Solution Q

One liter of Solution Q contained 8mL of 5M HCl, 5 g $FeCl_2$, 185 mg $CaCl_2$, 64 mg H_3BO_3, 18 mg $CoCl_2$, 4 mg $CuCl_2$, 605 mg Na_2MoO_4, and 40 mg $MnCl_2.4H_2O$.

M9 Minimal Media

372 mL of water was autoclaved, to which 100 mL volume of autoclaved 5X M9 solution was added. This solution was supplemented with 1 mL of 1M $MgSO_4$, 50 µL of 1M $CaCl_2$, 5 mL of 100X Vitamin Solution (Sigma), 2 mL of Solution Q, 10 mL of 20% d-glucose, 5 mL of 0.1 g/mL NH_4Cl, 5 mL of 0.1 g/mL $(NH_4)_2SO_4$ after each of these solutions was filter sterilized.

Appendix 2: Composition of SDS-PAGE gels to prepare one gel

Resolving gel containing 12% acrylamide	
40% Acrylamide/Bis-acrylamide (Bio-Rad)	1.2 mL
1.5 M Tris-HCl, pH 8.8	1.3 mL
10% SDS	200 µL
30% Ammonium Persulfate	10 µL
TEMED	4 µL
deionized H_2O	1.4 mL

Stacking gel containing 4% acrylamide	
40% Acrylamide/Bis-acrylamide (Bio-Rad)	250 µL
1.0 M Tris-HCl, pH 6.8	250 µL
10% SDS	100 µL
30% Ammonium Persulfate	8 µL
TEMED	4 µL
deionized H_2O	1.95 mL

Appendix 3: Chemical shift ambiguity index value definitions

The values other than 1 are used for those atoms with different chemical shifts that cannot be assigned to stereospecific atoms or to specific residues or chains.

Index Value	Definitions
1	Unique (including isolated methyl protons, geminal atoms, and germinal methyl groups with identical chemical shifts)
2	Ambiguity of geminal atoms or geminal methyl proton
3	Aromatic atoms on opposite sides of symmetrical rings (e.g. TYR HE1 and HE2 protons)
4	Intra-residue ambiguities
5	Inter-residue ambiguities
6	Intermolecular ambiguities
9	Ambiguous, specific ambiguity not defined